ТЕОРІЯ ХІМІЧНОЇ БУДОВИ ТА РЕАКЦІЙНОЇ ЗДАТНОСТІ ПОВЕРХНІ. МОДЕЛЮВАННЯ ПРОЦЕСІВ НА ПОВЕРХНІ

UDC 544.18:546.72 *DOI: 10.15407/Surface.2025.17.003*

IRON-CONTAINING DERIVATIVES OF GRAPHENE

O. S. Kremen, V. V. Lobanov, M. T. Kartel

Chuiko Institute of Surface Chemistry of the NAS of Ukraine,
17 Oleh Mudrak Str., Kyiv-03164, Ukraine, e-mail: kremenoksana@ukr.net

The review focuses on the results of quantum-chemical calculations of the properties of electrocatalysts based on iron-containing carbons, mainly graphene. Depending on the nitrogen atom states in electrocatalysts produced by pyrolysis of a mixture of carbon-, nitrogen-, and iron-containing precursors, a method for assigning N1s peaks in XPS was described. The different types of nitrogen atoms in ORR electrocatalysts enable a semi-quantitative determination by combining data from experimentally obtained XPS spectra with quantum-chemical calculations of chemically induced shifts in N1s core-level energies.

Quantitative analysis of the EXAFS and XANES spectra regions of FeN-C catalysts, which are free or nearly free of Fe crystalline structures, revealed the presence of porphyrin-like FeN_4C_{12} fragments. Electrochemical studies showed that these FeN_4C_{12} fragments catalyze the four-electron reduction of O_2 to water. Such porphyrin-like fragments can form either within highly disordered graphene sheets or between the zigzag edges of graphene, leading to the formation of micropores. FeN-C catalysts subjected to Ar- and NH_3-pyrolysis exhibit significantly different ORR activities. The increased ORR activity associated with FeN_4C_{12}-type fragments results from highly basic N-groups generated during pyrolysis with NH_3.

A detailed kinetic and thermodynamic analysis of ORR on FeN_4-G type catalyst with all pyrrole nitrogen atoms showed that the activation energy of dissociation of the adsorbed O_2 molecule is very high, regardless of its adsorption type on FeN_4-G catalyst in the Pauling or Griffiths model configuration.

The calculated ORR free energy change diagrams indicate that for all its elementary stages via the four-electron mechanism, the free energy changes (ΔG) are negative at low electrode potentials (up to 0.41 V). The rate-limiting stage for the entire ORR is the reduction of $OH_{(ads)}$ to $H_2O_{(ads)}$, with E_{act} = 1.02 eV.

The first self-consistent comparison of the activity of several potential structures of edge defects in the active center of iron-containing catalysts based on graphene nanocarbon showed that, depending on the synthesis conditions, the most stable Fe-containing defects are structures with four or three nitrogen atoms. It is assumed that both of these structures can coexist. Cluster structures of the FeN_3 (Fe_2N_5) type are capable of cleaving the bond in the O_2 molecule with a zero activation barrier and, therefore, can direct ORR along the dissociative route. This route is expected to be more selective, without H_2O_2 formation, due to the excess binding of ORR intermediates. Ab initio molecular dynamics data indicate that this spontaneous reaction is likely to be unaffected by solvation, as the solvent does not seem to alter the stability of the considered edge defects.

The DFT results showed that as the nitrogen doping level of graphene-FeN_x (x = 4, 3, 2, 1) increases, their activity in the hydrochlorination reaction increases sequentially. The following order of E_{act} for the catalytic reaction of the graphene-FeN_x catalyst series is obtained: graphene-FeN_1 > graphene-FeN_2 > graphene-FeN_3 > graphene-FeN_4.

The Fe atom embedded in the graphene network activates the methane molecule with an activation energy of 25.7 kcal/mol without applying an external electric field. The stability of the adsorption complexes, transition states, and products changes significantly under the influence of the direction and strength of the applied electric field. A positive electric field destabilizes the adsorption complexes, while the transition state and products are more stable compared to the case without a field. The activation energy decreased significantly from 25.7 to 17.5 kcal/mol when an electric field of +0.015 a.u. was applied. The results indicate that an applied external electric field can control the catalytic activity of graphene when iron is added. Using aberration-corrected TEM, we show that the diffusion of single Fe atoms at graphene edges depends on the edge type (zigzag and armchair), with subdiffusion occurring at armchair edges and superdiffusion occurring at zigzag edges. Theoretical calculations show that this difference is due to different diffusion barriers between stable states. The anomalous diffusion behaviour can be expected to affect the growth/catalysis kinetics of synthetic sp^2 nanomaterials grown using metal catalysts. The in situ observations and theoretical studies (MD and DFT) provide key insights into the fundamental growth processes of sp^2 nanostructures, such as graphene and carbon nanotubes, on metal catalysts.

Keywords: *density functional theory (DFT), iron-based electrocatalysts, X-ray photoelectron spectra (XPS), N1s core levels, porphyrin-like fragments, oxygen reduction reaction (ORR), four-electron ORR mechanism, degree of nitrogen doping in graphene, anomalous diffusion.*

CONTENT

ABBREVIATIONS AND NOTATIONS

AC-TEM	Aberration-corrected transmission electron microscope
B3LYP	Hybrid functional in density functional theory
B_{bond}	The binding energy of Fe on FeN_4-G
B_E	Binding energy
CLS	Chemistry-induced variations in core-level shifts
CNT	Carbon nanotube
CUS	Coordinatively unsaturated iron sites
DFT	Density functional theory

DFTB	Density functional tight binding
DFTB-MD	Density functional tight binding molecular dynamics
DFT-D	Density functional theory computation including a dispersion term
DOS	Density of state
E_{act}	Activation energy
E_{ads}	Adsorption energy
$E_{ads\ state}$	Total energy of C_2H_2/HCl and the catalyst
E_{C2H2}	Energy of the isolated molecule C_2H_2
$E_{catalyst}$	Energy of the isolated catalyst
$E_{co-ads\ state}$	Total energy of molecules C_2H_2, HCl, and the catalyst
E_{dis}	Dissociation energy
E_F	Fermi energy
EF	Applied an external electric field
E_G	Total energy for optimized pristine graphene sheet
E_{HCl}	Energy of the isolated molecule HCl
EM	Electron microscopy
E_{react}	Reaction energy
E_{tot}	Total energy of the adsorption complex
E_X	Total energy of the isolated X species
EXAFS	Extended X-ray absorption fine structure
FePc	Phthalocyanine
FMO	Frontier molecular orbitals
FWHM	Full width at half maximum
G	Graphene
GGA	Generalized gradient approximation
G-N_x	Graphene material in which N atoms are not bonded to TM atoms
Graphene-FeN_2-Hex	Two adjacent N atoms are located in a six-membered ring
Graphene-FeN_2-Oppo	Two N atoms are located on opposite sides of the Fe
Graphene-FeN_2-Pen	Two adjacent N atoms are located in a five-membered ring
G-TMN_x	Graphene material containing TM atoms with N atoms coordinated to them
G-TMN_x/G-N_x	Graphene material in which the atoms share G-N_x and G-TMN_x groupings
HAADF-STEM	High-angle annular dark field scanning transmission electron microscopy
HOMO	Highest occupied molecular orbital
HR TEM	High-resolution transmission EM
HR-TEM	High-resolution transmission electron microscope
IM	Intermediate
IRC	Intrinsic reaction coordinate
LANL2DZ	Effective core pseudo-potentials basis set
LST	Linear synchronous transit
LT-STM, 4 K	Low-temperature scanning tunnelling microscopy
LUMO	Lowest unoccupied molecular orbital
LVACTEM	Low-voltage aberration-corrected transmission electron microscopy
MD	Molecular dynamics
MSD	Mean square displacement
MXAN	Method of complete quantitative analysis of Fe K-edge X-ray absorption spectra
NBO	Natural bond orbital

Near-edge	Near-edge X-ray absorption fine structure
ORR	Oxygen reduction reaction
P1	Pauling model 1
P2	Pauling model 2
PBE	Generalized gradient approximation in the Perdew-Burke-Ernzerhof functional
Pc	Phthalocyanine
PDOS	Partial DOS
PElM	Polymer electrolyte membrane
PGM	Platinum group metals
QST	Quadratic synchronous transit
RRDE	Rotating ring disk electrode
SDD	Stuttgart-Dresden effective core potential
SHE	Normal hydrogen electrode
STM	Scanning tunneling microscopy
TDOS	Total DOS
TEM	Transmission electron microscopy
TS	Transition state
TM	Transition metal
XAFS	X-ray absorption fine structure
XANES	X-ray absorption near-edge structure
XPS	X-ray photoelectron spectroscopy
XRD	X-ray diffraction
ZPE	Zero-point energy
η^2	Type interaction at the Fe site of the G
$B_E(1s)$	The binding energy of the 1*s*-electron
$B_E(N1s)$	The binding energy of the *1s*-electron of the N atom
TM	Transition metal

INTRODUCTION

The negative impacts of carbon dioxide emissions on the planet's climate have underscored the need for a gradual transition from fossil fuels to environmentally friendly renewable energy sources. The most promising technological solution is the fuel cell. This electrochemical cell converts the chemical energy of environmentally friendly fuels, such as hydrogen and an oxidizer (primarily oxygen), into electricity, producing molecular oxygen via oxidation-reduction reactions and the formation of water. This technology, although very promising, currently faces many problems, not only due to the low specific energy released but also because of the high activation barriers of the corresponding reactions, the slow kinetics of electroreduction, and the low selectivity for a specific target product. The latter is due to the many possible parallel reactions that often occur on the electrodes. Until recently, these processes have used electrocatalysts exclusively based on platinum group metals (PGMs), as they enhance the efficiency and selectivity of electrochemical transformations, thereby increasing the reaction rate. However, the electrocatalysts that exist today are still largely insufficiently effective for achieving the economic benefits of the processes and are quite expensive. Therefore, one of the primary tasks in the field of creating electrocatalysts is to find and develop innovative, relatively inexpensive catalytic materials with improved characteristics. The primary interest is in replacing expensive electrode catalysts using PGM with new and more affordable materials that either do not contain PGM or include non-noble transition metals, mainly iron.

The review considers the results of quantum chemical studies of the properties of electrocatalysts based on iron-containing carbons, mainly graphene. Results from modern quantum chemistry and molecular dynamics methods enable the prediction of strategies for creating new catalysts with improved efficiency and selectivity.

ASSIGNMENT OF XPS PEAKS OF NITROGEN-CONTAINING FUNCTIONAL GROUPS IN NITROGEN-DOPED GRAPHENE (GN_x) AND NITROGEN-FUNCTIONALIZED IRON ($GFeN_x$) HETEROGENEOUS ELECTROCATALYSTS

Graphene (G), due to its unusual properties, as confirmed by various theoretical and experimental studies of electrical [1, 2], magnetic [3, 4], and mechanical [5] properties, is considered one of the most promising materials of the early twenty-first century [6–8]. In particular, the unique band structure of G gives rise to numerous anomalous electronic and transport properties, including the anomalous quantum Hall effect [9, 10]. However, the G of an ideal structure without defects and dopants has limited practical application due to the absence of a band gap in the electronic band structure, low charge carrier density, non-magnetism, and chemical inertness [11–13]. The properties of G can be modified by doping with heteroatoms or by functionalization, thereby expanding its use as a material for high-capacity capacitors [14], nanoelectronic applications [15–17], selective catalysts [18], and spin electronics [19].

G is doped simultaneously or sequentially with nitrogen and/or transition metals, and a set of materials is formed in which nitrogen and transition metal atoms are incorporated into different fragments of the graphene network [20].

The most widely used materials in chemistry are those based on G containing transition metal (TM) atoms as cathode electrocatalysts for the oxygen reduction reaction (ORR) [20]. This is primarily because fuel cells are promising next-generation energy sources, given their high efficiency and low operating temperatures, which make them indispensable for use in transport and residential areas [21]. The second most important factor in the spread of such materials is the high cost of platinum, which serves as the most effective catalyst in fuel cells with a polymer electrolyte membrane (PElM). In addition to their high cost, platinum-containing catalysts lose stability and activity over time [22].

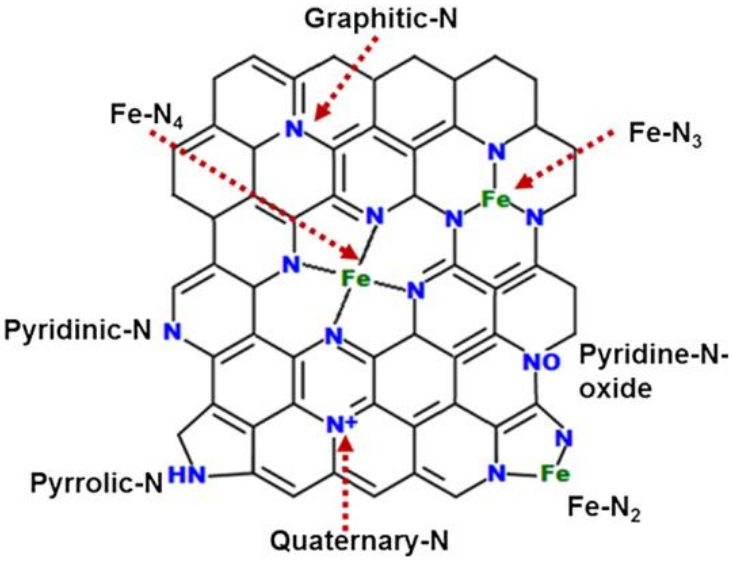

Fig. 1. Schematic of nitrogen species present in nitrogen-doped graphene ($G\text{-}N_x$) and nitrogen functionalized iron ($G\text{-}FeN_x$) heterogeneous electrocatalysts [41]

Therefore, numerous attempts to develop cheaper, platinum-free electrocatalysts are understandable, and graphene catalysts containing TM atoms, particularly iron atoms, in combination with nitrogen atoms coordinated to them ($G\text{-}TMN_x$) occupy a leading position. Also worthy of attention as electrocatalysts are graphene-like materials in which nitrogen atoms are

not bound to transition metal atoms (G-N_x), as well as those in which nitrogen atoms of both types, G-TMN_x/G-N_x, are present. Carbon-containing materials, in addition to graphene sheets, can be nanofibers and carbon nanotubes [22–26]. Among the transition metal atoms, Fe and Co atoms are most often used [27–29]. Variations in carbon carriers, types of nitrogen atom binding, and the nature of TM make it possible to purposefully change the electronic, chemical, and morphological properties of local active centres to enhance their electrochemical activity [30–33].

Among the platinum-free nitrogen-functionalized catalytic systems, the transition-metal catalyst G-TMN_x exhibited high catalytic activity, suggesting that nitrogen coordination to the metal atom forms new ORR-active sites. However, previous studies have not provided any insight into which type or types of G-TMN_x and G-TMN_x/G-N_x sites exhibit the highest ORR activity [24, 34, 35], and the debate regarding the role played by nitrogen-containing sites alone in the electrocatalytic activity of graphene catalysts continues. Since the ORR routes and the reaction pathways for hydrogen peroxide (H_2O_2) formation depend on the specific nature of the existing active sites, it is expected that the role of nitrogen-containing sites will be decisive.

Nitrogen, which is present in the three types of functionalized materials (G-TMN_x, G-TMN_x/G-N_x and G-N_x), can be part of several different functional groups, the presence of which, in principle, can be demonstrated by X-ray photoelectron spectroscopy (XPS) [36] and high-level quantum chemical calculations.

The XPS method has become a primary surface-analysis technique for determining the properties of heterogeneous electrocatalysts, in which chemically induced variations in core-level shifts (CLS) are used to detect and identify surface groups [27, 28, 37]. According to the results obtained from numerous high-resolution XPS data, nitrogen-containing moieties can be in the following forms in pyrolysis electrocatalysts: (1) pyridinic-N, (2) pyrrolic-N, (3) pyridine-N-oxide, (4) quaternary-N, and (5) graphitic-N, as well as in various other forms when it is coordinated to the transition metal atom (Fig. 1) [38–42].

However, the role of these types of functional groups in ORR remains unclear and largely depends on the preparation method of the G-based electrocatalysts. Nitrogen-functionalized carbon materials are complex, heterogeneous materials, and the relationships between overall catalytic activity and the activity of different nitrogen-containing moieties remain unclear. For example, several studies [42, 43] have shown that pyridinic-N and pyrrolic-N moieties are the most catalytically active in ORR. At the same time, other data indicate that catalysts with a higher amount of graphitic-N [4, 4] or quaternary-N [4, 5] functional groups exhibit higher ORR activity. The inconsistencies in the literature reports can be attributed to inadequate calibration of the XPS spectra and to secondary effects arising from different coordination environments of the TM atoms. These effects are most pronounced for graphitic nitrogen atoms, whose binding energies range from 401.5 to 403.0 eV, depending on the chemical environment. The significant overlap of the binding energies (B_E) for the quaternary-N (nitrogen with a charge of +1) and graphitic-N groups makes their identification in the N1*s* XPS spectrum difficult. Moreover, the lack of suitable reference data can also lead to a wide range of N1*s* binding energies for different types of nitrogen-containing moieties. Due to these uncertainties, relating XPS spectral features to a specific structure of the nitrogen-containing group is a difficult task, and inferring detailed structure-property relationships from experimentally obtained XPS spectra alone is highly ambiguous. Because of this circumstance, in works [27, 41] the density functional theory (DFT) [46, 47] with the PBE functional [48] was used to calculate the binding energies of the 1*s* electron of nitrogen atoms in nitrogen-containing fragments, which are necessary for the accurate identification and interpretation of the position of this 1*s* level in the XPS spectra of nitrogen-containing G-based catalysts (XPS N1*s* spectra). The complementary experimental and computational results allowed us to determine the presence of different types of nitrogen-containing functional groups, emphasizing the centers containing the TM atom to which the nitrogen atoms are coordinated and graphitic-N. The role of these groups in the oxygen reduction

occurring in the G-N_x systems obtained by doping graphene plates with nitrogen only is also explained. This putative unification of experiment and theory allows us to relate the nature of each type of active site to the ORR rate using XPS data directly.

In progress [41], six clusters were considered, each of which modelled a particular section of the doped graphene plane. A section of the graphene plane of the ideal structure was represented by a region measuring 9.843 by 8.524 Å. It contained 32 carbon atoms (C_{32}) (Fig. 2*a*). A similar section with four pyridinic-N atoms was obtained from the C_{32} cluster, from which two central carbon atoms were removed. The four carbon atoms closest to the formed double vacancy were replaced by N atoms ($C_{26}N_4$) (Fig. 2*b*). A cluster reproducing a state with a graphitic-N atom was obtained from the C_{32} cluster, in which one of the C atoms was replaced by a nitrogen atom ($C_{31}N$). (Fig. 2*c*). Three clusters of the G-FeN_x series with nitrogen atoms coordinated to an iron atom were obtained similarly: G-FeN_2 from the $C_{26}N_4$ cluster by introducing an Fe atom into the center of a double vacancy and replacing two of the four N atoms surrounding the vacancy with carbon atoms (Fig. 2*d*); G-FeN_3 from the $C_{31}N$ cluster by replacing one of the carbon atoms with an Fe atom (Fig. 2*e*); the G-FeN_4 cluster from the $C_{26}N_4$ cluster by introducing an iron atom into the center of a double vacancy (Fig. 2*f*).

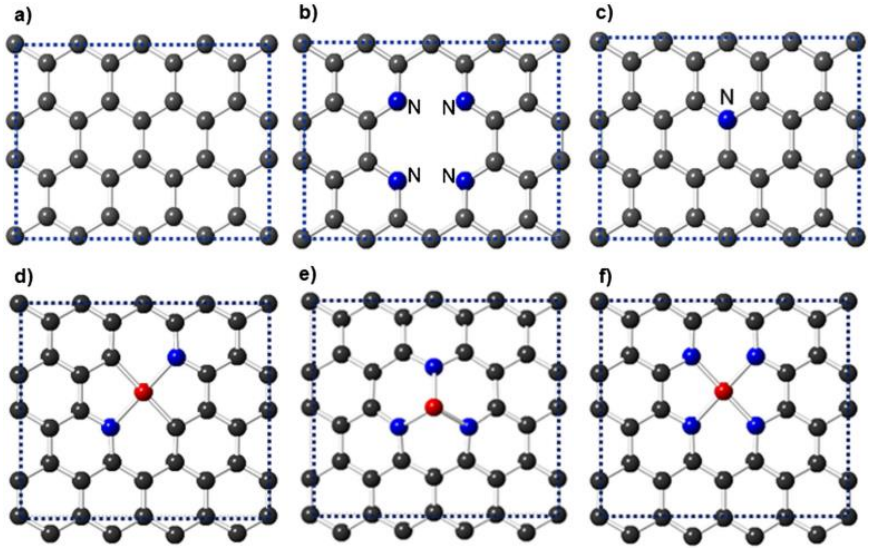

Fig. 2. Top view of the doped graphene configurations considered in [41]: Metal-free defects: (*a*) Pristine graphene sheet (C_{32}), (*b*) Pyridinic-N ($C_{26}N_4$), (*c*) Graphitic-N ($C_{31}N$), and nitrogen coordinated to metal defects (*d*) G-FeN_2, (*e*) G-FeN_3, (*f*) G-FeN_4. Gray: Carbon; Blue: Nitrogen; Red: Fe [41]

Following the recommendations of works [49, 50], the values of BE for the structures G-FeN_x and G-N_x were calculated as the difference between the orbital energy (B_E (1*s*)) obtained by the DFT method and the Fermi level (E_F) of the corresponding cluster. The chemical shift of the BE (N1*s*) level was defined as the difference in the B_Es between the corresponding cluster and the cluster that reproduces the pyridine structure. According to this definition, a positive CLS value corresponds to a higher BE than that of the pyridinic structure, and vice versa. The assignment of the N1*s* peak in the experimentally obtained spectrum of the sample was made by adding the CLS value calculated by the DFT method to the energy of the N1*s* peak in the XPS spectrum of the reference structure of the pyridinic-N.

Initially, reference XPS spectra of such standard compounds as polypyrrole (pyrrolic-N) and polypyridine (pyridinic-N) were obtained in [41]. The assignment of high-resolution N1*s* spectra was made using a single peak for which the full width at half maximum (FWHM) was 1.1 eV at an energy of 398.8 eV for polypyridine (pyridinic-N) and 400.7 eV for polypyrrole (pyrrolic-N) (see Fig. 3*a* and 3*b*). The peak positions are consistent with the reference databases

[51, 52]. The FWHM values for the pyridinic-N peak and the pyrrolic-N are 1.1 and 1.3 eV, respectively. The assignment of the N1*s* peaks was obtained according to those published earlier [53]: imine (398.0), pyridinic-N (398.8), nitrogen coordinated to FeN_x (399.8), pyrrolic-N (400.7), quaternary-N (401.8), and graphitic-N (403.3 eV). In addition to the peaks due to different types of nitrogen to carbon coordination, there is a peak at 3998 eV assigned to the G-FeN_x family of groups, which includes different geometries and chemical environments, namely G-FeN_4, G-FeN_3, and G-FeN_2. Through the correlation of XPS and Mössbauer spectra, the peak due to the mesomeric FeN_4 center, in which all nitrogen atoms are equally bound to the metal atom, was assigned to the FeN_x peak in the XPS spectrum of N1*s* [54].

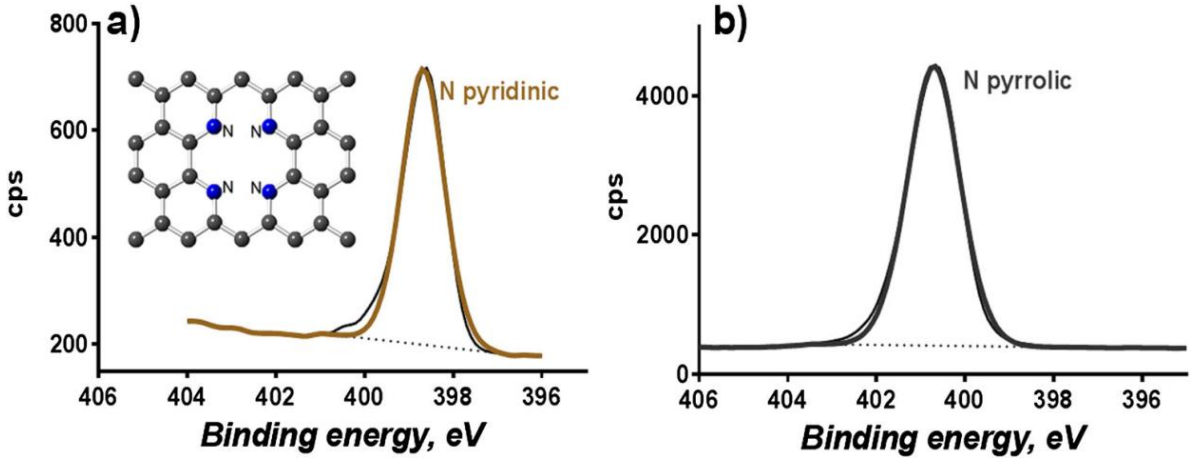

Fig. 3. X-ray photoelectron spectroscopy N1*s* spectra for (*a*) pyridinic-N reference peak and (*b*) pyrrolic-N nitrogen moieties obtained experimentally [41]

The chemical environment of nitrogen-doped G defects in a heterogeneous electrocatalyst can be determined by comparing their B_E obtained from XPS data. However, calculating B_E and chemical shift from DFT data is somewhat complicated. Due to the substantial change in the Coulomb potential near the nuclei, the absolute value of the B_E of the defects in question is irrelevant, since minor distortions of the electron wave functions can lead to significant deviations in the orbital energies. By comparing the B_E shifts relative to the overall experimental and calculated reference structure, this error can be significantly reduced or eliminated.

The reference structure, available both experimentally and theoretically as pyridinic-N($C_{26}N_4$), was used for the calculations. The chemical shift of N1*s* was calculated as CLS = B_E (defect) – B_E ($C_{26}N_4$). The shifts of the B_E of the nitrogen atom for two different types of coordination with Fe and Co, i.e., G-FeN_x and G-N_x, were reported in [49, 50]. The defects of the FeN_2 type had lower CLS values, ranging from 0.9 to 1.1 eV, than those calculated by the DFT method. The overlaps of the peaks due to defects of the FeN_3 and FeN_4 types significantly exceed their shifts concerning the $C_{26}N_4$/N-pyridine reference structure in the XPS spectrum. Therefore, the defects of FeN_3 and FeN_4 fragments were predicted to have a higher CLS = 1.5 eV and significantly higher formation energies. The CLS values obtained by DFT were used to calibrate the XPS N1*s* spectra.

Among the active sites involving the nitrogen atom that are of interest, graphitic-N deserves special attention. It was agreed that groups with nitrogen coordinated to TMs, such as Fe (FeN_x), are active sites that catalyze the complete reduction of oxygen to water via a four-electron mechanism. Still, spectroscopic methods did not allow the authors [41] to identify a specific geometric coordination of nitrogen. The role of graphitic-N in nitrogen-doped mesoporous carbons and nitrogen-doped graphenes for ORR has also been widely discussed in the literature. Some papers claim a partial reduction of oxygen to hydrogen peroxide (two-electron mechanism) [37, 56, 57], while other papers provide evidence for the complete

conversion of oxygen to water [57, 58]. This is important for the design of electrocatalysts with a preferred content of a particular type of defect.

The experimentally obtained N1*s* peak for graphitic-N was previously assigned to an energy of 401.8 eV [50]. However, graphitic-N has a B_E of 401.5 to 405 eV, depending on the chemical nature of other nitrogen atoms in the immediate vicinity. Therefore, the B_E of the peak previously assigned to 401.8 eV corresponds to a mixture of graphitic and quaternary nitrogen, which significantly complicates the precise identification of the graphitic-N defect type and its concentration.

However, using DFT calculations, a CLS was predicted for graphitic-N relative to the pyridinic-N reference in [41]. The N1*s* peak position for graphitic-N is 402.1 eV, which was then recalculated by adding the DFT calculated CLS to the experimentally observed N1*s* peak position in the pyridinic-N reference (B_E = 398.8 eV (pyridinic-N, reference, experiment) + 3.3 eV (CLS, DFT) = 402.1 eV). This B_E was previously attributed to the quaternary nitrogen atom in an XPS experiment. DFT calculations [41] indicate that the peak at 402.1 eV likely contains a significant contribution from the graphitic-N moiety. Moreover, the DFT-predicted CLS = 3.3 eV is consistent with experimental observations and corresponds to the G-N_x B_E shift obtained in [49, 50] for ORR electrocatalysts.

After developing a technique to determine the nature of N-containing catalytic sites in carbon materials using XPS data, the activity of the resulting catalysts was evaluated for ORR [41]. It is known that the conditions of catalyst heat treatment (temperature, duration, and temperature sweep rate) significantly affect its electrocatalytic activity [60]. Moreover, a variety of functional N-containing fragments can be formed under different heat-treatment temperatures. Therefore, to better understand the role of each specific N-containing group in oxygen reduction, the Rotating Ring Disk Electrode (RRDE) method was employed to obtain both qualitative and quantitative information about the catalysts and the electrochemical reactions occurring in the electrolyte. The RRDE method takes advantage of the laminar flow created by rotation. As the reaction mixture rotates, the solution in contact with the electrode is diverted to the side, which is similar to the situation with a rotating disk electrode. As the solution is diverted to the side, it crosses the ring electrode and flows back into the primary reaction medium. In the RRDE method, the ORR occurs on the electrode disk via a four-electron mechanism. It was found that the G-N_x catalyst sample obtained by pyrolysis at 300°C contained the highest relative amount of graphitic-N (72.8%), which showed the lowest limiting current density (0.7 mA cm^2) and the highest hydrogen peroxide yield (86%), indicating that this catalyst primarily promotes the first step of the two-electron ORR mechanism, which leads to the formation of the intermediate product, hydrogen peroxide ($O_2 + 2e^- + 2H^+ \rightarrow H_2O_2$). In contrast, when the G-N_x sample was heat treated at a higher temperature (800°C), a significant decrease in the relative amount of graphitic-N (19.8%) and an increase in the content of amine-N (33.3%) as well as pyridinic-N (28.2%) were obtained, resulting in a higher limiting current density (1.4 mA·cm^2) and a decrease in the yield of hydrogen peroxide. This observation suggests that amine-N and pyridinic-N contribute to the second step of the two-electron ORR mechanism, i.e., the reduction of hydrogen peroxide to H_2O ($H_2O_2 + 2H^+ + 2e^- \rightarrow 4H_2O$).

ORR catalysis, G-FeN_x catalyst pyrolyzed at 800°C, was compared with the GN_x – GNS-300 sample. It was found that for the G-FeN_x sample, the yield of H_2O_2 was only 2%, which can be attributed to the presence of 11.5% graphitic-N. However, the low yield of hydrogen peroxide indicates that other defect-containing moieties present in G-FeN_x catalyst almost completely reduced oxygen to water via the four-electron ORR mechanism ($O_2 + 4e^- + 4H^+ \rightarrow H_2O$). Using XPS data, it was found that the activity of this catalyst is due to nitrogen being coordinated to the metal atom. This sample showed the highest current density (4.8 mA·cm^2) and the lowest yield of hydrogen peroxide. This indicates that the G-N_x centers can catalyze two reactions: (i) the four-electron reduction of oxygen to water and (ii) the two-electron reduction to H_2O_2, catalyzed

by graphitic-N. The pyridinic-N, which is still present in significant amounts in the obtained catalysts, also catalyzes the second step of the two-electron ORR mechanism, i.e., the reduction of hydrogen peroxide to H_2O ($H_2O_2 + 2H^{++} + 2e^- \rightarrow 4H_2O$). Although the complete reduction of O_2 to H_2O is highly desirable in fuel cells, the two-electron reduction mechanism may be applicable for the production of H_2O_2 on an industrial scale. It was found that the G-N_x sample pyrolyzed at 800°C had higher electrochemical activity and provided low peroxide yield compared to the G-FeN_x sample heat treated at 300°C. Considering that the heat treatment time and temperature rise rate remained unchanged for both G-Nx catalysts and the formation of catalytically active sites was mainly influenced by temperature, this confirms the importance of pyrolysis conditions for catalyst optimization. However, the G-N_x-800°C catalyst had significantly lower activity than the G-FeN_x catalyst heat-treated at the same temperature, indicating that iron sites play a crucial role in the ORR. Analysis of the XPS results indicates that graphitic-N and Fe lead to higher currents and minimal H_2O_2 formation, suggesting a role for these groups in either the complete reduction of O_2 to H_2O and/or the partial reduction of H_2O_2 to water.

Thus, the DFT calculations in [41] were used to calculate the CLS of graphitic-N. The results obtained convincingly demonstrate that graphitic-N is present in N-containing samples, and that the experimentally observed pyridinic-N is stable. Analysis of XPS peak intensities and positions, combined with ab initio calculations, enables the determination of the content of different types of N defects in ORR electrocatalysts. The RRDE data obtained experimentally suggest that graphitic-N moieties formed at lower temperatures significantly contribute to hydrogen peroxide formation in ORR catalysts. In contrast, metal coordination to nitrogen is critical for efficient overall ORR. The proposed combination of experiment and theory not only aids in analyzing the types of N-containing functional groups but also accelerates the design of lower-cost electrocatalysts for PElM fuel cells.

XAFS METHOD IN STUDYING THE PROPERTIES OF IRON-CONTAINING GRAPHENES

As noted above, ORR catalysis is of primary importance for metal-air batteries and fuel cells, two environmentally friendly technologies whose theoretical specific energy is sufficient to power full-size, long-range vehicles [61]. Although PElM fuel cell technology is now relatively mature, there remains a need for platinum-based catalysts. Since platinum is mainly required for the cathode due to the slow ORR rate, there is a strong incentive to search for new materials suitable for catalyzing this reaction. Following the first report [62] of increased ORR activity using $Fe(Co)N_4$ macrocycles adsorbed on a carbon-containing material as a catalyst, a line of research was developed into a new class of catalysts, subsequently named TMN-C [63], obtained by pyrolysis above 700°C. It was later shown that such catalysts can be synthesized by pyrolysis of individual metal-, nitrogen-, and carbon-containing precursors [64]. The results of [65–67] made it possible to increase their activity and durability; however, the structure of the active site or sites remained unclear for two reasons. First, the non-crystallographic ordering of metal atoms in a carbon-containing catalyst requires specialized spectroscopic methods. Secondly, the simultaneous presence of various types of active sites, along with other metal-containing phases, in most TMN-C ORR catalysts prevents the acquisition of spectroscopic evidence of their nature. Basic information on the structure of FeN-C catalyst fragments was obtained by analyzing EXAFS (extended X-ray absorption fine structure) spectra, ^{57}Fe Mössbauer spectroscopy methods, X-ray photoelectron, and mass spectroscopy [29, 68–70]. Various fragments of the gross formula FeN_xC_y [71, 72] have been proposed as active centers. It has also been hypothesized that iron simply catalyzes the formation of N-containing active centers in C-containing materials [73, 74]. However, poisoning of TMN-C catalysts with cyanide and the low efficiency of metal-free catalysts have revealed the metallic nature of the catalytic activity in

ORR [75, 76]. The works [77–79] present the results of *ab initio* calculations on the properties of TMN_xC_y fragments incorporated into graphene sheets. Binuclear structures $Fe_2N_xC_y$ were also proposed as active centers of TMN-C catalysts [79, 80]. However, spectroscopic evidence for the presence of such hypothetical centers has not yet been obtained, and their properties have not been compared with the properties of TMN-C catalysts free of crystallographic structures based on transition metals, in particular, iron.

At work [81], the structure of active centers in FeN-C catalysts pyrolyzed in argon or NH_3 was investigated. Ammonia leads to the formation of more active but less durable catalysts [65, 71]. Regardless of the gas used in pyrolysis, it was established that for FeN-C materials containing no or almost no crystallographic structures of iron, the identity of the Mössbauer spectra and XANES spectra is characteristic, which indicates the presence of the same Fe-based fragments. In [81], the structure of two putative active centers with different structures, featuring a porphyrin planar architecture with a FeN_4C_{12} grouping and an adsorbed O_2 molecule coordinated to an iron atom, was investigated and determined. The identification is confirmed by excellent agreement between the experimentally obtained X-ray absorption spectra of FeN-C catalysts, almost free of iron-based crystalline structures, and calculations using the DFT theory taking into account dispersion interactions (DFT-D) [82, 83]. Despite the identity of the FeN_4C_{12} fragments, NH_3-pyrolyzed catalysts demonstrate significantly higher activity in ORR than Ar-pyrolyzed ones. This correlates positively with the formation of N-containing groups with higher basicity during pyrolysis with ammonia, which increases the activity inherent in FeN_4C_{12} fragments due to chemical or electronic effects.

A few words about the XANES method: in the modern understanding, the name XAFS unites the designations of the names of several sections of the absorption spectrum X-rays near the absorption jump caused by the photoelectric effect: the XANES region, sometimes called NEXAFS (*near edge X-ray absorption fine structure*), limited to the energy range ±(30–50) eV relative to the excitation threshold energy (jump), and the EXAFS (*extended X-ray absorption fine structure*) region, located above the absorption jump and extending in the range from approximately 30 to 1500–2000 eV relative to the excitation threshold. The conventional division of the spectrum into these regions is due to the necessity of employing different physical approximations to describe them. XANES or XAFS spectroscopy allows one to obtain information about the nature, quantity, and location of neighbouring atoms relative to the atom under study, both in the first and in more distant coordination spheres. In this regard, XAFS spectroscopy is used for structural analysis along with X-ray diffraction analysis. At the same time, it has several additional advantages, making it possible to study substances in any aggregate state, complex chemical composition, including cases when the concentration of the atoms being studied is small (for example, impurities in alloys, catalysts, active centers in enzymes, analysis of environmental pollution), as well as to study the dynamics of transformations during chemical reactions and external influences. The development of XAFS spectroscopy is associated with the emergence of synchrotron radiation sources, without which its experimental implementation would be very problematic, since XAFS spectra are measured in the X-ray energy range of 1–100 eV.

In [81], four types of FeN-C catalysts were synthesized: $Fe_{1.0}$, $Fe_{0.5}$, $Fe_{0.5}$-900, and $Fe_{0.5}$-950. The subscript corresponds to the mass of Fe in the catalyst precursor before pyrolysis. Catalysts $Fe_{1.0}$ and $Fe_{0.5}$ were synthesized at 1050°C in Ar for one hour, and samples $Fe_{0.5}$-900 and $Fe_{0.5}$-950 were obtained by pyrolysis of sample $Fe_{0.5}$ in NH_3 for 5 min at 900 and 950°C, respectively. The Fe content and catalyst precursor preparation were modified for $Fe_{0.5}$ to avoid metal particle formation. The absence of sextet and singlet components in the Mössbauer spectrum of the mentioned samples indicates the almost complete lack of crystalline phases of zero-valent iron. The Mössbauer spectra of ^{56}Fe demonstrated their practical identity for the

$Fe_{0.5}$, $Fe_{0.5}$-900, and $Fe_{0.5}$-950 samples, indicating identical iron-containing structures in Ar- or NH_3-pyrolyzed FeN-C materials.

The Fourier transform EXAFS spectra also show the presence of iron-based crystalline structures in the $Fe_{1.0}$ sample and their absence in the $Fe_{0.5}$ sample. The assignment of the signal at 2.2–2.6 Å in the Fourier transform EXAFS spectrum to Fe-C or Fe-Fe interactions is based on the accurate analysis of the EXAFS spectrum. The Fourier transform EXAFS spectra of the NH_3-pyrolyzed $Fe_{0.5}$-900 and $Fe_{0.5}$-950 materials also show a minor signal at 2.2 Å, attributed to Fe-Fe backscattering. This minor signal increases with increasing pyrolysis time in NH_3. Its increase is explained by the higher content of crystalline Fe_2N with increasing pyrolysis time in NH_3, as determined by Mössbauer spectroscopy.

The obtained catalysts were electrochemically characterized by the RRDE method in a fuel cell with PElM. The obtained results indicate 2% yield of H_2O_2 at potentials typical for the PElM fuel cell. They are virtually independent of the disk rotation speed, suggesting a four-electron route of oxygen reduction to water. The catalyst activity measured by RRDE is the same for $Fe_{1.0}$ and $Fe_{0.5}$ samples, but significantly higher for $Fe_{0.5}$-900 and $Fe_{0.5}$-950 samples. Such an increase is typical for catalysts obtained by pyrolysis in an NH_3 atmosphere, which is known to cause the formation of fundamental N-containing groups [65, 71, 84]. The same activity of $Fe_{1.0}$ and $Fe_{0.5}$ catalysts indicates that the Fe-based particles present in $Fe_{1.0}$ are inactive in ORR, which contradicts the data on the OOR activity of carbon-encapsulated iron particles [34, 85].

The FeN_xC_y fragment present in both Ar- and NH_3-pyrolyzed FeN-C materials was studied under the assumption of the presence of four ligands in the equatorial plane (nitrogen atoms) and one or two axial ligands (O_2 molecules) in the coordination sphere of the Fe atom. First, the EXAFS spectrum of $Fe_{0.5}$ was analyzed, which does not contain Fe crystalline structures. The dominant contribution to the spectrum EXAFS gives the ligands of the first coordination sphere, Fe-N and Fe-O. The NFe-N signal was too small to determine the angle between the Fe-N bonds and, consequently, the geometry of the group. The Fe-N distance obtained for Ar- or NH_3-pyrolyzed FeN-C materials is 1.99–2.01 Å, which is consistent with the data obtained for iron porphyrins by the DFT method [86, 87].

XANES spectroscopy, which is more sensitive to the arrangement of atoms around the photoabsorber, was used to more accurately determine the structure of the catalytic center [88, 89]. First, differences were established between the XANES spectra of $Fe_{0.5}$ and non-pyrolyzed Fe(II) phthalocyanine, Fe(II)Pc. The pre-edge feature characteristic of heat-treated FeN-C catalysts is absent for the $Fe_{0.5}$ sample, indicating a violation of the D_{4h} symmetry of the ligand arrangement around the Fe atom [90]. Subsequently, the XANES spectrum of the Fe0.5 sample was quantitatively analyzed using the MXAN procedure [91], which had previously been successfully applied to heme proteins [91, 92]. Since the XANES spectra of $Fe_{0.5}$, $Fe_{0.5}$-900, and $Fe_{0.5}$-950 samples are identical, the results obtained from the XANES analysis of the $Fe_{0.5}$ sample are directly applicable to the $Fe_{0.5}$-900 and $Fe_{0.5}$-950 samples. The XANES spectrum calculation was first checked for Fe(II)Pc. Then, the XANES spectra of the model FeN_xC_y molecules, which had been previously studied using the DFT method [77–79, 93, 94], were calculated. Only the distances between the Fe and N atoms were varied in the calculation. The optimized geometry corresponds to a configuration with four nitrogen atoms at a distance of 1.95 Å (Table 1, lines 1, 3). In this case, the agreement between the experimental and calculated spectra is unsatisfactory. In the second step, the O_2 molecule was included in the calculation, and the Fe-N and Fe-O distances were optimized together with the angle between the O_2 molecule axis and the normal to the N_4 plane, as well as the distance from the Fe atom to the graphene plane. Some improvement was observed, although agreement remained unsatisfactory (Table 1, lines 2 and 4).

Below, we consider the structure with a different arrangement of carbon atoms in the N_4 plane. XANES analysis was performed for the FeN_xC_y fragment with a porphyrin structure, for which all Fe-N distances were varied. In this case, the experimental spectrum of the Fe-based

catalyst is accurately reproduced up to 90 eV above the absorption edge; however, a discrepancy remains at higher energies. With the second fitting, taking into account one oxygen molecule in the configuration perpendicular to its axis of the N_4 plane, the results are significantly improved over the entire energy range, which indicates the need to include an oxygen atom or molecule, or another light element in the axial position of the first coordination sphere of the Fe atom. When considering the second O_2 molecule in the axial position, excellent agreement was obtained between the experimental and theoretical spectra (Table 1, line 7). In this calculation, the iron coordination corresponds to a distorted octahedron embedded in a graphene sheet with two axial oxygen molecules at a distance of 1.87 Å and four equatorial nitrogen atoms at a distance of 2.00 Å from the Fe atom. Another structure capable of reproducing the experimental XANES spectrum is still represented by the porphyrin geometry with the O_2 molecule located parallel to the N_4 plane above the Fe atom, with a longer Fe-O distance of 2.00 Å and a shorter Fe-N distance of 1.93 Å (Table 1, line 8), without the iron atom moving out of the plane. The Fe-N distance is identical to that in Fe(II) phthalocyanine – 1.926 Å [93].

Table 1. Structural parameters providing the best agreement between the theoretically calculated XANES spectrum and the experimentally obtained ones for the samples $Fe_{0.5}$ (rows 1–8) and $Fe_{0.5}$-950 (rows 9, 10) of the fragments FeN_4C_{10}, FeN_4C_{12}, and $FeN_{(2+2)}C_{(4+4)}$, as well as the fragment FeN_4C_{12} [93]

No.	Coordination	Fe-N bond length, (Å)	Fe-O bond length, (Å)	Angle (°)
FeN_4C_{10}				
1	4-fold	1.95 (3)	—	—
2	5-fold	1.99 (3)	1.82 (3)	42(5)
***$FeN_{(2+2)}C_{(4+4)}$**				
3	4-fold	1.95 (3)	—	—
4	5-fold	1.97 (3)	1.80 (5)	46(6)
FeN_4C_{12}				
5	4-fold	1.98 (3)	—	—
6	5-fold	1.97 (3)	1.86 (4)	51(5)
7	6-fold	2.00 (3)	1.87 (4)	33(7)
8	6-fold	1.93 (3)	2.00 (4)	90(0)
FeN_4C_{12}				
9	6-fold	2.01 (2)	1.88 (4) [94]	55(7)
10	6-fold	1.92 (2)	2.02 (3) [94]	90(0)

*The subscripts $_{(2+2)}$ and $_{(4+4)}$ indicate that the fragment $FeN_{(2+2)}C_{(4+4)}$ has two N atoms and four C atoms entering from each of the adjacent graphene sheets.

Due to the high affinity between Fe and N [37, 96], it was necessary to investigate the stability of the FeN_4 moiety compared to FeN_3, FeN_2, or FeN_2C_2 moieties, which was accomplished by the DFT method [32, 79]. The formation of pyridine moieties of FeN_4 was found to be more favorable in the micropores overlapping graphene sheets than at the edge or inside the graphene sheet [32, 77]. Based on this, the formation of structures requiring the presence of C_4N-type pyrrole rings was expected to be even more favorable when overlapping the edges of graphene pores than when located inside the graphene sheet. Additionally, the bridging structure would preferentially form between the zigzag graphene edges. The DFT-D calculations performed for such a model FeN_4C_{12} cluster with a zigzag edge were compared with the results for the $FeN_{(2+2)}C_{(4+4)}$ and FeN_4C_{10} fragments. The Fe-N bond lengths found for the FeN_4C_{12} cluster are in good agreement with the lengths determined by EXAFS and XANES for the FeN_4C_{12} cluster without oxygen or with one or two O_2 molecules adsorbed in the axial position (see Table 1). The strong binding of Fe(II) to the nitrogen atoms in the porphyric structure is evidenced by the B_E of about -7 eV, comparable with that calculated for the $FeN_{(2+2)}C_{(4+4)}$ and FeN_4C_{10} clusters. The B_E of Fe(II) to the O_2 molecule was calculated for FeN_4C_{10} and FeN_4C_{12} clusters. The DFT-D results for the truncated FeN_4C_{12} cluster with one O_2 molecule adsorbed in the configuration with the O-O axis perpendicular to the plane of nitrogen

atoms showed that Fe(II) is out of plane by 0.2 Å, and a Fe(II)-O bond of 1.786 Å length is formed. The adsorption energy of O_2 is 1.83–1.84 eV for FeN_4C_{10} and FeN_4C_{12} clusters. The geometrical and energy characteristics of the FeN_4C_{10} cluster obtained by the DFT-D method are in complete agreement with the previous results [78].

Thus, the performed quantitative analysis of the regions of the EXAFS and XANES spectra of FeN-C catalysts free or nearly free of Fe crystalline structures revealed the existence of porphyrinic FeN_4C_{12} molecules, which is in strong contrast to the previously proposed FeN_xC_y fragments with nitrogen atoms included in six-membered rings [81]. Electrochemical studies show that such compounds catalyze the four-electron reduction of the O_2 molecule to water. Due to their geometric structure, porphyrin compounds can be formed either in highly disordered graphene sheets or between zigzag graphene edges, forming micropores. Despite the virtually identical FeN_4C_{12} molecules, FeN-C catalysts subjected to Ar pyrolysis and NH_3 pyrolysis demonstrate completely different activities in ORR. The increase in ORR activity caused by the FeN_4C_{12} fragment is due to the highly basic N-groups formed during pyrolysis with NH_3. The results of [81] pave the way for the use of the XANES method for the structural study of G-based TMN-C electrocatalysts. This class of transition metals is widespread on Earth and is promising for important electrochemical reactions.

FOUR- AND TWO-ELECTRON MECHANISMS OF OXYGEN REDUCTION REACTIONS CATALYZED BY IRON-CONTAINING GRAPHENES

Fe- and Co-based catalysts are, in general, still inferior in several respects to catalysts using Pt [97]. Bridging the remaining gap in activity and stability between TMN_x-C and Pt-containing catalysts requires a thorough study of the properties of the oxygen reduction active sites to provide a better understanding of the ORR mechanism [62]. The performance of TMN_x-C catalysts in ORR depends on the catalyst structure, namely the type of nitrogen atoms (graphite, pyridine, or pyrrole), the nature of the TM, the number of N atoms coordinating the TM atom, and the morphology of the C-containing material. Numerous studies have reported that the abundance of TM-N_4 motif structures is higher at low temperatures, favoring the reduction of O_2 to H_2O_2. In contrast, at high temperatures, the TM-N_2 active site is formed, directing the ORR via a four-electron mechanism with water formation [70, 72, 98, 99]. In [70, 99, 100], it was demonstrated that the FeN_2-C fragment is more electrocatalytically active than the FeN_4-C fragment. Further studies have shown that the $FeN_{(2+2)}$-C fragment, which connects two adjacent graphite crystallites, is a potential model for most catalytic sites in FeN_x-C type catalysts [72, 101]. The catalytic site of the $FeN_{(2+2)}$-C fragment is based on the FeN_2-C structure with all pyridine Ns in the phenanthroline configuration. Still, it differs from the FeN_4-C fragment, which has all pyrrole nitrogen atoms. The FeN_4-C fragment is much more difficult to insert into the graphene lattice than FeN_2-C due to its high symmetry [72]. DFT calculations also showed that the formation of pyridine FeN_x structures is more favorable than pyrrole ones [102]. However, in [104–105] it was revealed that the obtained catalysts, with the Fe atom coordinated by four pyrrole nitrogen atoms (FeN_4 motif) embedded in the surface of the carbon material, have an activity comparable to the above-described FeN_x type catalysts. In addition, in [106], a FeN-C catalyst based on modified G with an average coordination of the Fe atom by three N atoms was reported, which demonstrated increased ORR activity, high stability, and a low yield of H_2O_2 in an acidic medium. Also in [32], it was found that the FeN_3 and CoN_3 configurations are stable with negative formation energies.

The optimal active structure of the catalytic center in ORR remains unclear. Several theoretical calculations have been performed to elucidate the active center structure and the reaction mechanism of ORR under the action of TMN_x-C catalyst [32, 93, 107, 108]. Based on the energies of O_2 adsorption and the formation of the corresponding intermediate products on the surface of the MN_x-C catalyst, all calculations led to an active site of the TMN_x-C type. It

was found that the graphitic configuration of MN_4 is energetically favorable and stable in the region of real working potentials [93, 107, 108]. Taking into account the weak interaction between the peroxide and CoN_4-C, it was suggested in [93] that CoN_4 does not promote the complete ORR, and an active site of a different structure is required for peroxide reduction. It was found in [107] that the adsorption behaviour of transition metals is not an intrinsic property, since it can be strongly modified by changing the local geometry of the active site, the chemical nature of the nearest neighbors, and the oxidation state. It was reported in [108] that the iron-containing regions of FeN_4-C nanotubes are stable adsorption sites for O_2 molecules and all intermediate products, which is similar to the ORR behaviour on metal-N_4 macrocycles. In [102], experimental and theoretical methods were combined to elucidate the ORR mechanisms using FePc and CoPc as catalysts. It was suggested that ORR occurs via a four-electron mechanism on FePc catalysts and via a two-electron mechanism on CoPc catalysts, which is consistent with the results of [110]. The studies mentioned above primarily focused on thermodynamic information, such as adsorption energy and/or the Gibbs free energy change. However, the detailed kinetic behaviour of TMN_x-C catalysts was not considered in these studies. This information is important for the design and optimization of the catalyst structure and performance. Previously [111], the ORR kinetics were reported on the FeN_4-graphene model with all pyridinic-N atoms.

In [112], DFT calculations were used to study the ORR on the surface of the FeN_4-graphene model with all pyrrolic-N atoms, FeN_4, which allowed focusing on the calculation of the energies of the involved elementary reaction steps. The parameterization of Perdue, Burke, and Ernzerhof in the generalized gradient approximation (GGA) [48, 113] was used to describe the electron exchange and correlation effects. The adsorption energy E_{ads} is defined as

$$E_{ads} = E_{tot} - E_{FeN4} - E_X, \quad (1)$$

where E_{tot}, E_{FeN4}, and E_X are the total energies of FeN_4-G with an adsorbed particle X, the FeN_4-G catalyst, and the isolated particle X, respectively. The negative adsorption energy indicates that it is energetically favourable for the adsorbate molecule to attach to the surface of the FeN_4-G catalyst. The formation energy (E_f) was calculated according to the expression.

$$E_f = E_{FeN4} - G + y\mu_C - E_G - x\mu_N - E_{Fe}. \quad (2)$$

Here E_G is the energy of the optimized sheet of the ideal sheet G. The μ_C is the chemical potential of carbon atom, defined as the total energy per carbon atom for ideal G. The μ_N is the chemical potential of the nitrogen atom, defined as half the total energy of the N_2 molecule, and E_{Fe} is the total energy of an isolated Fe atom in the gas phase, x is the number of embedded nitrogen atoms, and y is the number of carbon atoms removed from the graphene sheet during defect formation. A higher (more positive) formation energy means that the presence of a defect in the equilibrium state is less likely [93]. The bond energy B bond of an Fe atom in the FeN_4-G fragment is calculated as:

$$B_{bond} = E_{FeN4\text{-}G} - E_{N4\text{-}G} - E_{Fe}, \quad (3)$$

where $E_{N4\text{-}G}$ is the energy of the FeN_4-G fragment without the Fe atom. The full LST (linear synchronous transit)/QST (quadratic synchronous transit) method was used to calculate the energy barrier of each elementary stage in the search for the transition state [114].

According to the approach developed in [115], the free energies of formation of ORR intermediates can be calculated. The expression determines the change in free energy for an elementary step:

$$\Delta G = \Delta E + \Delta ZPE - T\Delta S + \Delta G_{pH} + \Delta G_U + \Delta G_{field}, \quad (4)$$

where ΔE is the reaction energy obtained from DFT calculations, ZPE is the zero-point energy, T is the temperature equal to 300 K, and ΔS is the entropy change. The ZPE and S values of the

ORR intermediates are calculated based on the vibrational frequencies of their atoms. ΔG_{pH} and ΔG_U are the contributions to the free energy due to the changes in the pH value and the electrode potential U, respectively. ΔG_U = -neU, where n is the number of transferred electrons and U is the electrode potential relative to the standard hydrogen electrode (SHE). ΔG_{pH} = $-k_B T \ln 10$ = $pH \times k_B T \ln 10$, where k_B is the Boltzmann constant. In [115], the pH value is taken to be zero for an acidic medium. The effect of the electrochemical double layer was found to be insignificant for the ORR intermediates and does not significantly affect the results of [115]. The free energy of formation of H_2O was calculated for the gas phase at 300 K. A pressure of 0.035 bar, since at this pressure the gas phase H_2O is in equilibrium with liquid water at 300 K. The free energy of O_2 was obtained from the reaction $O_2 + 2H_2 = 2H_2O$, for which the change in free energy was 4.92 eV.

In the calculations in [112], a periodic (6 × 6) supercell G with a FeN_4-coordinated structure was used, in which the Fe atom is surrounded by four pyrrole nitrogen atoms (Fig. 4).

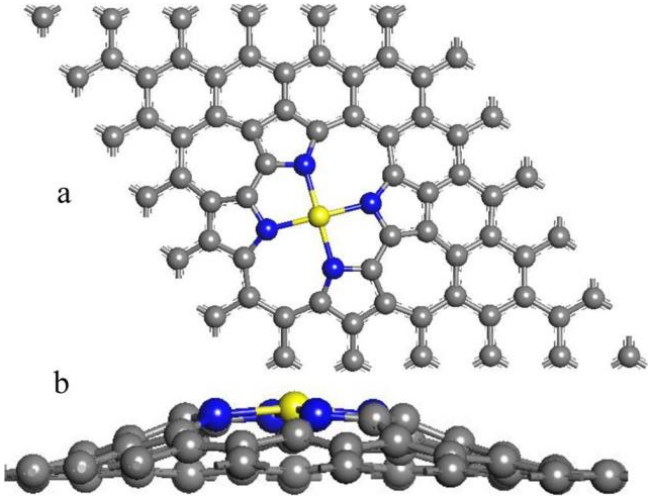

Fig. 4. Top (*a*) and side (*b*) views of the most stable configurations of FeN_4-G. Gray, yellow, and blue spheres represent C, Fe, and N atoms, respectively [112]

After optimization, the FeN_4-G fragment was found to be highly deformed. The entire FeN_4 fragment and the C atoms located near the N atoms protrude from the G plane, forming a lid-like relief (Fig. 3*b*). The height of the Fe atom above the G plane was 1.43 Å. The four Fe-N bonds are nearly equivalent, with an average bond length of 1.91 Å, which is close to the results (1.90 and 1.92 Å) [102]. The formation energy of the FeN_4-G fragment was 1.17 eV, indicating that its formation is energetically unfavorable. However, the interaction of the Fe atom with the surface is powerful, with a bond energy of -9.24 eV. Thus, the FeN_4-G structure is not easily formed, but once it has formed under certain conditions, the strong bond interaction makes it stable.

The adsorption of the O_2 molecule was considered for several possible initial positions relative to the Fe atom of the FeN_4 group. Preliminary calculations indicate that the O2 molecule can be chemisorbed only on the Fe atom; therefore, the Fe atom should be considered the active center of the FeN4-G catalysts, a conclusion also supported by specific experimental evidence [105, 111, 116, 117]. The O_2 molecule can be bound to the Fe atom either through one of its atoms (Pauling model) [118] or by both of its atoms (Griffiths model) [119]. Both configurations are energetically favourable for the adsorption of the O_2 molecule on FeN_4-G. For the Pauling model, two different stable configurations are possible, i.e., either with one oxygen atom tilted toward the formed five-membered ring (model P1) or toward the seven-membered ring (model P_2). For models P1 and P2, E_{ads} is - 0.91 and -0.95 eV, the O–O bond lengths are 1.225 and 1.278 Å, and the distances between the Fe atoms and the two O atoms are 1.740 and 1.734 Å, respectively. Thus, the two configurations, P1 and P2, of the adsorption complex are practically identical. In the Griffiths adsorption model, the O_2 molecule is located parallel to the catalyst surface with an adsorption energy of -0.70 eV, which is similar to the adsorption complex of the

O_2 molecule with FePc [120]. The O–O bond center is located above the Fe atom, and the distances from the Fe atom to the two O atoms are 1.90 Å. The O–O bond length is 1.334 Å. An analysis of the atomic population showed that in the Griffiths model configuration, there is a greater charge transfer from the catalyst to the adsorbed O_2 molecule than in the Pauling configurations [120, 121].

Initially, the direct dissociation of the O_2 molecule was considered:

$$O_{2(ads)} \rightarrow 2O_{(ads)}. \quad (5)$$

The index (ads) indicates the adsorbed state of the O_2 molecule. The dissociation reaction (5) is strongly endothermic, with the reaction energy (E_{react}) equal to 1.81 eV. The activation barrier (E_{act}) of this process is 2.54 eV, which is too high to be overcome at the fuel cell operating temperature (approximately 80°C). Both the reaction energy and the activation barrier indicate that O_2 dissociation at the active site of FeN_4-G is impossible.

As an alternative to step (5), the $O_{2(ads)}$ molecule can simultaneously capture one proton H^+ and one electron $e^–$, which is equivalent to the addition of one hydrogen atom, to form the $OOH_{(ads)}$ group. The equation can express this step:

$$O_{2(ads)} + H^+ + e^– \rightarrow OOH_{(ads)}. \quad (6)$$

Under ORR conditions, there are two possible mechanisms for the transformation of the adsorbed OOH fragment $_{(ads)}$: a two-electron mechanism, in which the H atom ($H^+ + e^–$) is added to form H_2O_2, and a four-electron mechanism, according to which the O–OH bond is broken, which leads to the formation of the final product, the H_2O molecule.

The cleavage of the O–OH bond indicates a possible four-electron reaction mechanism [122]. Dissociation of the adsorbed OOH fragment $_{(ads)}$ can occur via three possible routes (equations 7–9):

$$OOH_{(ads)} \rightarrow O_{(ads)} + OH_{(ads)}, \quad (7)$$

$$OOH_{(ads)} + H^+ + e^– \rightarrow H_2O_{(ads)} + O_{(ads)}, \quad (8)$$

$$OOH_{(ads)} + H^+ + e^– \rightarrow 2OH_{(ads)}. \quad (9)$$

The direct dissociation route of the $OOH_{(ads)}$ fragment is expressed by equation (7). This reaction is endothermic, with E_{react} equal to 0.40 eV and E_{act} equal to 0.94 eV in the FeN_4-G model. Instead of direct cleavage of the O–OH bond in the $OOH_{(ads)}$ fragment, its modification can occur by inserting an H atom into it. In this case, the kinetics of the route strongly depend on the position of the inserted H atom due to the spatial asymmetry of the $OOH_{(ads)}$ fragment. If an H atom is inserted into the FeO–OH bond, then dissociation of $OOH_{(ads)}$ under the action of H produces $H_2O_{(ads)}$ + $O_{(ads)}$ (equation 8). This process is thermodynamically and kinetically favorable, with E_{react} = -2.32 and E_{act} = 0.19 eV. Note that the formed H_2O molecule drifts away from the Fe atom (the smallest distance between the H_2O molecule and the Fe atom exceeds 3.00 Å). The O atom remains adsorbed on the Fe atom, with whose participation the further reduction reaction can occur. However, when the hydrogen atom is introduced into the Fe–OOH bond, reaction (9) is realized. This process is also thermodynamically and kinetically favorable, E_{react} = -1.75 eV and E_{act} = 0.29 eV. Among the three possible routes of $OOH_{(ads)}$ dissociation, more than one reaction is favorable. The barriers of reactions 7 (0.19 eV) and 8 (0.29 eV) are so low that they can be easily overcome with the formation of intermediate products $O_{(ads)}$ and $OH_{(ads)}$. Therefore, further reduction of $O_{(ads)}$ to H_2O occurs according to reactions (10) and (11):

$$O_{(ads)} + H^+ + e^– \rightarrow OH_{(ads)}, \quad (10)$$

$$OH_{(ads)} + H^+ + e^– \rightarrow H_2O_{(ads)}. \quad (11)$$

The isolated $O_{(ads)}$ atom formed in reaction (7) remains chemisorbed on the Fe atom of the FeN_4-G group with an adsorption energy of -4.33 eV. Subsequently, the H atom ($H^+ + e^-$) is added to the oxygen atom of $O_{(ads)}$ to form the $OH_{(ads)}$ fragment, E_{ads} of this stage is -2.82 eV. When another hydrogen atom ($H^+ + e^-$) is introduced into the system, the $OH_{(ads)}$ fragment is further reduced to form a second $H_2O_{(ads)}$ molecule. Reactions (5–11) occur in fuel cells in the presence of water, and the Fe atom is the only active center for the O_2 molecule. When comparing the adsorption energies of the $O_{2(ads)}$ and $H_2O_{(ads)}$ molecules, it is seen that the adsorption energy of H_2O on the Fe atom is -0.51 eV, which is lower in absolute value than that of the O_2 molecule. Therefore, the O_2 molecule will be preferentially adsorbed on the Fe atom rather than the H_2O. This result is consistent with the ORR results on FePc [109].

Reactions 10 and 11 are characterized by negative E_{react} values of -1.53 and -1.07 eV, respectively, indicating their high exothermicity and high thermodynamic probability of occurrence. However, their activation barriers are quite high. E_{act} of the reactions 10 and 11 is 0.81 and 1.02 eV, respectively. OH reduction is another important step in the ORR via the four-electron mechanism. This stage is crucial for the formation of the H_2O molecule; a high E_{act} value results in low efficiency of the four-electron ORR mechanism.

Based on the calculated E_{act} values, the most favourable four-electron ORR mechanism was determined. In the FeN_4-G model, this mechanism consists of the following sequence of elementary steps: reduction of an O_2 molecule to OOH, hydrogenation dissociation of OOH to form H_2O and O or two OH groups, reduction of an O atom to OH, and reduction of OH to a second H_2O molecule. The highest barrier (1.02 eV) is inherent in the step of $OH_{(ads)}$ reduction to $H_2O_{(ads)}$, which is the rate-limiting step of the entire process. This step differs from the step for the FeN_4-graphene model with all pyridine N atoms [111], in which the initial step of $O_{2(ads)}$ reduction to $OOH_{(ads)}$ is decisive. The highest activation barrier is inherent in the last step, indicating that O_2 reduction can end at the two-electron step to form H_2O_2.

The equation describes the first stage of the two-electron mechanism.

$$OOH_{(ads)} + H^+ + e^- \rightarrow H_2O_{2(ads)}. \quad (12)$$

After the formation of the adsorbed $OOH_{(ads)}$ fragment according to reaction (12), another H atom ($H^+ + e^-$) enters the reaction system. This H atom is localized near the O atom, which is bonded to the Fe atom, forming the H_2O_2 molecule. The reduction of $OOH_{(ads)}$ to H_2O_2 is an exothermic reaction with E_{react} = -0.62 eV, and the active barrier is 0.91 eV. For the optimized structure of H_2O_2 adsorbed on FeN_4-G, the O–O bond length in the $H_2O_{2(ads)}$ fragment is 1.828 Å, which is significantly longer than that of the free H_2O_2 molecule (1.472 Å), as in the cases of FePc [109] and FeN_4-G with all pyridine nitrogen atoms [111]. The dissociation reaction can be expressed by equation (13).

$$H_2O_{2(ads)} \rightarrow 2OH_{(ads)}. \quad (13)$$

The E_{react} of this step is -0.89 eV, indicating that it is exothermic. Importantly, this step has a low E_{act} (0.57 eV), suggesting that although H_2O_2 can be chemisorbed on FeN_4-G, it is unstable and can easily dissociate into two $OH_{(ads)}$ moieties. However, once formed, the OH species will subsequently be reduced to H_2O. The OH reduction reaction discussed above has a high E_{act} = 1.02 eV. The high barrier indicates a low reaction rate, resulting in a significant accumulation of OH species on the surface. Excess OH species can shift the equilibrium of reaction (13) to form H_2O_2. The high barrier of OH reduction slows down the H_2O_2 dissociation reaction.

Alternatively, the H_2O_2 molecule can be desorbed from the surface. The desorption energy of H_2O_2 is 0.55 eV, which is slightly lower than the dissociation barrier of H_2O_2 (0.57 eV), which is easily overcome. Thus, the desorption of H_2O_2 favours the formation of $H_2O_{2(ads)}$, which determines the most favourable route of the two-electron ORR reaction. The steps are in the following order: reduction of O_2 to OOH, reduction of OOH by hydrogenation to

form H_2O_2, and then desorption of the adsorbed H_2O_2 molecule from the surface. The highest barrier (0.91 eV) occurs for the reduction step of $OOH_{(ads)}$ to $H_2O_{2(ads)}$, which acts as the rate-determining step of the overall reaction.

Table 2 shows the calculated values of E_{reac}, E_{act}, E_{ads}, and E_{dis} for all elementary stages occurring via four- and two-electron mechanisms. Some structural parameters of the reaction centres are also given.

To investigate the presence of a thermodynamic step determining the ORR rate, ORR free energy diagrams in acidic media were calculated for FeN_4-G catalysts with H_2O_2 and H_2O as stable end products, respectively (Figs. 5 and 6).

Table 2. Energy parameters of intermediate stages of ORR via the four-electron route

	E_{ads}, eV	**E_{react}, eV**	**E_{act}, eV**	**E_{dis}, eV**	**R(O-O), Å**	**R(Fe-O), Å**
$FeN_4N\ O_2$					1.225	1.740
Model P1	-0.91				1.278	1.740
Model P2	-0.95				1.334	1.900
Model G	-0.70					
$O_{2(ads)} \rightarrow 2O_{(ads)}$			2.54	1.81		
$O_{2(ads)} + H^+ + e^- \rightarrow OOH_{(ads)}$		0.55	0.53			
$OOH_{(ads)} \rightarrow O_{(ads)} + OH_{(ads)}$ (direct)		0.40	0.94			
$OOH_{(ads)} + H^+ + e^- \rightarrow H_2O_{(ads)} + O_{(ads)}$ $FeO\text{-}OH + H^+ + e^-$		-2.32	0.19			
$OOH_{(ads)} + H^+ + e^- \rightarrow H_2O_{(ads)} + O_{(ads)}$ $Fe\text{-}OOH + H^+ + e^-$		-1.75	0.29			
$O_{(ads)}$	-4.33					
$O_{(ads)} + H^+ + e^- \rightarrow OH_{(ads)}$		-1.53	0.81			
$OH_{(ads)}$	-2.82					
$OH_{(ads)} + H^+ + e^- \rightarrow H_2O_{(ads)}$		-1.07	1.02			
$H_2O_{(ads)}$	-0.51					

Based on the diagrams of free energy changes constructed in theoretical calculations in [112], it was concluded that the reduction of OOH to H_2O_2 (Fig. 5) is associated with negative changes in free energy for all positive potential values (U > 0 V). Therefore, the thermodynamic stage that determines the rate of two-electron reduction is the last stage of OOH reduction to H_2O_2 with $\Delta G = 0.27$ eV at zero potential. The high positive value of ΔG for H_2O_2 formation indicates that the catalytic activity of ORR by the two-electron mechanism is very low. A significantly different picture is obtained for ORR by the four-electron mechanism, for which, at a low potential value, the transition from stage to stage is due to negative values of the change in free energy (Fig. 6). At a higher potential exceeding 1.03 V, the reduction of O to OH and O_2 to OOH occurs with an increase in free energy. Overall, the free energy diagrams indicate that the ORR via the four-electron mechanism is facilitated at low potentials, and the rate-determining thermodynamic step is the final step of OH reduction to H_2O.In the most favourable four-electron mechanism, ORR proceeds through four main steps, which are characterized as an oxygen reduction process. Chemisorbed $O_{2(ads)}$ is initially hydrogenated to $OOH_{(ads)}$, which then undergoes a hydrogenation dissociation reaction to form $O_{(ads)}$ and $H_2O_{(ads)}$. $O_{(ads)}$ is subsequently hydrogenated to $OH_{(ads)}$ and finally to H_2O. The free energies of all elementary steps of ORR by the four-electron mechanism decrease at low electrode potential (down to 0.41 V compared to the standard hydrogen electrode). For the reduction of $OH_{(ads)}$ to H_2O, the activation barrier is highest ($E_{act} = 1.02$ eV) and the value of $\Delta G = -0.41$ V, which makes this step rate-limiting in the four-electron mechanism. This condition is similar to the outcome of ORR over a platinum catalyst [123–125], in which the rate of $OH_{(ads)}$ elimination or protonation determines the overall ORR rate. However, the behavior of ORR over a platinum catalyst differs from that of the FeN_4-G model with all pyridine nitrogens [111], in which the initial reduction step of $O_{2(ads)}$ to $OOH_{(ads)}$ is rate-limiting. Furthermore, in the FeN_4-G model with all pyridine nitrogens, the rate-

determining step E_{act} is only 0.62 eV, which is lower than that of the FeN_4-G model with all pyrrole Ns (1.02 eV). After comparing the barriers to the rate-limiting steps of ORR in two different FeN_4-G models, the ORR activity in the FeN_4-G model with all pyridine nitrogen atoms is higher than in the FeN_4-G model with all pyrrole nitrogen atoms. In the two-electron ORR mechanism, the reaction proceeds through two main steps. Chemisorbed $O_{2(ads)}$ is initially hydrogenated to $OOH_{(ads)}$, which then undergoes a reductive hydrogenation reaction to form $H_2O_{2(ads)}$. The free energy changes in the reduction of OOH to H_2O_2 are positive at any positive electrode potential compared to the standard hydrogen electrode. The highly positive ΔG value for H_2O_2 formation indicates that the two-electron ORR mechanism is unfavourable.

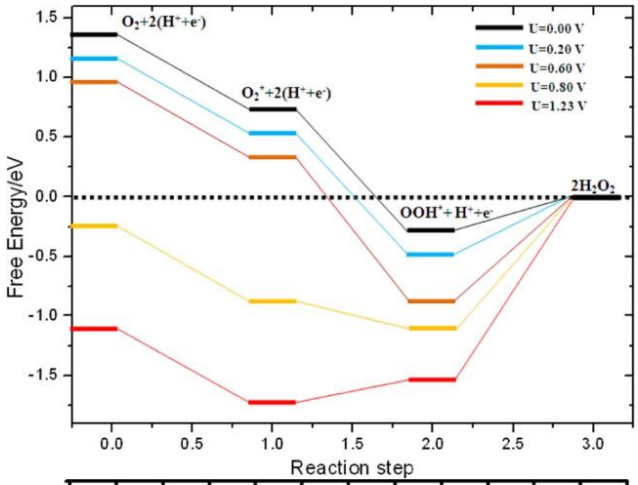

Fig. 5. Free-energy diagram for the reduction of O_2 into H_2O_2 on the FeN_4-G in acidic medium. The ∗ denotes the adsorption on the surface [112]

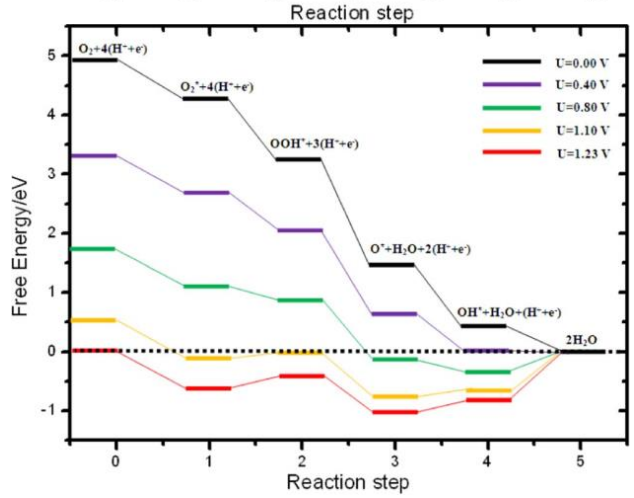

Fig. 6. Free-energy diagram for the reduction of O_2 into H_2O on the FeN_4-G in acidic medium. The ∗ denotes the adsorption on the surface [112]

Thus, the DFT calculations of the detailed kinetic and thermodynamic course of ORR on a FeN_4-G catalyst with all pyrrole nitrogen atoms performed in [112] showed that E_{act} of dissociation of an adsorbed O_2 molecule is very high regardless of whether it is adsorbed on the FeN_4-G catalyst in the Pauling or Griffiths model configuration. The most probable stages of the four-electron reduction mechanism can be arranged in the following order:

$$O_{2(ads)} \rightarrow OOH_{(ads)} \rightarrow O_{(ads)} + H_2O_{(ads)} \text{ (or } 2OH_{(ads)}) \rightarrow OH_{(ads)} + H_2O_{(ads)} \rightarrow 2H_2O_{(ads)}. \quad (13)$$

The free energy diagrams show that for all elementary steps of ORR via the four-electron mechanism, the free energy changes are negative at low electrode potential (up to 0.41 V). The rate-limiting step for the overall ORR is the reduction of $OH_{(ads)}$ to $H_2O_{(ads)}$, with E_{act} = 1.02 eV. The product of the two-electron reduction, H_2O_2, can be chemisorbed on the catalyst surface. Still, the free energy diagrams show that the decrease in OOH to H_2O_2 occurs at positive free energy changes for any positive electrode potential compared to the conventional hydrogen electrode. The high positive ΔG for hydrogen peroxide formation indicates that the two-electron ORR route is unfavourable on FeN_4-G type catalysts.

CLUSTERING OF Fe_xN_y FRAGMENTS IN GRAPHENE NANORIBBONS

Graphene nanoribbons (GNRs) are two-dimensional carbon sheets with zigzag edges that have been used as a model system for precious metal-free carbon catalysts [126] because they can contain various ORR catalytic sites, which is consistent with experimental facts for sp^2 hybridized carbons. It has been demonstrated that the combination of structural defects, embedded nitrogen atoms, metals, and vacancies can form active sites [127]. Such sites are usually more stable at the edges of graphene sheets than in bulk G [94, 128]. The marginal location of these defects is an important condition for the accessibility of products and reactants to them, which contributes to the efficiency of mass transfer. The marginal regions of nanocarbon clusters also have unique electronic and magnetic properties [128, 129], which distinguish them from areas in the bulk G [93, 107, 130].

TT maintain the optimal configuration of the catalytic centres in working condition, they must be covalently embedded in the planar structure of the graphene matrix. It has been shown [127] that nitrogen atoms coordinate non-precious metal atoms directly. However, the nature of catalytic fragments of the $(TM_x)N_{y\ type}$ remains actively discussed in the literature [32, 93, 107–109, 130]. The stability of any particular catalytic site $(TM_x)N_y$ will depend on the chemical potentials of the TM and N atoms introduced into the graphene network under the synthesis conditions, a fact that has not been sufficiently covered in the literature. It has also been suggested that the catalytic site may include several metal atoms in close association, and that this facilitates the multi-electron reduction steps of ORR [131–133].

In the work [79], the DFT and ab initio molecular dynamics (MD) methods are used to characterize the properties of the active sites of the iron-doped catalysts. The main attention is focused on their molecular structure, surface accessibility, sensitivity to the chemical potentials of N and Fe atoms, and the features of the reaction in an aqueous medium. The clustering tendencies of different N-coordinated fragments are analyzed to establish the structure of the $(TM_x)N_y$ catalytic sites. Finally, the adsorption of O_2 molecules on various types of $(TM_x)N_y$ sites embedded in G edge defects and its consequences for ORR are considered.

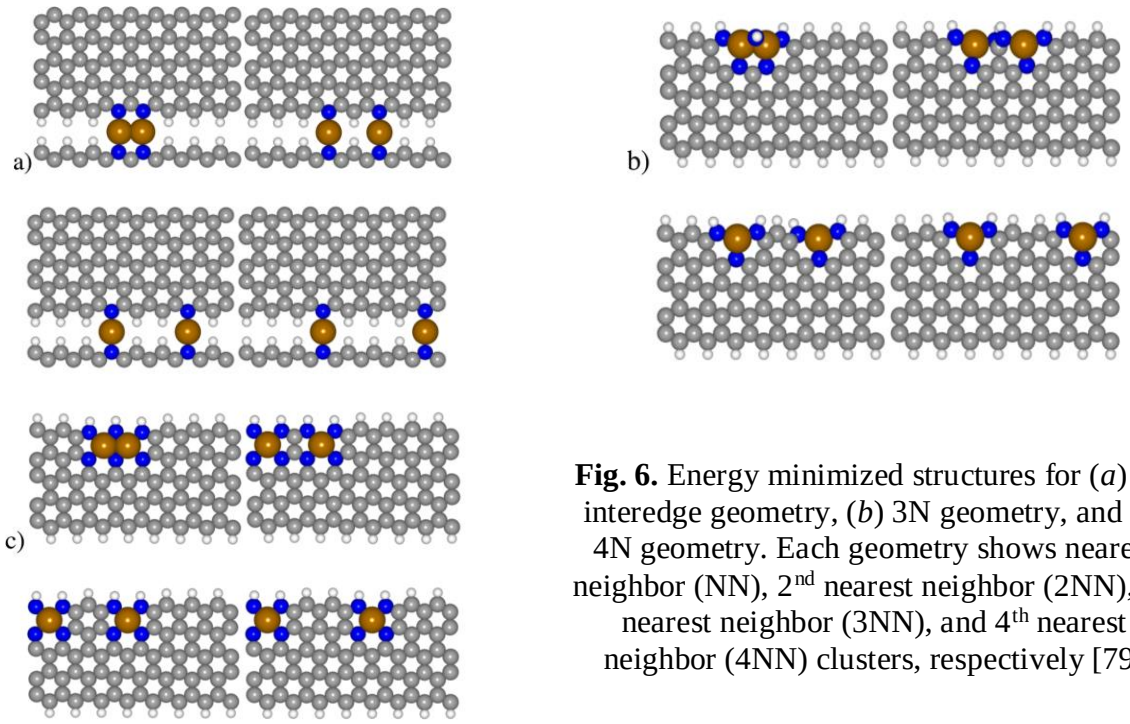

Fig. 6. Energy minimized structures for (*a*) 2N interedge geometry, (*b*) 3N geometry, and (*c*) 4N geometry. Each geometry shows nearest neighbor (NN), 2nd nearest neighbor (2NN), 3rd nearest neighbor (3NN), and 4th nearest neighbor (4NN) clusters, respectively [79]

To consider the formation of active catalytic centres $(Fe_x)N_y$, three of their possible configurations were used: 2N-coordinated interedge, 3N-coordinated intraedge, and 4N-coordinated intraedge. These configurations consist of Fe atoms located between the N-

containing zigzag edges of graphene sheets (crystallites); Fe atoms localized above or in single vacancies and coordinated by three nitrogen atoms (two of which are on the teeth of the zigzag edge); Fe atoms located in divacancy positions coordinated by 4 N atoms (two of which are on the teeth of the zigzag edge) (see Fig. 7). For the 3N and 4N configurations, a graphene nanoribbon of 8 carbon pairs in length and five carbon pairs in width with two FeN_x defects of a given geometry is used, which allows for possible clustering of defects of 2, 3, and 4 carbon pairs located along the zigzag edges. In the case of the 2N-coordinated structure, lower formation energies are achieved by using a ribbon of six carbon pairs in width. This arrangement allows localization of the Fe atom between two edge nitrogen atoms (Fig. 7*a*), which leads to a more stable configuration compared to the stepped one realized by a ribbon of five carbon pairs in width. Having calculated the formation energies of defect clusters for all admissible distances between Fe atoms, one can estimate the tendency for clustering of defects of a particular type.

The energies of cluster formation were calculated using the DFT method, and the generalized gradient approximation parameterized by Perdue, Burke, and Erzerhoff [113, 134] was used for the exchange and correlation components.

The energies of formation are calculated as follows:

$$G_{defect} = E_{defect} + \Delta n_C \mu_C + \Delta n_H \mu_H - \Delta n_N \mu_N - \Delta n_{Fe} \mu_{Fe} - E_{GNR}, \quad (14)$$

where μ_x is the chemical potential of the atom x, E_{defect} is the energy of a specific Fe_xN_y structure, and E_{GNR} is the energy of the nanoribbon without Fe and N atoms. When calculating the energy of the initial state for chemical potentials, the energy of one C atom in bulk G for carbon, 1/2 the energy of an N_2 molecule for nitrogen, the energy of one Fe atom in the bulk phase of iron for Fe, and 1/2 the energy of an H_2 molecule for hydrogen were used. Δn_x is the change in the number of atoms of the type x in a defective nanoribbon compared to a defect-free one. The entropy and zero-point energy were not taken into account, which, according to the authors [79], does not affect the results obtained.

The ab initio molecular dynamics (MD) simulations are performed with temperature scaling and using the Verlet algorithm. The time step is set to 1 fs. The temperature is held constant at 300 K. The MD simulations are used to study the reaction of the active sites in vacuum, as well as the possibility of coordination by the O_2 molecule and water in aqueous solutions at elevated temperatures.

Table 3. Distances between Fe atoms of FeN fragments x (Å) and energies of their formation (eV) [79]

Iron-containing multiatomic structure	Distances between Fe atoms of Fe-N fragments x (Å)	Formation energies (eV)
FeN_2NN	2.17	9.52
$FeN_{22}NN$	4.89	11.3
$FeN_{23}NN$	7.34	11.1
$FeN_{24}NN$	9.83	11.1
FeN_3NN	2.14	2.37
$FeN_{32}NN$	4.83	3.00
$FeN_{33}NN$	7.88	3.11
$FeN_{34}NN$	9.88	3.86
FeN_4NN	2.25	0.75
$FeN_{42}NN$	5.05	0.69
$FeN_{43}NN$	7.46	0.82
$FeN_{44}NN$	9.85	0.76

The equilibrium structures for each type of nitrogen coordination at optimal distances between Fe atoms are shown in Fig. 8. The calculated distances between Fe atoms and the formation energies are given in Table 3. The formation energies concerning the nearest neighboring cluster (clustering energies) as a function of the distances between Fe atoms are

shown in Fig. 9 for the three considered configurations, from which it is evident that the formation energy of different types of catalytic iron-containing centers depends differently on the distance between FeN_x defects. The 2N and 3N configurations are characterized by a thermodynamic preference for Fe-Fe clustering, while the formation energy of the 4N configuration is relatively insensitive to the distance between Fe atoms. At higher temperatures, entropic effects can change the obtained formation energies. The reference N_2 molecule, which has a higher entropy due to the increased number of degrees of freedom in the gas phase, will be more stable at high temperatures, resulting in an effective stabilization of lower nitrogen content structures (such as the 3N and 4N NN cluster configurations) compared to higher nitrogen content structures that have no nearest neighbors.

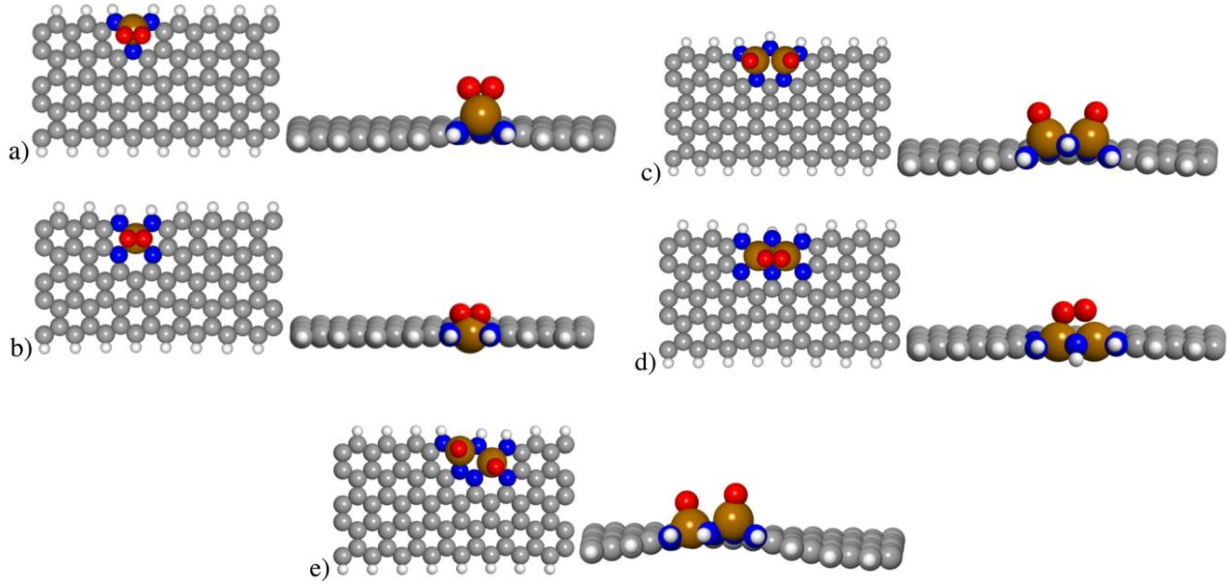

Fig. 8. Optimized geometries for (*a*) FeN_3 structure with adsorbed O_2; (*b*) FeN_4 structure with adsorbed O_2; (*c*) bimetallic FeN_3 cluster structure with adsorbed O_2; (*d*) bimetallic FeN_4 cluster structure with adsorbed O_2; (*e*) bimetallic FeN_3/FeN_4 cluster structure with adsorbed O_2. Each structure is shown from above and from the side [79]

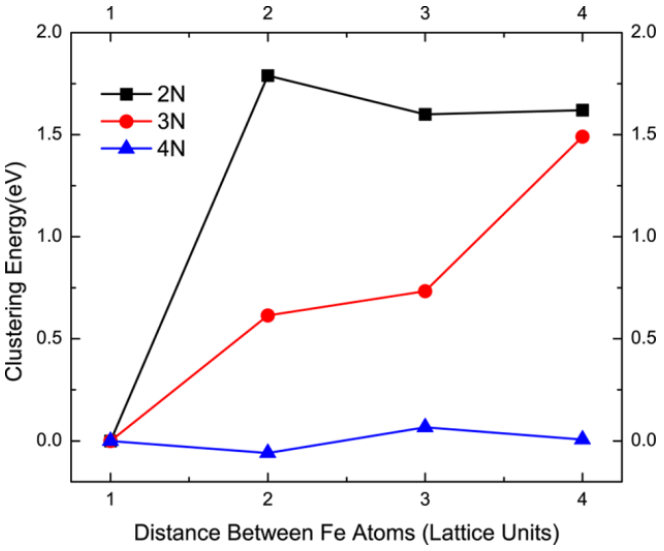

Fig. 9. Clustering energies as a function of Fe-Fe spacing following the structures depicted in Fig. 8 [79]

The results imply that the propensity of a given active site configuration to form multimetallic (i.e., cluster) configurations is minimally dependent on whether it is a 2N, 3N, or 4N type. Multimetallic active sites are more likely to catalyze ORR via unique routes. Moreover,

a potential route to tunable catalysis is opened by specially designing heterometallic clusters. This phenomenon may explain the enhanced activity of the synthesized Fe and Co catalysts [67].

According to the authors of [79], the initial stage of oxygen reduction involves the adsorption of the O_2 molecule on the active site. It is therefore important to consider this stage of adsorption and to compare the properties of different active sites. Geometry optimization using the DFT method revealed that bond cleavage in the O_2 molecule over the clustered region of FeN3 (i.e., Fe2N5) leads to the dissociation of the O_2 molecule. Such spontaneous cleavage of the O–O bond was reported in [135], where it was shown that this reaction on the Fe_2N_5 catalytic site occurs without a barrier. The ability of two incompletely coordinated Fe atoms to adsorb the formed O atom provides the driving force for the dissociation of the O_2 molecule. Since the dissociation of the oxygen molecule occurs spontaneously, the ORR dissociative pathway will likely happen on cluster bimetallic fragments of the Fe_2N_5 type. On isolated FeN_3 and FeN_4 fragments and the clustered Fe_2N_5 site, the O_2 molecule binds to the Fe atom(s), and the subsequent addition of the H atom results in the formation of a stable OOH species without dissociation of the O–O bond. This suggests that an associative mechanism is likely on such sites. This mechanism, which is generally less preferred, may result in the undesirable formation of H_2O_2 instead of H_2O. The mixed site of the bimetallic FeN_3/FeN_4 cluster also results in the dissociation of the O_2 molecule, suggesting that the presence of the FeN_3 fragment promotes dissociative adsorption. The structures with the dissociated O_2 molecule are shown in Fig. 8. These results indicate that the geometry of the catalytic site plays a crucial role in the ORR route and, consequently, in the selectivity of the four- and two-electron reactions. It is proposed that multimetallic defects at the edges of nanoribbons provide ideal active sites for reactions in which initial bond cleavage is a crucial step (e.g., ORR and possibly the electrochemical synthesis of ammonia).

Metal-nitrogen clusters, the structure of which is determined from ab initio calculations, may or may not be stable when exposed to an aqueous environment. To directly address this issue, ab initio MD simulations were performed on a system with a clustered FeN_3 site in the presence of solvent molecules at 300 K. Water molecules were arranged in a grid to a density of 1.0 g/cm^3 in the space outside the van der Waals volume in the vicinity of the graphene sheet. The system was then gradually heated to 300 K over a series of 0.5 ps, after which this temperature was held constant for 2.5 ps. A time step of 1 fs was used in the simulations. Although this time is insufficient for complete equilibrium to be reached at the catalyst/water interface (about 100 ps is required for this), it is sufficient to observe the reduction of water molecules around the active site. The results of ab initio MD simulations showed that water molecules are in equilibrium in the vicinity of the Fe_2N_5 catalytic site, where an O_2 molecule was introduced to replace the nearest water molecule above the active site. The geometry of the active site and water molecules is fixed while the other degrees of freedom are optimized. Then the active site itself is optimized while the oxygen molecule remains fixed. When the constraint on the position of the O_2 molecule is removed, it spontaneously dissociates in the presence of water, as in a vacuum. The energy released by O_2 bond dissociation is 3.96 eV (1.98 eV/atom).

Thus, for the first time, a self-consistent comparison of several potential structures of edge defects of the active center of a catalyst based on a non-precious metal in combination with graphene nanocarbon was carried out by the DFT method [79]. Based on the energies of formation of such Fe_xN_y centers, it was found that they thermodynamically lead to the formation of clusters. Moreover, depending on the synthesis conditions, the most stable Fe-containing defects are either 4N or 3N structures. It is assumed that both of these structures can coexist. The energy between the 2N ribbon configuration is so much higher than that of the other defects studied that its existence is assumed to be either thermodynamically forbidden or metastable relative to its decay. F_eN_3 (Fe_2N_5) cluster structures appear to be capable of cleaving the zero-barrier O_2 bond and may therefore direct ORR along a dissociative pathway. This pathway is

expected to be more selective, without H_2O_2 formation, due to excess binding of ORR intermediates. Ab initio molecular dynamics suggest that this spontaneous reaction is unlikely to be affected by solvation, as the solvent does not appear to impact the stability of the edge defects considered.

BALL-MILLED IRON-CONTAINING GRAPHENES IN THE DIRECT CATALYTIC CONVERSION OF BENZENE TO PHENOL

Many properties of catalysts containing single iron atoms embedded in a graphene matrix with or without nitrogen atoms have been discussed above. It was assumed by default that they were obtained by one or another chemical method, the most popular of which is the pyrolysis of precursors containing nitrogen, iron, and a carbon carrier. It is clear that with this approach, it is impossible to create a material with only one type of nitrogen-containing catalytic centers, which makes it extremely difficult to determine those properties that most contribute to a specific reaction. On the other hand, many successful examples can be found in enzymes such as cytochrome P-450 [136, 137], nitrogenase [138] and methane monooxygenase [139], as well as in some homogeneous catalysts where organic ligands and proteins surround iron atoms, making them highly active, selective and stable [136, 140–142], designed to perform specific functions in a living organism. Therefore, in heterogeneous catalysis, the preparation of single-atom iron-containing centers deposited on a catalyst support with a stable structure and high activity remains an urgent task [143–146].

Several studies [147–149] have demonstrated that a single metal atom, particularly iron, can be successfully incorporated into a graphene matrix in situ by electron beam irradiation using transmission electron microscopy (TEM). However, single metal atoms in G are mobile during irradiation [147, 148], which leads to instability of the catalyst under real conditions. Moreover, it isn't easy to obtain a sufficient amount of metal incorporated into the graphene matrix by the irradiation method for practical application. It has been proven that FeN_4-type centers with a Fe atom in organic macrocycles exist as stable structures. In contrast, FeN_4 macrocycles on a substrate are prone to aggregation during catalytic reactions due to weak interactions between these macrocycles and the substrate [150]. Therefore, one of the possible ways to stabilize the Fe atom sites in the graphene matrix is to introduce N atoms as an “anchor”, since the C–N bond has been shown [151, 152] to be highly stable in N-doped G.

Taking these factors into account, a methodology for obtaining highly dispersed isolated FeN_4 fragments with non-coordinatively saturated Fe atoms embedded in a graphene matrix in large quantities was developed in [153] by high-energy ball milling of iron phthalocyanine, FePc, and graphene nanosheets under controlled conditions. It was demonstrated that high-energy ball milling is a powerful method that allows breaking and creating new chemical bonds in materials or molecules with moderate energy costs [151, 154–156]. In [153], a series of FeN_4(FeN_4/G) catalysts with different iron contents, namely FeN_4/G-1.5 (1.5% Fe), FeN_4/G-2.7, and FeN_4/G-4.0, were prepared by ball milling FePc and GN composites with appropriate energy selection.

The prepared samples were examined using the HAADF-STEM (high-angle annular dark field) method. The results indicate that the Fe atoms are bonded with the N atoms in the graphene matrix environment, which is also in good agreement with the DFT simulation results. Note that some areas around the Fe atoms also exhibit disordered structures, indicating that defects in the graphene network around some iron atoms occur after high-energy ball milling. X-ray diffraction (XRD) and Raman spectra also show that no characteristic structural fragments in FePc, Fe, or FeO_x are observed in the FeN_4/G samples, indicating that the Fe atoms are well distributed in them. The TEM and HAADF-STEM results confirm this conclusion.

To obtain more information about the atomic and electronic structure of FeN_4 centers in the graphene matrix, LT-STM, 4 K (low-temperature scanning tunneling microscopy) was used.

The iron atom in the LT-STM image is resolved as a bright spot. The STM modeling of the FeN_4 center embedded in the G lattice is consistent with the STM image, indicating that the iron atom significantly changes the electron density of states of neighboring atoms, and the FeN_4 fragment is in the G plane, forming stable bonds with neighboring carbon atoms. To further study the chemical state and coordination structure of these FeN_4 centers, the XAFS method was used.

The above results demonstrated that FeN_4 fragments were successfully incorporated into the G matrix via high-energy ball milling of FePc and graphene. One proposed mechanism for their formation suggests that the outer macrocyclic structure of FePc could be disrupted during the milling process, leaving behind isolated FeN4 sites that interact with graphene at its defect sites. Carbon atoms adjacent to the FeN_4 fragment can be further reduced under the action of high milling energy, which ultimately leads to the formation of FeN_4 centers embedded in the G matrix. In [157], it was shown that isolated Fe atoms embedded in a silicide matrix exhibit high activity and long-term stability in the direct conversion of methane to ethylene and hydrocarbons. Thus, it is expected that such a graphene-framed single FeN_4 fragment will have high efficiency in catalytic reactions.

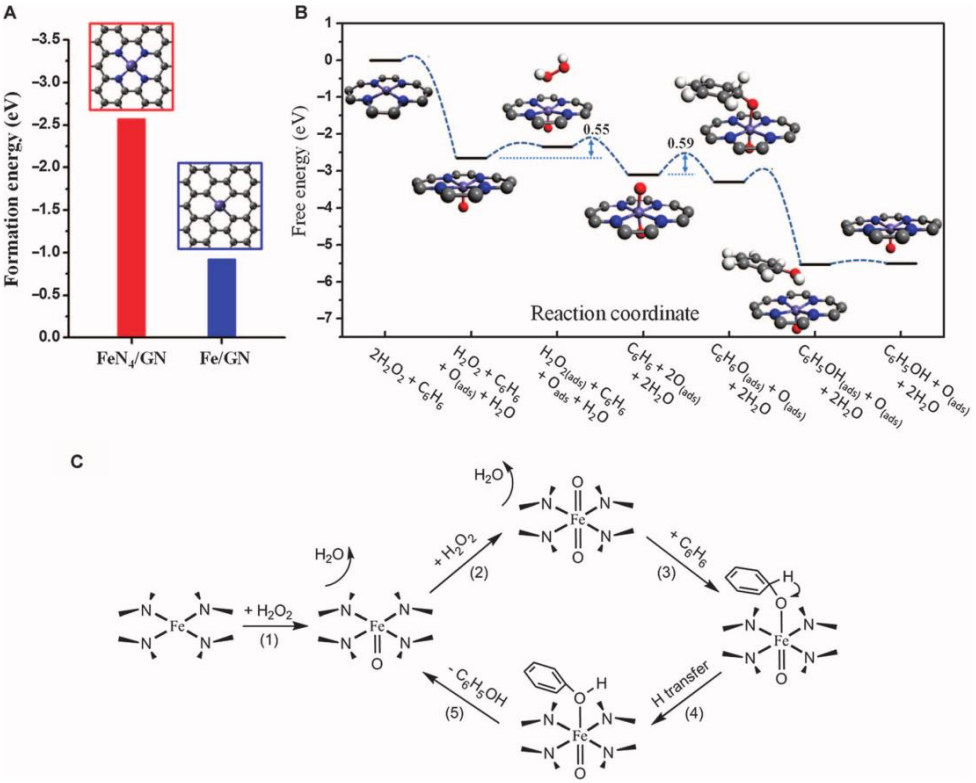

Fig. 9. Theoretical analysis of the FeN_4/GN structure and the catalytic reaction process by DFT calculations. (A) The formation energies of FeN_4/GN and Fe/GN structures. The formation energy is calculated as follows: $E_{Fe-embedded} - E_{Fe-bulk} - E_{(N)GN}$, where $E_{Fe-embedded}$ and $E_{Fe-bulk}$ are the total energies of FeN_4/GN and the Fe/GN structure and the Fe atom in the Fe bulk, respectively, and $E_{(N)GN}$ is the total energy of the optimized structure of FeN_4/GN or Fe/GN with the Fe atom removed from the system. (B) Free energy diagram of the oxidation of benzene to phenol on FeN_4/GN. The gray, blue, light blue, red, and white balls represent C, N, Fe, O, and H atoms, respectively. (C) Scheme for the reaction mechanism of the oxidation of benzene to phenol on FeN_4/GN [153]

The obtained and characterized isolated iron atom catalysts were applied in the direct catalytic conversion of benzene to phenol, which is one of the most critical reactions in fundamental and applied research [58, 159]. Various catalysts, including Ti-containing zeolites,

palladium membranes, and transition metal (Fe, Cu, and V) oxides or chelates, have been extensively studied as catalysts for the direct conversion of benzene to phenol. This reaction is typically carried out at temperatures between 50 and 140 °C since it is tough to carry out at room temperature due to the high stability of the C–H bond in benzene [158, 159–162]. Here, FeN_4/G samples were found to exhibit high activity and selectivity toward phenol at room temperature. Benzene oxidation was carried out at 25°C using hydrogen peroxide as the oxidizing agent. With the increase of iron content in G, the activity and yield of phenol first increased rapidly and then decreased. This tendency of change in efficiency with the increase of Fe content in G can be explained by the fact that the moderate amount of FeN_4 fragments may promote both their dispersion in graphene and their binding to G. In contrast, a higher content of FeN_4 fragments leads to their agglomeration. The optimized FeN_4/G-2.7 catalyst has a turnover rate of 84.7 h^{-1} for benzene conversion during the first 5 min and can provide a benzene conversion of 23.4% and a phenol yield of 18.7% in 24 h. (As is customary in heterogeneous catalysis, the activity of a catalyst can also be characterized by the number of revolutions (eng. Turnover number) of a catalyst, which is considered to be equal to the number of reagent molecules converted by one catalyst molecule per second. For nucleophilic and basic catalysts under normal conditions, this number is $10^{-7} – 10^{-2}$ s^{-1}, for acidic and electrophilic catalysts – $10^{-4} – 10^{-1}$ s^{-1}, for enzymes – up to 10^6 s^{-1}, and in the case of catalytically perfect enzymes – up to 4×10^7, as in the case of catalase.

To gain a deeper understanding of the activity of FeN_4/G in benzene oxidation, DFT calculations were performed in [153] to study the reaction mechanism. The model of the FeN_4 fragment embedded in G was adopted according to the experimental characteristics. As shown in Fig. 10*a*, the formation energy of the FeN_4 center in the graphene matrix (FeN_4/GN) is significantly lower than the insertion energy of a single Fe atom in pure graphene (Fe/GN). This suggests that N atoms can be used as anchors to enhance the stability of Fe atoms in the G network, which confirms the experimental results.

The H_2O_2 molecule readily dissociates on the FeN4 fragment to form an Fe=O intermediate and release one H_2O molecule, followed by dissociation of another H_2O_2 molecule on the FeN_4 fragment on the other side of the G plane with E_{act} = 0.55 eV and the formation of the O=Fe=O center. The benzene molecule is adsorbed on the oxygen atoms of the O=Fe=O fragment, and the C–O bond with E_{act} is formed = 0.59 eV. For comparison, direct adsorption of benzene on the oxygen atom of the Fe=O group is energetically unfavorable and requires an additional free energy of 0.86 eV. Benzene adsorbed on the O=Fe=O fragment is converted to phenol through the transfer of one H atom from the adjacent C atom of the benzene molecule to the O atom with E_{act} = 0.35 eV. The Fe=O catalytic center can be regenerated in the reaction cycle after desorption of phenol from the iron atom. The highest energy barrier along the reaction pathway occurs during the adsorption of benzene on the O=Fe=O fragment, which is only 0.59 eV and is moderate for low-temperature reactions. The formation of Fe=O/O=Fe=O intermediates on the FeN_4 fragment is also confirmed by the analysis of the XAFS spectra of FeN_4/GN samples after treatment with H_2O_2.

EXAFS results show that in the initial FeN_4/GN samples, the average value of the coordination number of the Fe atom is about 4, almost the same as that in the FePc molecule, but less than its maximum coordination number of 6. Thus, the iron-containing sites in these catalysts are coordinatively unsaturated. Upon further treatment of the FeN_4/G sample with hydrogen peroxide, the coordination number of the iron-containing site increases. These results confirm the DFT calculations, according to which the coordinatively unsaturated iron-containing center can effectively activate the H_2O_2 molecule to form the Fe=O group. The above experimental results indicate that FeN_4 centers play a crucial role in the adsorption and activation of oxygen, which is consistent with the reaction cycles obtained in the DFT calculations. For comparison, the reaction path of benzene oxidation on the Fe atom of the FePc molecule was

also calculated. It is shown that the reaction mechanism and free energy diagram of benzene oxidation on FePc are similar to those on FeN_4/G, but the dissociation energy of the first H_2O_2 molecule to form Fe=O on FeN_4/G is lower than on the FePc monomer.

Analysis of charges according to Bader shows that the charge on the iron atom of the FeN_4/G fragment is 0.14 at. units higher compared to FePc, as a result of which the transfer of electron density to the adsorbed oxygen atom is 0.10 at. units higher compared to FePc, which energetically favors the formation of the Fe=O bond in the FeN_4/G catalyst. Thus, the increased activity of FeN_4/G in the benzene oxidation reaction can be due to both the internal increase in the activity of the FeN_4 fragment and the high dispersion of these centers in FeN_4/G compared to bulk FePc.

Thus, it was shown in [153] that the unique two-dimensional structure of the considered catalysts provides a well-defined model for understanding the nature of the catalytic oxidation reaction on FeN_4/G type catalysts using experimental data and DFT calculation results. In this system, the FeN_4 fragment is highly dispersed and well stabilized by the graphene matrix, which subsequently increases the activity of the benzene oxidation reaction to phenol. This reaction can proceed efficiently at room temperature and even at 0°C. DFT calculations show that the catalytic activity is due to the presence of isolated iron atoms, and the activation barriers are moderate enough for the reaction to proceed at room temperature, which is consistent with experimental data. The results obtained open the way to the creation of highly efficient catalysts using non-precious metals for catalytic oxidation reactions at low temperatures.

ACETYLENE HYDROCHLORINATION REACTION CATALYZED BY GRAPHENE-FeN_X CATALYSTS (x = 4, 3, 2, 1)

In [163], the mechanism of acetylene hydrochlorination catalyzed by graphene-FeN_x (x = 4, 3, 2, 1) catalysts doped with different amounts of N atoms was investigated using the DFT method. Based on the activation barrier of the elementary stages of the reaction, as well as the activity of these catalysts, the most suitable type of catalyst without noble metals for acetylene hydrochlorination was determined.

All density functional theory calculations were performed using the Gaussian09 software package [164] with the B3LYP exchange-correlation functional [165]. The 6-31G(d,p) basis set was used for hydrogen, carbon, nitrogen, and chlorine atoms, and the LANL2DZ effective basis set with pseudopotential was applied for Fe atoms. All relative energies along the reaction pathway were obtained by accounting for zero-point energy during optimization of the spatial structure, without any symmetry restrictions. Moreover, the DFT-D3 method was used in all calculations to account for the dispersion correction [166]. Harmonic vibrational frequencies were calculated to verify that all optimized structures correspond to energy minima (no imaginary frequencies) or transition states (one imaginary frequency). To confirm that each transition state (TS) correctly links the reaction products with the reactants, calculations along the internal reaction coordinate (IRC) were performed [167, 168]. The energy of individual adsorption of acetylene (C_2H_2) and hydrogen chloride (HCl) molecules, as well as the energy of their joint adsorption on the graphene-FeN_x catalyst, was calculated using the formulas:

$$E_{ads} = E_{adsstate} - (E_{C2H2}/HCl + E_{catalyst}), \quad (15)$$

$$E_{co\text{-}ads} = E_{co\text{-}adsstate} - (E_{C2H2} + E_{HCl} + E_{catalyst}), \quad (16)$$

where $E_{adsstate}$ is the total energy of the adsorption complex C_2H_2 or HCl on the catalyst surface, $E_{co\text{-}adsstate}$ is the sum of the total energies of the molecules of C_2H_2, HCl and the catalyst, E_{C2H2}, E_{HCl} and $E_{catalyst}$ are the energies of isolated molecules of C_2H_2, HCl and the catalyst, respectively.

The reactants used were graphene-FeN_4, graphene-FeN_3, graphene-FeN_2, and graphene-FeN_1 catalysts, as well as free C_2H_2 and HCl molecules. Their equilibrium configurations are

shown in Fig. 11. The equilibrium configurations of the graphene-FeN_x catalysts have a planar structure. Graphene-FeN_4, graphene-FeN_3, and graphene-FeN_1 have only one isomer each, while the graphene-FeN_2 catalyst exists in the form of three isomers, depending on the relative positions of the nitrogen atoms [169, 170]. (The subscript for the nitrogen atom is N_1, extra for the availability of the inventory of the graphene-FeN_x catalyst at other values of x). In graphene-FeN_2-Pen, two adjacent N atoms are located within one five-membered ring in the graphene-FeN_2-Oppo isomer, each of the N atoms is included in six-membered rings in the graphene-FeN_2-Hex isomer, and two adjacent N atoms are located in one six-membered ring. The calculated average values of the Fe-N and Fe-C bond lengths in the graphene-FeN_x catalysts are given in Table 4.

To further elucidate the characteristics of graphene-FeN_x catalysts, density of states (DOS) diagrams were constructed for six catalysts [171]. In graphene-FeN_4, the *p* orbitals of C and N atoms make major and minor contributions to the HOMO (highest occupied molecular orbital), respectively. The *d*- and *s*-orbitals of Fe atoms make major and minor contributions to the LUMO (lowest unoccupied molecular orbital), respectively. In graphene-FeN_3, the *p* orbitals of C atoms are the major contributors to HOMO and LUMO. In graphene-FeN_2 LUMO, the orbitals of the three catalysts are similar, namely, the *p* orbitals of C atoms make a significant contribution to LUMO. In graphene-FeN_2-Pen and graphene-FeN_2-Oppo, the *d*-orbitals of the Fe atom and the p orbitals of the C atoms determine the major and minor contributions to HOMO. In graphene-FeN_2-Hex, the contributions of the *d*-orbitals of the Fe atom and the p orbitals of the C atom to HOMO are almost the same. In graphene-FeN_1, the *p* orbital of *C* atoms makes a significant contribution to HOMO; the d orbitals of the Fe atom and the p orbitals of the C atom are the major and minor contributors to LUMO. The difference in the number of embedded N atoms has a significant impact on the HOMO and LUMO structure of graphene-FeN_x catalysts.

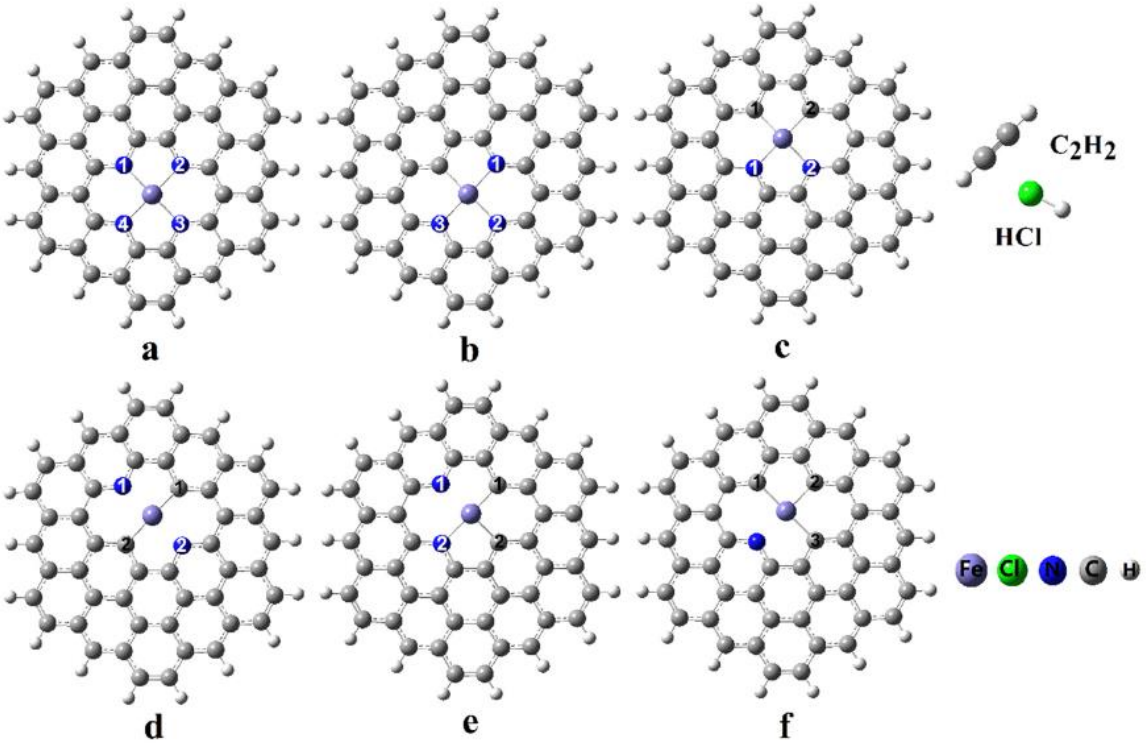

Fig. 11. Optimized structures of C_2H_2, HCl, graphene-FeN_4 (*a*), graphene-FeN_3 (*b*), graphene-FeN_2-Pen (*c*), graphene-FeN_2-Oppo (*d*), graphene-FeN_2-Hex (*e*), and graphene-FeN_1 (*f*) [163]

The adsorption of reactants is a critical step in the reaction (see Fig. 12). Since all catalysts contained only one metal atom, it was previously assumed that only the Fe atom in the catalyst would be the active site of the reaction. Charge distribution calculations showed that in

graphene-FeN_4, the positive charge on the Fe atom is huge. In other catalysts, Fe atoms influence the negative charge distribution. Secondly, it is evident from the LUMO structure that the negative charge is predominantly concentrated around the Fe atoms in graphene-FeN_x catalysts. Therefore, the Fe atom is most likely the active site. To clarify the active sites of the reaction and the order of adsorption by reactants, C_2H_2 and HCl molecules were placed above the Fe atom and C and N atoms around the Fe atom when constructing adsorption complexes. The structure of adsorbed C_2H_2 complexes on graphene-FeN4, graphene-FeN_3, and graphene-FeN_2 catalysts is such that the C_2H_2 molecule, located on the Fe atom, is in different degrees of deformation. In the case of graphene-FeN_1, the C_2H_2 molecule was adsorbed not on the Fe metal atom, but on two carbon atoms linked to the Fe atom. This indicates that a decrease in the number of N atoms embedded in the graphene network changes the active center of the reaction. The adsorption energies of individual reactants and the corresponding energies of joint adsorption are given in Table 5, from which it is evident that the adsorption energy of C_2H_2 on the graphene-FeN_x catalyst is higher than that of HCl, illustrating that the C_2H_2 molecule is adsorbed first, and HCl is adsorbed later, forming a coadsorption structure. Moreover, the adsorption energy of isolated C_2H_2 and HCl molecules is less than the corresponding energy of joint adsorption, which guarantees the possibility of the reaction.

Table 4. Average Fe-N and Fe-C bond lengths in graphene-FeN_x catalysts (x=4, 3, 2, 1) and the activation energies of the stages determining the rate of the acetylene hydrochlorination reaction

Catalyst	d(Fe–N), Å	d(Fe–C), Å	Activation energy rate-limiting stage (kcal/mol)
Graphene-FeN_4	1.92		16.80
Graphene-FeN_3	1.93	1.88	20.59
Graphene-FeN_2-Pen	1.92	1.89	23.64
Graphene-FeN_2-Oppo	1.98	1.90	27.71
Graphene-FeN_2-Hex	1.97	1.88	28.52
Graphene-FeN_1	1.99	1.91	38.21

Table 5. Energies of critical points (kcal/mol) along the cross-section of the multidimensional potential energy surface of the reaction of conversion of acetylene and hydrogen chloride to vinyl chloride using iron- and nitrogen-containing catalysts

Catalyst	Coadsorbtion	TS1	IM1	TS2	IM2	TS3	IM3
FeN_4	-32.31	-18.79	-29.71	-19.60	-32.31	-22.28	-49.50
FeN_3	-11.59	9.00	-14.35	-2.78	-31.61	–	–
FeN_2-Pen	-36.34	-24.74	-56.50	-34.88	-56.34	–	–
FeN_2-Oppo	-35.49	-21.12	-45.60	-17.89	-57.36	–	–
FeN_2-Hex	-34.18	-18.93	-42.72	-19.20	-56.89	–	–
FeN_1	-65.58	-27.91	-60.57	-22.36	-43.16	–	–

To better understand the bond types in the adsorption complexes, the Mayer bond orders of C=C in C_2H_2 and H–Cl bond orders of HCl in the coadsorption structures were calculated, and their bond types were estimated. When the Mayer bond order is close to 1.0, 2.0, and 3.0, the bond types are identified as single, double, and triple bonds, respectively. For the graphene-FeN_4 catalyst, two H atoms of the adsorbed C_2H_2 molecule are displaced from the iron atom, causing the deformation of the C_2H_2 molecule. The length of the C=C double bond of the C_2H_2 molecule increased from 1.206 to 1.233 Å, and the length of the H–Cl bond of the HCl molecule also increased from 1.286 to 1.293 Å. This indicates the degree of interaction between the reactants and the catalyst. To further study this interaction, the electron density transfer between the catalyst and reactants in the coadsorption complexes was estimated. Thus, the electron density transfer between the C_2H_2 and HCl molecules on the graphene-FeN_4 catalyst was 0.054 and 0.148 a.u., respectively. In the adsorption complex with the graphene-FeN_3 catalyst, the C=C bond length of the C_2H_2 molecule increased to 1.253 Å, and the H–Cl bond length of the HCl

molecule increased to 1.297 Å with an electron density transfer from the C_2H_2 molecule of 0.018 and the HCl molecule of 0.063 a.u. to the graphene-FeN_3 catalyst. For the graphene-FeN_2 catalysts, the configuration of the C_2H_2 molecule in the adsorption complex on graphene-FeN_2-Pen was similar to that on graphene-FeN_4. The bond length of the C_2H_2 molecule increased to 1.238, 1.282, and 1.279 Å in graphene-FeN_2-Pen, graphene-FeN_2-Oppo, and graphene-FeN_2-Hex, respectively, and the electron density transfer between them was 0.150, 0.080, and 0.043 a.u., respectively. In addition, the H–Cl bond lengths in these three coadsorption complexes increased to 1.318 Å, 1.308 Å, and 1.292 Å in turn, and the amount of electron density transferred between them was 0.104, 0.034, and 0.106 a.u., respectively. For graphene-FeN_1, the C=C bond multiplicity in the C_2H_2 molecule is between single and double, and the C_2H_2 molecule itself is bonded to two C atoms of the catalyst with a C=C bond length of 1.397 Å. The electron density transfer between C_2H_2 and graphene-FeN_1 was 0.035 a.u. The H–Cl bond length in the HCl molecule increased to 1.303 Å, with an electron density transfer of 0.074 a.u. between HCl and graphene-FeN_1. The analysis performed showed that during adsorption, an interaction occurs between the reactants and the catalyst, and that the reactants are in different degrees of activation.

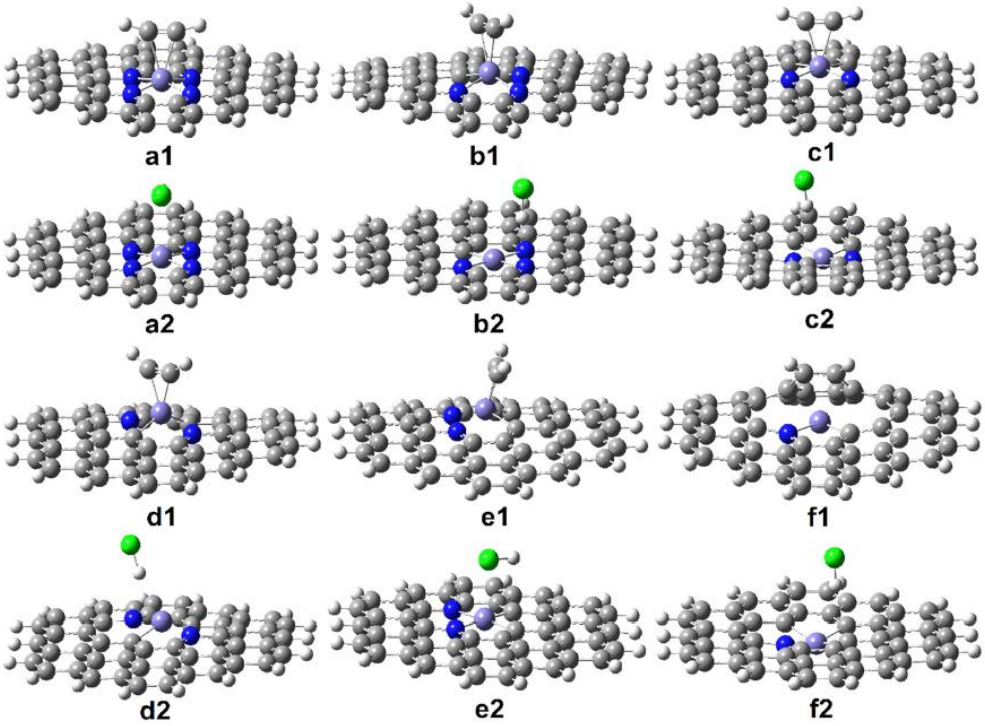

Fig. 12. Stable adsorption configurations of graphene-$FeN_4 \cdot C_2H_2$ (*a*1), graphene-$FeN_4 \cdot$ HCl (*a*2), graphene-$FeN_3 \cdot C_2H_2$ (*b*1), graphene-$FeN_3 \cdot$ HCl (*b*2), graphene-FeN_2-Pen $\cdot C_2H_2$ (c1), graphene-FeN_2-Pen $\cdot$ HCl (*c*2), graphene-FeN_2-Oppo $\cdot C_2H_2$ (*d*1), graphene-FeN_2-Oppo $\cdot$ HCl (*d*2), graphene-FeN_2-Hex $\cdot C_2H_2$(*e*1), graphene-FeN_2-Hex $\cdot$ HCl (e2), graphene-$FeN_1 \cdot C_2H_2$(f1), and graphene-$FeN_1 \cdot$ HCl (*f*2) [163]

The reaction of acetylene hydrochlorination, involving any of the six studied catalysts, begins with the formation of coadsorption structures, the energies of formation of which are listed in Table 5. For the graphene-FeN_4 catalyst, three transition states are localized on the route from the coadsorption structure to the final product (see Fig. 13). For the remaining catalysts, there are two such states. In the hydrochlorination of acetylene catalyzed by graphene-FeN_4, desorption of the product was the rate-controlling step of the entire reaction, with the desorption energy of a vinyl chloride molecule of 16.80 kcal/mol.

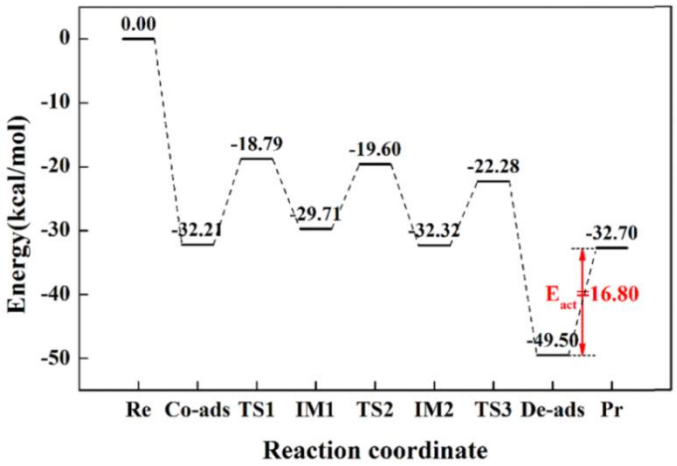

Fig. 13. Energy diagram of the optimal path for graphene-FeN_4 catalyzed acetylene hydrochlorination [163]

For the other studied catalysts, diagrams similar to those shown in Fig. 13 were obtained, and the rate-limiting stages and corresponding activation energies were determined. Thus, when using the graphene-FeN_3 catalyst, the rate of the entire reaction is determined by the stage of transition from TS1 to IM1, with an E_{act} of 20.59 kcal/mol. For the graphene-FeN_2-Pen catalyst, the rate-limiting stage of the entire process was the desorption of the vinyl chloride molecule from the surface, which required an energy of 23.70 kcal/mol. The graphene-FeN_2-Oppo and graphene-FeN_2-Hex catalysts have almost the same effect on the reaction. The rate-determining stage of the entire reaction was the stage of transition from IM1 to TS2, for which E_{act} was 27.21 and 28.52 kcal/mol, respectively. The highest value of E_{act} was obtained for the graphene-FeN_1 catalyst when moving from IM1 to TS2, with E_{act} = 38.21 kcal/mol.

In the catalytic reaction of acetylene hydrochlorination on the considered catalysts, the Fe atom was the active center of the reaction on graphene-FeN_4, graphene-FeN_3, and graphenes-FeN_2. In graphene-FeN_1, the Fe atom and two C atoms adjacent to it were the active centers of the reaction. According to the results, the degressive order of their energy barrier values corresponds to the following dependence: graphene-FeN_1 > graphene-FeN_2 > graphene-FeN_3 > graphene-FeN_4. For graphenes-FeN_2, the following dependence of activities was obtained: graphene-FeN_2-Hex > graphene-FeN_2-Oppo > graphene-FeN_2-Pen. The lowest activation barrier among the catalytic reactions in the graphene-FeN_x catalyst series was obtained for graphene-FeN_4 and it amounted to only 16.80 kcal/mol. Graphene-FeN_4 was expected to be the most efficient noble metal-free catalyst for acetylene hydrochlorination.

Moreover, the free energy change of the graphene-FeN_x (x = 4, 3, 2, 1)-catalyzed acetylene hydrochlorination reaction at 453.15 K was calculated. The results show that at 453.15 K, the catalyst with the lowest energy barrier is still graphene-FeN_4, and the reaction energy barrier for it is only 16.01 kcal/mol. The trend of free energy barrier change at 453.15 K of the graphene-FeN_x(x = 4, 3, 2, 1)-catalyzed reaction is consistent with the calculated zero-point energy at 298.15 K.

A large number of spin states characterizes the Fe atom. In graphene-FeN_x (x = 4, 3, 2, 1) catalysts, the number of electrons in graphene-FeN_4 and graphene-FeN_2 is even, and the spin multiplicity of the Fe atom was assumed to be 1, 3, and 5. In contrast, the number of electrons in graphene-FeN_3 and graphene-FeN_1 is odd, and the spin multiplicity of the Fe atom was 2, 4, and 6. In the work [163]. The cases were considered when the Fe atom in graphene-FeN_4 and graphene-FeN_2 is in the singlet state, and graphene-FeN_3 and graphene-FeN_1 in the doublet state. The reaction conditions for other multiplets of the Fe atom in graphene-FeN_x (x = 4, 3, 2, 1) were analyzed. It turned out that the molecules C_2H_2 and HCl are not adsorbed in the triplet and quintet states of graphene-FeN_4. They are also not adsorbed in the quartet and sextet states of

graphene-FeN_3. In the triplet states of graphene-FeN_2-Pen and graphene-FeN_2-Oppo, the adsorption energy of C_2H_2 and HCl molecules is very low, and the coadsorption energy is -3.11 and -4.06 kcal/mol, respectively, which is lower than the adsorption energy of the HCl molecule (-5.04; -4.47 kcal/mol, respectively), so the coadsorption structure is not formed. In the quintet states of the catalyst, the C_2H_2 molecule is not adsorbed. In the triplet state of graphene-FeN_2-Hex, the adsorption of C_2H_2 and HCl is weak, and the energy of their coadsorption is very low, which corresponds to physical adsorption, so a suitable transition state cannot be found. In the quartet state of graphene-FeN_1, the adsorption energy of C_2H_2 is higher, and the coadsorption energy is also higher. Thus, the Fe atom in the catalysts considered in this work is in optimal spin states.

Received in [163] The results obtained by the DFT method showed that the activity of graphene-FeN_x (x = 4, 3, 2, 1) consistently increased with the increase in the degree of doping with nitrogen atoms. The following order of E act was obtained for the catalytic reaction of the graphene-FeN_x series of catalysts: graphene-FeN_1 > graphene-FeN_2 > graphene-FeN_3 > graphene-FeN_4. There are three configurations of graphene-FeN_2 catalysts based on the relative position of N atoms. For them, the order of energy barriers was as follows: graphene-FeN_2-Hex > graphene-FeN_2-Oppo > graphene-FeN_2-Pen. Graphene-FeN_4 demonstrated the highest activity in the production of vinyl chloride catalyzed by catalysts made of base metals. The results of the study will help develop the theory of the structure of catalysts that do not contain noble metals.

EFFECT OF EXTERNAL ELECTRIC FIELD ON THE ACTIVATION OF THE C–H BOND IN A METHANE MOLECULE ADSORBED ON IRON-CONTAINING GRAPHENE

An innovative approach to increasing the activity of an iron-containing G catalyst in the conversion of methane to more valuable products is proposed in [172]. This reaction allows the primary component of natural gas, CH_4, to be converted into products such as methanol, formaldehyde, light olefins, and ethylene, which are of interest to the petrochemical industry [173–176]. The cleavage of the C–H bond in the methane molecule is considered the most critical stage of its further transformation, mainly due to the high dissociation energy, which is about ~100 kcal/mol [177]. To carry out this stage, at one time, several metal-containing catalysts were used, such as ionic [178, 182] complexes, specially prepared surfaces [180], clusters [181, 182], cluster ions [183–185], oxides [186, 187], as well as the metals themselves, embedded in porous materials [188–191]. To date, the most promising catalyst is considered to be clusters deposited on substrates, in particular on G. Several works have considered modifications of defect-containing G doped with metals, which have found application not only in catalysis, but in a wide range of applications, such as materials for storing gases, sensitization [192–202]. Such a diverse range of applications is explained by the combination of the electronic properties of the metal with a large surface area. Graphene sheets with deposited gold [202] or copper [198] clusters were used to activate the oxidation reaction of CO with oxygen. The graphene substrate allows for lower activation barriers compared to metals without a substrate [200, 201, 203].

Excellent adsorption properties of iron-containing G (FeG) concerning some small molecules, such as formaldehyde [204], hydrogen sulfide [205], and carbon monoxide [206], make it a promising material for use in gas adsorption and for the creation of gas sensors [207]. Iron-containing Graphenes are also used as catalysts for various reactions, such as N_2O decomposition, CO oxidation [208], and oxygen reduction. Its advantages include the low cost of the catalyst and the absence of toxicity compared to noble metals. Iron-containing G is easily synthesized by treating graphene with structural defects with iron-containing solutions (e.g., $FeCl_3$) [204 , 209].

The imposed external electric field (EF) is well known as one of the effective approaches to modify the properties of low-dimensional systems [210–214], especially carbon materials such as carbon nanotubes [215, 216] and graphene sheets [216–220]. It was demonstrated in [212, 213] that the application of EF of appropriate direction and strength can control the chemoselectivity of propene oxidation catalysed by iron oxo porphyrin materials. It was also shown there that EF applied along the direction of electron flow from the substrate to the iron oxo center can reduce the activation barrier and change the reactivity and selectivity of the catalysts. In addition, it was found that the application of EF is an effective method to modify the adsorption and catalytic properties of ideal and modified G. The adsorption/desorption and activation of H_2 and O_2 molecules on metal-doped graphene were controlled by appropriate EF [216, 220]. EF stacking has also been proposed as an efficient method for the binding and decomposition of nitrous oxide (N_2O) on Al-, Ga-, and Mn-doped G [218, 222].

In [172], a theoretical study of the effect of EF on the adsorption of the methane molecule and the activation of its C–H bond on Fe-doped G is carried out using density functional theory. The relative energies and structures of intermediate and transition states are discussed to understand the effect of EF on the adsorption and activation of the C–H bond.

The calculations were performed using a finite cluster model of an infinite graphene lattice in the form of a regular hexagon with zigzag edges, which consisted of 112 carbon atoms. The dangling bonds of the boundary carbon atoms were saturated with hydrogen atoms with a C–H bond length of 1.14 Å. A single vacancy in graphene was created by removing one carbon atom in the center of the model. The iron atom was located in the center of the single vacancy of the defect-containing G model. All calculations were performed using the Gaussian 09 program [164] with the M06-L functional [223, 224]. During geometry optimization, the 6-31G(d, p) basis set was used for all atoms except the Fe atom, which was described by the effective Stuttgart-Dresden (SDD) nuclear potential [225]. In the optimization of the structure of the adsorption complexes, the positions of the CH_4 molecule atoms and most of the graphene cluster model were assumed to be independent. In contrast, the peripheral hydrogen atoms in the G model were kept motionless to preserve the graphene topology. To confirm that the obtained structures correspond to transition states, the Hessian was diagonalized at the same level of theory. To determine the charges on the atoms of the adsorption complex, the canonical orbitals were transformed into natural orbitals (NBO) [226]. To describe the $_{CH4}$ molecule in a strong electric field and to obtain more accurate interaction energies with the field, single-point calculations were performed using a more flexible 6-31++G(d, p) basis set for all atoms. Moreover, in these single-point calculations, the D3 version of the Grimme correction was also applied to account for van der Waals interactions [166]. The contribution of the zero-point energy (ZPE) was not accounted for. The external EF was applied in the direction perpendicular to the graphene sheet in the range from -0.015 to +0.015 au with an interval of 0.005 au. Note that the EF strength of 1 a.u. is created at the first Bohr orbital of the hydrogen atom, which is equal to $\approx 5.14 \times 10^{11}$ Vm^{-1} [227]. The EF range from -0.015 to +0.015 au corresponds to from -7.17×10^9 to $+7.17 \times 10^9$ Vm^1. The positive direction of EF is defined as the direction from the graphene plane to the Fe atom and the adsorbed molecule, and the negative one is in the opposite direction.

The calculations assumed that the ground electronic state of the iron-containing complex, FeG, is a singlet. The electronic structure of the Fe atom was $[Ar]3d^64s^2$. The binding energy of the iron atom on the single vacancy of the graphene sheet was -136.2 kcal/mol. The embedded Fe atom and nearby carbon atoms protruded from the plane of the graphene sheet. The distance between the Fe atom and the three nearest carbon atoms was 1.77 Å, which is comparable with the data of previous studies using the PBE functional [114, 205, 208]. The partial charge of the Fe atom at EF = 0 was +0.329 at. units of charge, indicating the transfer of electron density from the Fe atom to the graphene sheet. The frontal molecular orbitals (FMO) of the FeG system, both

HOMO and LUMO, are mainly due to the *d*-orbitals of the Fe atom, indicating the coordination unsaturation of the Fe atom, which determines its acceptor ability with respect to adsorbed molecules. When a perpendicular external electric field EF was applied, electron polarization of the FeG system was observed. For positive EF, the positive charge on the Fe atom decreased, and the degree of involvement of the *d*-orbital of the iron atom in LUMO decreased compared to the absence of EF. On the contrary, the external negative EF led to an increase in the positive charge on the Fe atom. Such a charge redistribution gave reason to believe that such a transfer of electron density will promote the adsorption of the methane molecule. LUMO character tended to increase the contribution of *d*-orbitals with increasing EF strength. It was expected that the Fe atom, being in the FeGP system, would interact better with the methane molecule when negative EF was imposed.

Fig. 14 shows the equilibrium structures of the adsorption complexes of the methane molecule on the Fe atom of the FeG system with and without the effect of EF. In its absence, the methane molecule binds to the Fe atom of the FeG sheet via an η^2 interaction. The interatomic Fe H distances in the complex were 1.99 and 2.08 Å (see Fig. 14). The carbon atom of the methane molecule also made a specific contribution to the binding, with the optimal interatomic Fe C distance equal to 2.37 Å. The calculated adsorption energy of methane was -12.9, which is comparable with the value of -11.6 kcal/mol obtained within the framework of superimposing periodic conditions with the PBE functional [2-29]. The C–H bonds of the methane molecule were slightly lengthened from 1.09 to 1.10 and 1.11 Å upon Fe GP interaction. Analysis of the charge distribution in the adsorption complex showed the presence of interaction between the *d*-orbitals of the Fe atom and the *s* orbital of the H atom. The charge on the methane molecule was +0.152 au, while the charge on the Fe atom decreased from +0.329 to +0.101 au. Upon imposition of positive EF, the methane molecule moved away from the active center of Fe; therefore, the Fe H1 and Fe C distances increased. The decrease in the positive charge on the methane molecule in the adsorption complex compared to the absence of EF was in the range from 0.020 to 0.071 au. The adsorption energies of the methane molecule on FeGP decreased to -11.2, -10.0, and -10.3 kcal/mol for EF +0.005, +0.010, and +0.015 a.u., respectively. At negative EF, the opposite effect was observed, i.e., the methane molecule moved toward the Fe atom.

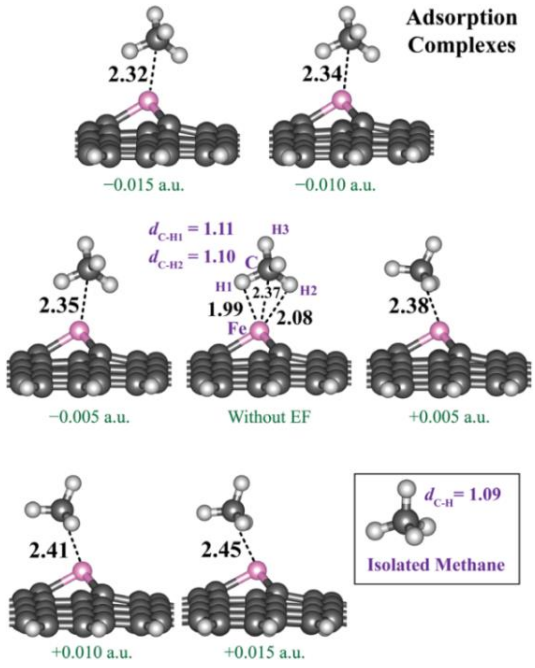

Fig. 14. Optimized structures of adsorption complexes of methane over FeGP with the effect of applied EF. [Color figure can be viewed at wileyonlinelibrary.com] [172]

These results indicate that the superposition of EF can significantly change the adsorption energy depending on the direction and strength of EF. Thus, the adsorption and desorption states of methane on the FeG adsorbent can be controlled explicitly by superposition of EF and

changing its strength.Activation of the adsorbed methane molecule on FeG results in the cleavage of the C–H bond to form a CH_3 group and an H atom bound by the graphene substrate. This process is considered to be a key one in the conversion of methane into various products [230]. Without external EF, the Fe C distance in the transition state decreased from 2.37 to 1.97 Å (see Fig. 15). At the same time, the hydrogen atom H1 of the methane molecule moves toward the surface of G, which results in the elongation of the C–H1 bond from 1.11 to 1.80 Å and the decrease in the Fe–H1 distance from 1.99 to 1.48 Å. The corresponding activation energy was 25.7 kcal/mol, and the apparent activation energy, ΔE_{ts} (the relative energy of the transition state concerning the sum of the energies of the isolated methane molecule and the G sheet model), was 12.8 kcal/mol. This activation energy is comparable with the result of previous calculations using the PBE functional, which gave a value of 20.2 kcal/mol [239]. The structure of the transition state was confirmed by a single imaginary frequency of 770.13i cm^{-1}, the mode of which corresponded to the cleavage of the C–H1 bond of methane and the transfer of the H1 atom to the carbon atom G.

After the C–H bond is broken, the CH_3 group binds to the active Fe center, and the H atom is coordinated to the nearest carbon atom of the graphene sheet, forming a complex of reaction products. The Fe–C and C–H1 distances were 1.94 and 1.20 Å, respectively (see Fig. 16). The energy of formation of the final product is 5.7 kcal/mol relative to the sum of the energies of the isolated reactants.

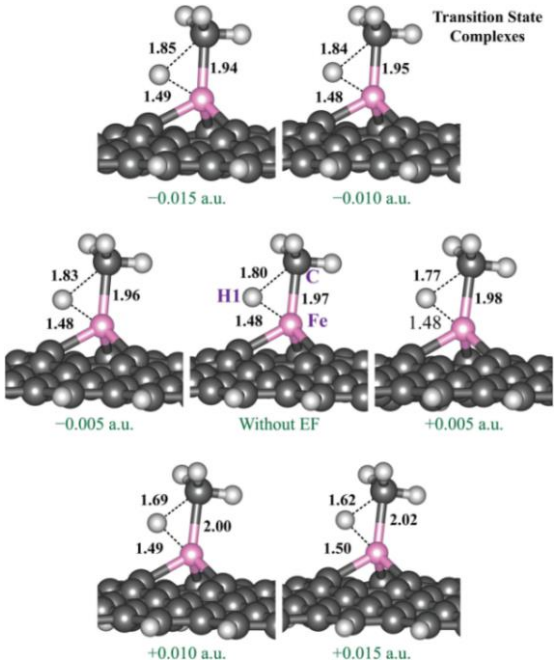

Fig. 15. Optimized structure of transition state complexes of methane activation over FeGP with the effect of applied EF. [Color figure can be viewed at wileyonlinelibrary.com] [172]

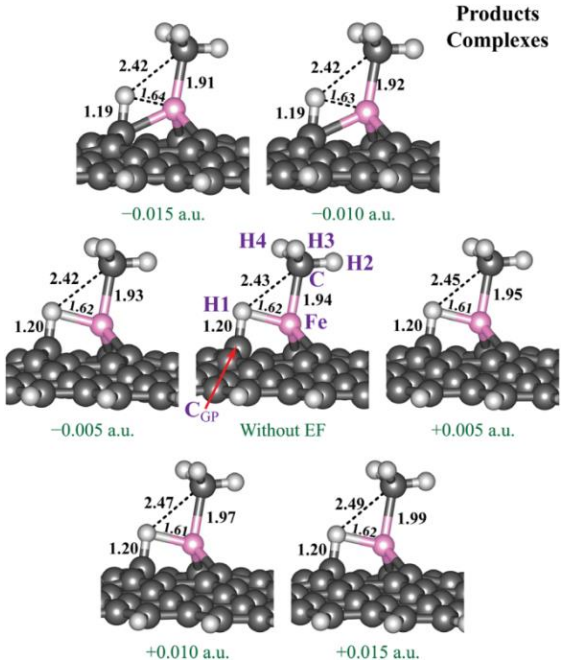

Fig. 16. Optimized structure of product complexes of methane activation over FeGP with the effect of applied EF. [Color figure can be viewed at wileyonlinelibrary.com] [172]

When a positive EF is imposed, the C–H distance between the atoms of the broken C–H bond decreases compared to that without EF. The H CGP distance tends to increase slightly with a more positive EF. This results in a decrease in the apparent activation energy from 22.3 (14.1), 18.9 (9.1), and 17.5 (5.6) kcal/mol when EF strengths of +0.005, +0.010, and +0.015 au are imposed, respectively. The Fe–C distance in the reaction product complexes tended to increase from 1.95 to 1.99 Å when a positive EF was imposed, while the CG–H distance remained virtually unchanged.

At negative EF, the opposite phenomena were observed. The change in the C–H distance in the transition states tended to increase. For the reaction product complexes, the CH_3 group gradually approached the Fe atom with increasing field strength. The Fe–C distances decreased slightly, while the activation energies increased significantly. The relative energies of the product complexes increased under the action of the applied negative electric field.

Fig. 17 shows the activation energy profiles of a methane molecule on a FeGP sheet with and without the applied external EF. Without EF, the apparent activation energy, ΔE_{ts}, was 12.8 kcal/mol, and the activation energy of C–H bond cleavage on the Fe atom in FeGP was 25.7 kcal/mol. The activation energies tended to increase with the imposition of EF in the negative direction, while the apparent activation energies, ΔE_{ts}, did not change significantly. On the other hand, with the imposition of positive EF, the apparent activation energy and E_{act} decreased within 1.7–5.6 and 3.4–8.2 kcal/mol, respectively. The positive direction of EF resulted in the C–H bond change being earlier in the transition state. This result is consistent with the data of previous theoretical studies of the C–H bond dissociation of methane on zeolites containing Au atoms, carried out at the M06-L/6-31G** level of theory [208]. The complexation without EF between the coordinated CH_3 group and the H atom on the Fe atom is endothermic with an energy of 5.7 kcal/mol. When the negative EF is imposed, this energy increases, while when the positive EF is imposed, it decreases. Therefore, EF can hinder or promote the C–H bond dissociation of the methane molecule on the FeG sheet depending on the direction of EF. Moreover, the C–H bond activation reaction on FeG is kinetically and thermodynamically allowed when the positive EF is imposed.

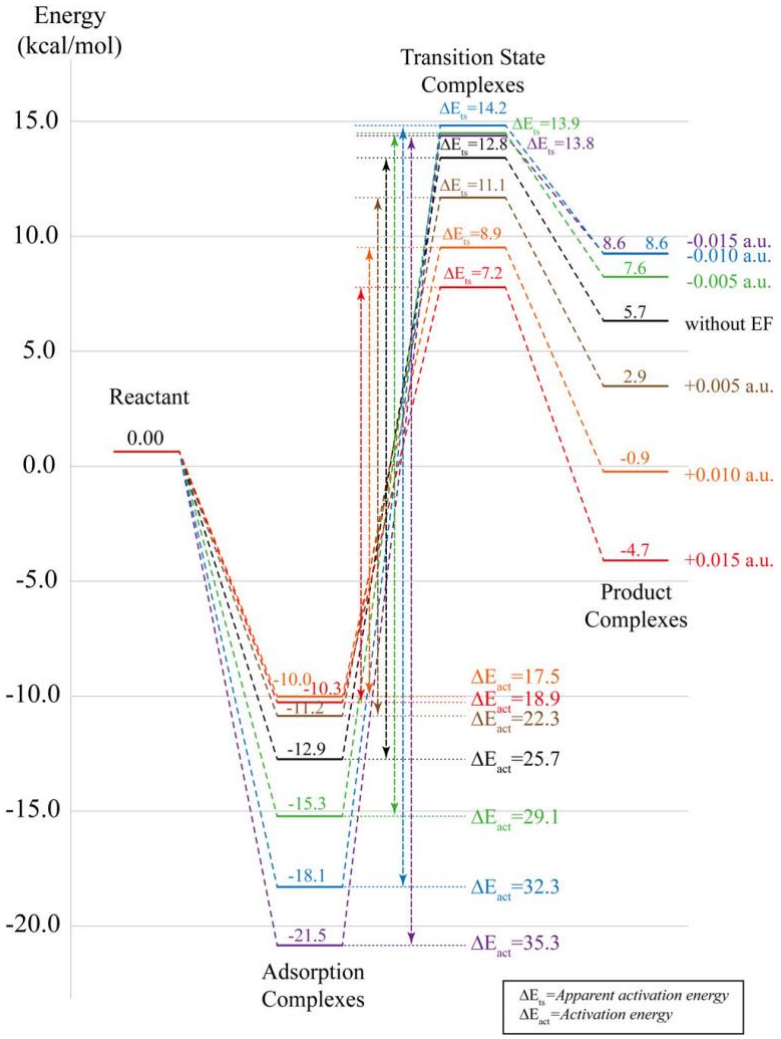

Fig. 17. Reaction energy profiles for methane activation over FeGP include the effect of applied EF. Energies are in kcal/mol. [Color figure can be viewed at wileyonlinelibrary.com [172]

Thus, without an external electric field, the Fe atom with a positive partial charge embedded in G had catalytic activity in the methane activation reaction with an activation energy of 25.7 kcal/mol [172]. The stability of the adsorption complexes, transition states, and products changes significantly under the action of the direction and strength of the applied electric field. Positive EF destabilizes the adsorption complexes, while the transition state and products are more stable compared to the case without a field. The activation energy significantly decreased from 25.7 to 17.5 kcal/mol upon applying an electric field of +0.015 a.u. The results indicate that an applied external electric field can regulate the catalytic activity of G upon iron addition.

CATALYTIC GROWTH OF ZIGZAG EDGES OF GRAPHENE SHEETS INDUCED BY A SINGLE IRON ATOM

As has been noted many times, defects in G, including vacancies [231], dislocations [232], grain boundaries [233], and edges [234], are of interest because they offer many ways to modify the properties of the ideal G structure deliberately. Of great interest are also dopant atoms in graphene (e.g., the transition metal atoms discussed above, which substitute for carbon atoms in graphene sheets and have been theoretically shown to have unusual magnetic or catalytic properties) [235]. Single atoms or small clusters in G (e.g., N [236] and Fe [148, 237, 238]) have been directly observed using high-resolution transmission electron microscopy (TEM). Doping elements such as Si have also been directly observed by scanning TEM [243]. In these cases, the atoms were embedded in the graphene network. In addition, single Au [240, 241] and Al [241] atoms have been observed (by TEM or scanning TEM) at the edges of the graphene sheet. The interaction between single metal atoms and the graphene edges is complex due to the different types of trap states at the edges [240]. Furthermore, some theoretical studies suggest that the atomic configurations of G faces are strongly influenced by nearby transition metal atoms [242, 243].

In [244], an experimental and theoretical study of the features of the location of individual Fe atoms at the edges of graphene sheets was carried out. Catalysts with a single metal atom embedded in the graphene network, as described above, are considered as a means of maximizing the catalytic efficiency [245, 246] due to the valence unsaturation of such atoms. Atoms at the edges of graphene sheets are of great interest given their catalytic potential, in particular, for understanding the catalytic growth of sp^2-hybridized carbons, primarily G, under the action of transition metals. Using low-voltage aberration-corrected TEM (LVACTEM) [247], it is possible to determine the structure of a group of atoms consisting of carbon atoms and a single Fe atom at the edge of a graphene sheet and, in addition, to record the dynamics of the movement of this Fe atom. Pentagon-hexagon transitions are observed, which indicate processes of catalytic addition or removal of carbon atoms at the edges of the graphene sheet. These processes are in excellent agreement with the results of ab initio calculations and molecular dynamics (MD) modeling, which, in turn, are also consistent with a previously proposed model of the catalytic growth of carbon nanotubes [248].

Previous studies have shown that the two-dimensional nature of the motion of individual atoms above the basal plane in G exhibits Brownian motion. From this information, the two-dimensional diffusion coefficient can be extracted, as well as the average activation energy for diffusion according to Arrhenius [147, 249].

A Gaussian distribution describes the spatial probability of finding a particle subject to Brownian motion. In this case, the mean square displacement (MSD) $\left\langle R^2(t)\right\rangle$ depends linearly on time, and the gradient corresponds to the diffusion coefficient (D) and is written as $\left\langle R^2(t)\right\rangle = 2nDt$ (Where n-dimension) [250, 251]. Similar to previous observations of an Au atom at the edges of a graphene sheet [240], refined experimental data [244] show that the diffusion of a single Fe atom along the edge of a single-layer graphene sheet is directly related to

the atomic configuration of the sheet edge. Moreover, random one-dimensional diffusion of the Fe atom along the G edge does not follow Brownian motion, but exhibits anomalous diffusion (namely, sub- or superdiffusion). The presence of trapped configurations explains the phenomenon of subdiffusion. In the absence of such trapped configurations, superdiffusion (levitation) occurs.

In the CVD-grown G samples used in [244], holes are occasionally found that can be enlarged by irradiation with the electron beam of a low-voltage aberration-corrected transmission electron microscope at an accelerating voltage of 80 kV. These freshly formed in situ edges of the enlarged holes represent an adequate (previous electron energy loss spectrum and TEM studies have confirmed the absence of oxygen or nitrogen at these edges [252] as well as hydrogen [253]) and convenient model for studying the one-dimensional motion of adsorbed Fe atoms. Because of the higher binding energy of the Fe atom at the exposed edges of G compared to the binding to the basal plane, Fe atoms are usually located at the edges.

Fig. 18 shows the two most common configurations of a chair-armrest graphene edge with one Fe atom. The presence of two different configurations of such an edge involving an iron atom is established. Quantitative comparisons between the experimental and simulated images show that in the first case, the Fe atom is embedded in a five-atom ring, forming a pentagon (Fig. 18*c*). In the second case (Fig. 18*d*), the Fe atom, when embedded in a five-atom ring, forms a distorted hexagon (i.e., the Fe atom replaces a carbon atom in a hexagonal lattice). The structures of the corresponding structures calculated by the DFT method are shown in Fig. 17*c* and *f* (top and side views, respectively).

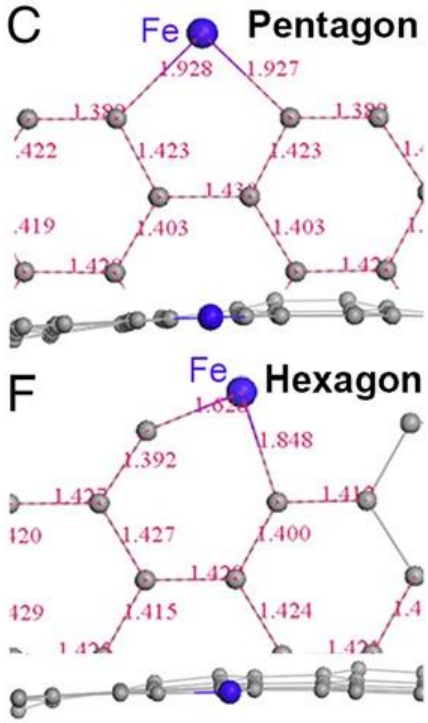

Fig. 18. Identification of hexagon and pentagon structures. (A–C) High-resolution TEM (HRTEM) images (false color), magnified regions of HRTEM with overlaps of the DFT-calculated atomic structures, and DFT-derived structures (top and side views) of a pentagon including an Fe atom. G_{ray} ball, carbon atom; orange ball, Fe atom. (D–F) HRTEM images (false color), magnified regions of HRTEM with overlaps of the DFT-calculated atomic structures, and DFT-derived structures (top and side views) of a distorted hexagon including an Fe atom. (Scale bars: B and E, 0.5 nm.) [244]

The pentagon and hexagon structures are of particular interest because of their importance for the catalytic growth of sp^2 carbon materials [248]. The action of an electron beam on adsorbed Fe atoms located at the edges of a graphene sheet results in the displacement of the Fe atom to different locations on the edge, which facilitates its movement along the edge of the graphene sheet. Figure 19*a–d* shows a typical movement of an Fe atom by one unit cell. The Fe atom moves from a pentagon (Fig. 19*a*) into a hexagon with its participation (Fig. 19*b*) and moves to the right. Then the monatomic motion creates the dark shadow line shown in Fig. 19*c*, which is highlighted by the red circle (i.e., the Fe atom moves during the camera exposure). It then stops at the adjacent position and forms a pentagon again (Fig. 19*d*).

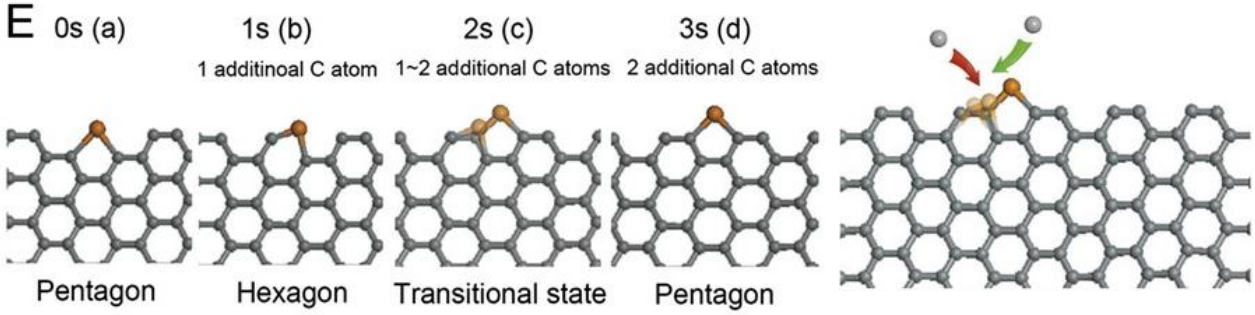

Fig 19. One cycle of catalytic growth of the graphene edge. (*a–d*) A series of high-resolution TEM images for 4s; the Fe atom is highlighted as a red dot, whereas the nearby carbon atoms are highlighted as black dots. The dark shadow line, which is highlighted by the red circle in C, is due to the motion of the Fe atom during exposure time. (Scale bar: 0.5 nm.) (*e*) The corresponding atomic structures for *a–d*. (*f*) The combination of *a–d*, which shows the trace of the Fe atom during the one-unit cell translocation. (Scale bar: 0.5 nm.) (G) The atomic structure for the whole growth process (two carbon atoms are added) [244]

In most cases, translocation of Fe atoms without the removal or addition of carbon is not observed. The incorporation of carbon atoms into the graphene edge via an Fe atom highlights the catalytic properties of Fe at the atomic level. In this process, free carbon atoms in the vicinity diffuse under the action of an electron beam [237, 254]. Electrons accelerated to 80 kV can transfer up to 16 eV to a carbon atom and 3 eV to a single Fe atom [255]. At room temperature, the thermal activation energy for changing the configuration of graphene edges (insertion or removal of a carbon atom) is insufficient. In contrast, removal or translocation of carbon atoms under the action of an electron beam can occur [234, 240]. In [244], it was shown that Fe atoms at graphene edges are capable of both removing and incorporating carbon atoms, acting as a catalyst determining the transition between pentagons and hexagons.Compared to the armrest-type edges, Fe atoms on zigzag edges were sometimes able to overcome or jump large distances in 1. It was found that the local displacement of an Fe atom along one edge of a graphene sheet exhibits a one-dimensional random motion consisting of random jumps and stays in a fixed position. Displacements that are equal to or smaller than a single-atom distance (C–C distance) correspond to hexagon-pentagon transitions.

These transitions are usually fast, e.g., within 28s. Long steady-state periods are observed predominantly in the pentagonal formations at the armchair edges (e.g., 42 to 58 s). Steady-state periods are also observed in the hexagonal formations consisting of five C atoms and an Fe atom, both in the armchair and zigzag edge cases. Large displacements or jumps are observed only along the zigzag edges (e.g., 85s). The DFT calculations yield binding energies of the Fe atom in different configurations at the armchair or zigzag edges, which are in good agreement with the experimental data, since the observed trap state is a configuration with a high binding energy (5.45 eV) compared to the other configurations. However, the stable state of the Fe atoms depends not only on the thermodynamics but also on the kinetics. Additional insight can be gained by estimating the residence time of individual Fe atoms at the armchair or zigzag edges of the graphene sheet using MSD methods, which can be characterized by a power law: $\left\langle R^2(t)\right\rangle = t^{\gamma}$. For dynamic motion along the armchair edge $\gamma = 0.7$ (the linear correlation coefficient is 0.98), whereas for the zigzag edge $\gamma = 1.2$ (the linear correlation coefficient is 0.99). These values γ indicate deviations from purely thermally activated normal diffusion $\gamma = 1.0$. In short, individual Fe atoms undergo subdiffusion ($\gamma < 1.0$) along the armchair and superdiffusion ($\gamma > 1.0$) along the zigzag. The probability distribution of displacements (l) between successive jumps also follows a power law $P(l) \sim l^{-\mu}$ (rather than an exponential one),

where $\mu = 2.2$ at the armchair and $\mu = 1.8$ on the edges of the zigzag. The law can express the probability distribution of the time interval between two successive jumps $P(\tau) \sim \tau^{-\nu}$, where $\nu = 0.9$ for the armchair and $\nu = 1.1$ for zigzag. The deviation $< l^2 >$ at $\mu < 2.0$ and divergence $< \tau >$ at $\nu < 1.0$ at the time boundary, will lead to superdiffusion (levitation) and subdiffusion, respectively [250, 251]. In the case of diffusion of the iron atom, the competition between large jumps and long dwell times at a given location can lead to crossovers between different diffusion regimes. The relationships between μ, ν and γ (according to the continuous time displacement model: $\gamma = 2 + \nu - \mu, \nu < 1$ or $\gamma = 3 - \mu, \nu > 1$) [250], where μ and ν are the parameters of the probability distributions can give values γ in cases of displacement of the Fe atom, both along the armchair and along the zigzag edges.

Moreover, changing the electron beam intensity does not change the nature of the anomalous diffusion of the Fe atom (see Fig. 20). The measurements of the displacement of a single Fe atom on the same graphene edge (a mixed edge consisting of zigzag and armchair regions) at three different beam intensities showed that the diffusion of a single Fe atom follows the superdiffusion law. The fitted exponents of the power law are 1.15, 1.10, and 1.11 (from low to high electron beam intensities) and are independent of the beam intensity. Although the exponents of the power law are quite close, the parameters of the linear fit (pre-exponential factors in the power law formula) differ significantly for different intensities. Based on the obtained formulas for the power law, one can easily derive an expression for the generalized diffusion coefficient K_ν^μ by fitting the values using the MSD method to the following equation [250]:

$$\langle R^2(t) \rangle = \frac{2K_\nu^\mu}{\Gamma(1+\nu)} t^{2+\nu-\mu} \tag{17}$$

(in the case of superdiffusion, we can assume that $\nu = 1$). The generalized diffusion coefficient K_ν^μ linearly correlates with the beam intensity. A deeper analysis reveals the presence of a superdiffusion regime with γ = 1.25, which is similar to the experimentally obtained value γ = 1.2.

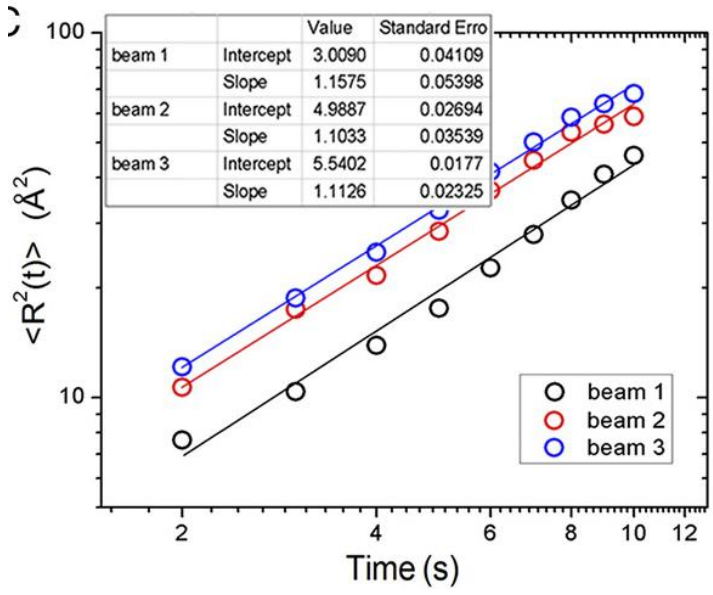

Fig. 20. The MSD of the Fe atom on the same graphene mixed edge under three different beam intensities. The inset shows the power law-fitting parameters for the three beam intensities [244]

Previously [231], it was shown that electrons accelerated to 80 kV are capable of sputtering C atoms on graphene edges in a lightning-like manner. In the presence of Fe atoms on the graphene edges, removal of C atoms was also observed. Still, the Fe atom always remained on the edge of the graphene sheet at the location from which the last C atom was removed, indicating the participation of the Fe atom in this process. More importantly, the Fe atom

sometimes participates in the insertion of carbon atoms into the graphene edge (i.e., the catalytic growth of sp^2-carbon material is directly observed). Examples of this process are shown in Fig. 19. First, the Fe atom is drawn into a five-atom ring (pentagon), after which a C atom is inserted into it, forming a six-atom (hexagonal) ring; finally, the Fe atom leaves the hexagonal ring and is replaced by a C atom, creating an all-carbon hexagon. These experimental observations are consistent with theoretical predictions [248].

The experimentally observed growth cycle is shown in Fig. 21*A*, where the DFT-calculated energies defining each stage of the cycle are given. For a deeper understanding, high-temperature DFT tight-binding MD (DFTB-MD) simulations were performed [2, 56] to reproduce the catalytic process. In essence, DFTB-MD simulations highlight the importance of the chemical affinity of Fe, which allows the Fe atom to bind nearby C atoms and transfer the trapped C atoms to nearby growth sites. Many of the translational states (e.g., C atoms trapped by Fe atoms) are challenging to observe experimentally due to the time resolution of the instrument; however, the initial and final states, which are more stable, are well captured. The high-temperature DFTB-MD simulations performed here allow the process to be accelerated and thus make such simulations feasible. Although these simulations are not precisely equivalent to the electron beam-driven processes observed in experiments, they nevertheless show possible reaction pathways and routes at the graphene edges, and the results are consistent with the reduction in total energy and experimental observations that the process is initiated and maintained by the electron beam.

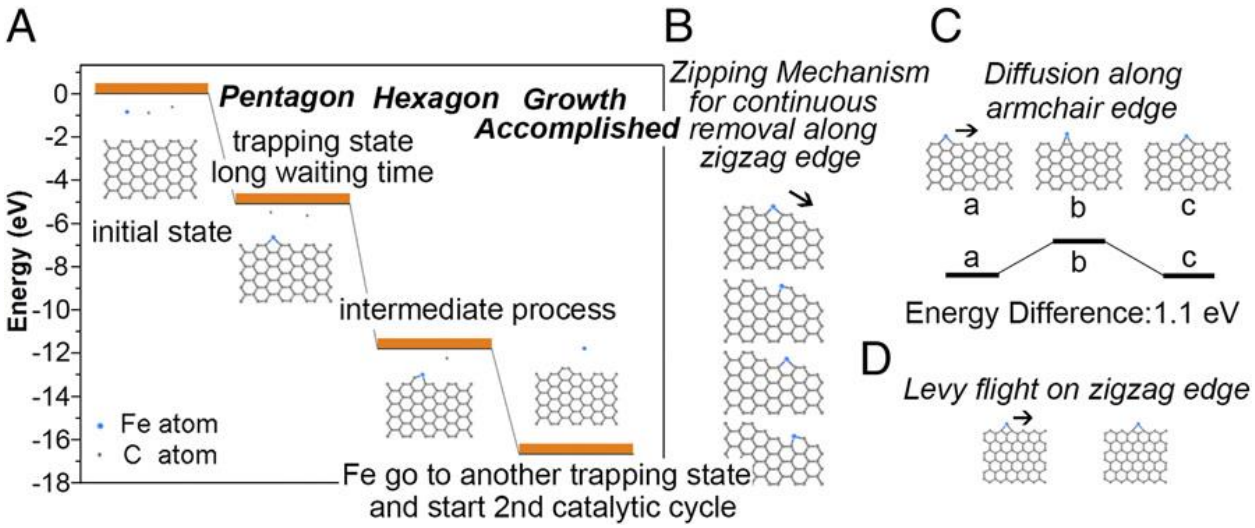

Fig. 21. The catalytic and diffusion processes. (A) DFT-calculated energies for four steps in catalytically grown G from a single Fe atom. (B) The unzipping model for removing one layer from a G zigzag edge of G by a single Fe atom. The reverse process is zipping growth. (C) The movement of a single Fe atom at an armchair edge. The DFT-calculated energies show the trapping state at an armchair edge. (D) The flat energy landscape obtained on a zigzag edge is caused by the similarity of each saddle point [244]

Now we can turn to the physical picture of the electron beam-induced diffusion of Fe atoms on the graphene edge. The beam energy is constant at 80 kV, meaning that the average energy transfer from high-energy electrons to the target atoms remains constant. It has already been shown in the literature [255] that at the TEM beam intensity, the electrons mainly interact with the target atoms in turns. Therefore, it is reasonable to assume that the distribution of the Fe atom hopping length will not depend strongly on the electron beam intensity (since the electron energy does not change, only the electron flux intensity changes). However, if the beam intensity is varied, the average waiting time τ between two hops will be inversely proportional to the beam intensity.

In the case of superdiffusion, it can be assumed that $\nu = 1$, and from Fig. 20*d*, it can be seen that $1/\tau$ depends linearly on the beam intensity [244], which is consistent with the electron beam activation model. Furthermore, without the electron beam, according to the MD simulation, the anomalous diffusion behaviour can still prevail.

Finally, it was shown in [244] that, using aberration-corrected TEM, the diffusion of single Fe atoms at graphene edges depends on the edge type (zigzag and armchair), with subdiffusion occurring at armchair edge embedding and superdiffusion occurring at zigzag edge embedding. Theoretical calculations suggest that this difference is due to different diffusion barriers between the edge states. More importantly, in situ studies directly documented the catalytic removal and addition of carbon atoms at the sp^2-hybridized edge of a graphene sheet in the presence of a single Fe atom under electron irradiation. Anomalous diffusion behaviour is expected to affect the growth/catalysis kinetics of synthetic sp^2 nanomaterials grown using metal catalysts. The conducted *in situ* observations and theoretical studies (MD and DFT) provide key insights into the fundamental growth processes of sp^2 nanostructures, such as graphene and carbon nanotubes, on metal catalysts.

CONCLUSIONS

The review considers the results of quantum chemical studies of the properties of electrocatalysts based on iron-containing carbons, primarily graphene. First, the works in which the assignment of N1*s* peaks was performed are analysed in XPS depending on the type of nitrogen atom state in electrocatalysts obtained by pyrolysis of a mixture of carbon-, nitrogen-, and iron-containing precursors. The results of catalyst tests in OOR are presented. The combined use of data from experimentally obtained XPS spectra and quantum-chemical calculations on chemically induced shifts in the energy of the N1*s* core levels made it possible to semi-quantitatively determine the content of different types of nitrogen atoms in OOR electrocatalysts. The results showed that as the degree of nitrogen doping of graphenes-FeN_x ($x = 1, 2, 3, 4$) increases, their catalytic activity in OOR increases.

The RRDE data are consistent with the proposal that the graphite-like nitrogen-containing moieties produced at lower temperatures contribute significantly to the formation of hydrogen peroxide in ORR, while the metal coordinated to the nitrogen is critical for the complete oxygen reduction reaction.

The quantitative analysis of the regions of the EXAFS and XANES spectra of FeN-C catalysts free or nearly free of Fe crystalline structures revealed the existence of porphyrin-like FeN_4C_{12} moieties in them, which is in strong contrast to the previously proposed FeN_xC_y moieties with nitrogen atoms incorporated into six-membered rings. Electrochemical studies indicate that FeN_4C_{12} moieties catalyse the four-electron reduction of O_2 to water. The porphyrin-like moieties can be formed either in highly disordered graphene sheets or between the zigzag edges of graphene sheets, resulting in the formation of micropores. FeN-C catalysts subjected to Ar- and NH_3-pyrolysis demonstrate completely different activities in ORR. The increase in ORR activity caused by FeN_4C_{12} type fragments is due to the highly basic N-groups formed during pyrolysis with NH_3.

DFT calculations of the detailed kinetic and thermodynamic course of ORR on the FeN_4-G catalyst with all pyrrole nitrogen atoms showed that the activation energy for the dissociation of an adsorbed O_2 molecule is very high, regardless of its adsorption type on the FeN_4-G catalyst in the Pauling or Griffiths model configuration. The most probable sequence of stages of the four-electron reduction mechanism may correspond to the following order:

$$O_{2(ads)} \rightarrow OOH_{(ads)} \rightarrow O_{(ads)} + H_2O_{(ads)} \text{ (or } 2OH_{(ads)}) \rightarrow OH_{(ads)} + H_2O_{(ads)} \rightarrow 2H_2O_{(ads)}.$$

The calculated ORR free energy diagrams show that for all its elementary steps via the four-electron mechanism, the free energy changes (ΔG) are negative at low electrode potential

(up to 0.41 V). The rate-limiting step of the overall ORR is the reduction of $OH_{(ads)}$ to $H_2O_{(ads)}$, with E_{act} = 1.02 eV. The product of the two-electron reduction, H_2O_2, can be chemisorbed on the catalyst surface, and the free energy diagrams show that the decrease of OOH to H_2O_2 occurs at positive free energy changes for any positive electrode potential compared to the conventional hydrogen electrode. The high positive ΔG value for hydrogen peroxide formation indicates that the two-electron ORR route is unfavourable on FeN_4-G type catalysts.

The first self-consistent comparison of the activity of several potential structures of the active site edge defects of iron-containing catalysts based on graphene nanocarbon has shown that, depending on the synthesis conditions, the most stable Fe-containing defects are structures with four or three nitrogen atoms. It is assumed that both of these structures can coexist. The energy of the interribbon configuration with two nitrogen atoms in each ribbon is so much higher than that of the other structures studied that its existence is assumed to be either thermodynamically forbidden or metastable relative to its decay. FeN_3 (Fe_2N_5) type cluster structures appear to be able to cleave the O_2 bond with zero activation barrier and hence can direct ORR along a dissociative route. This route is expected to be more selective, without H_2O_2 formation, due to excess binding of ORR intermediates. Ab initio molecular dynamics data suggest that this spontaneous reaction is unlikely to be affected by solvation, as the solvent does not appear to alter the stability of the edge defects considered.

The results obtained by the DFT method showed that with an increase in the degree of doping with nitrogen atoms in graphenes-FeN_x (x = 4, 3, 2, 1), their activity in the hydrochlorination reaction consistently increases. The following order of E_{act} was obtained for the catalytic reaction of the graphene-FeN_x catalyst series: graphene-FeN_1 > graphene-FeN_2 > graphene-FeN_3 > graphene-FeN_4. There are three configurations of graphene-FeN_2 catalysts based on the relative positions of N atoms. The following order of energy barriers was obtained for them: graphene-FeN_2-Hex > graphene-FeN_2-Oppo > graphene-FeN_2-Pen. Graphene-FeN_4 demonstrated the highest activity in the production of vinyl chloride catalysed by catalysts made of base metals.

Without applying an external electric field, the Fe atom embedded in the graphene network activates the methane molecule with an activation energy of 25.7 kcal/mol. The stability of the adsorption complexes, transition states, and products changes significantly under the action of the direction and strength of the applied electric field. A positive electric field destabilizes the adsorption complexes, while the transition state and products are more stable compared to the case without a field. The activation energy decreased significantly from 25.7 to 17.5 kcal/mol when an electric field of +0.015 au was applied. The results indicate that an applied external electric field can regulate the catalytic activity of iron-doped graphene.

Aberration-corrected TEM revealed that the diffusion of single Fe atoms at graphene edges is dependent on the edge type (zigzag and armchair), with subdiffusion occurring at armchair edges and superdiffusion at zigzag edges. Theoretical calculations show that this difference is due to different diffusion barriers between the stable states. In situ studies directly documented the catalytic removal or addition of carbon atoms to the sp^2-hybridized edge of a graphene sheet in the presence of a single Fe atom when the sample was irradiated with electrons of the energy used in TEM experiments. It can be expected that the anomalous diffusion behaviour will affect the growth/catalysis kinetics of synthetic sp^2 nanomaterials grown using metal catalysts. The conducted *in situ* observations and theoretical studies (MD and DFT) provide key insights into the fundamental growth processes of sp^2 nanostructures, such as graphene and carbon nanotubes, on metal catalysts.

REFERENCES

1. Castro Neto A. H., Guinea F., Peres N. M. R., Novoselov K. S., Geim A. K. The electronic properties of graphene. *Rev. Mod. Phys.* 2009. **81**(1): 109.

2. Mao Y., Yuan J., Zhong J. Density functional calculation of transition metal adatom adsorption on graphene. *J. Phys.: Condens. Matter*. 2008. **20**(11): 115209.
3. Zhang Y., Talapatra S., Kar S., Vajtai R., Nayak S. K., Ajayan P. M. First-Principles Study of Defect-Induced Magnetism in Carbon. *Phys. Rev. Lett*. 2007. **99**(10): 107201.
4. Topsakal M., Aktürk E., Sevinçli H., Ciraci S. First-principles approach to monitoring the band gap and magnetic state of a graphene nanoribbon via its vacancies. *Phys. Rev*. 2008. **78**(23): 235435.
5. Susi T., Kotakoski J., Kepaptsoglou D., Mangler C., Lovejoy T.C., Krivanek O. L., Zan R., Bangert U., Ayala P., Meyer J.C., Ramasse Q. Silicon-Carbon Bond Inversions Driven by 60-keV Electrons in Graphene. *Phys. Rev. Lett*. 2014. **113**(11): 115501.
6. Das S., Kim M., Lee J., Choi W. Synthesis, Properties, and Applications of 2-D Materials: A Comprehensive Review. *Crit. Rev. Solid State Mater. Sci*. 2014. **39**(4): 231.
7. Geim A. K., Novoselov K. S. The rise of graphene. *Nat. Mater*. 2007. **6**(3): 183.
8. Yazyev O. V., Helm L. Defect-induced magnetism in graphene. *Phys. Rev. B*. 2007. **75**(12): 125408.
9. Novoselov K. S., Jiang Z., Zhang Y., Morozov S. V., Stormer H. L., Zeitler U., Maan J. C., Boebinger G. S., Kim P., Geim A. K. Room-Temperature Quantum Hall Effect in Graphene. *Science*. 2007. **315**(5817): 1379.
10. Zhang Y., Tan Y. W., Stormer H. L., Kim P. Experimental observation of the quantum Hall effect and Berry's phase in graphene. *Nature*. 2005. **438**(7065): 201.
11. Ding J., Qiao Z., Feng W., Yao Y., Niu Q. Engineering quantum anomalous/valley Hall states in graphene via metal-atom adsorption: An *ab-initio* study. *Phys. Rev. B*. 2011. **84**(19): 195444.
12. Guinea F., Katsnelson M. I., Geimet A. K. Energy gaps and a zero-field quantum Hall effect in graphene by strain engineering. *Nat. Phys*. 2010. **6**: 30.
13. Oostinga J. B., Heersche H. B., Liu X., Morpurgo A. F., Vandersypen L. M. K. Gate-induced insulating state in bilayer graphene devices. *Nat. Mater*. 2008. **7**: 151.
14. Luo G., Liu L., Zhang J., Li G., Wang B., Zhao J. Hole Defects and Nitrogen Doping in Graphene: Implication for Supercapacitor Applications. *ACS Appl. Mater. Interfaces*. 2013. **5**: 11184.
15. Nishad A. K., Sharma R. Analytical time-domain models for performance optimization of multilayers GNR interconnects. *IEEE Journal of Selected Topics in Quantum Electronics*. 2014. **20**(1): 3700108.
16. Nirmalraj P. N., Lutz T., Kumar S., Duesberg G. S., Boland J. J. Nanoscale mapping of electrical resistivity and connectivity in graphene strips and networks. *Nano Lett*. 2011. **11**(1): 16.
17. Rakheja S., Kumar V., Naeemi A. Evaluation of the potential performance of graphene nanoribbons as on-chip interconnects. Proceedings of the IEEE. 2013. **101**(7): 1740.
18. Huang C., Li C., Shi. G. Graphene-based Catalysts. *Energy and Environment*. 2012. **2**(10): 8848.
19. Zutic I., Fabian J., Das Sarma S. Spintronics: Fundamentals and applications. *Rev. Modern Phys*. 2004. **76**: 323.
20. Thomas C. E. Fuel cell and battery electric vehicles compared. *Int. J. Hydrogen Energ*. 2009. **34**: 6005.
21. Borup R., Meyers J., Pivovar B., Kim Y. S., Mukundan R., Garland N., Myers D., Wilson M., Garzon F., Wood D., Zelenay P., More K., Stroh K., Zawodzinski T., Boncella J., McGrath J. E., Inaba M., Miyatake K., Hori M., Ota K., Ogumi Z., Miyata S., Nishikata A., Siroma Z., Uchimoto Y., Yasuda K., Kimijima K., Iwashita N. Scientific Aspects of Polymer Electrolyte Fuel Cell Durability and Degradation. *Chem. Rev*. 2007. **107**(10): 3904.

22. Greeley J., Stephens I. E. L., Bondarenko A. S., Johansson T. P., Hansen H. A., Jaramillo T. F., Rossmeisl J., Chorkendorff I., Norskov J. K. Alloys of platinum and early transition metals as oxygen reduction electrocatalysts. *Nat. Chem*. 2009. **1**: 552.
23. Sun J., Fang Y. H., Liu Z. P. Electrocatalytic oxygen reduction kinetics on Fe-center of nitrogen-doped graphene. *Phys. Chem. Chem. Phys*. 2014. **16**: 13733.
24. Serov A., Artyushkova K., Andersen N. I., Stariha S., Atanassov P. Original Mechanochemical Synthesis of Non-Platinum Group Metals Oxygen Reduction Reaction Catalysts Assisted by Sacrificial Support Method. *Electrochim. Acta*. 2015. **179**: 154.
25. Kruusenberg I., Matisen L., Shah Q., Kannan A. M., Tammeveski K. Non-platinum cathode catalysts for alkaline membrane fuel cells. *Int. J. Hydrogen Energ*. 2012. **37**: 4406.
26. Prehn K., Warburg A., Schilling T., Bron M., Schulte K. Towards nitrogen-containing CNTs for fuel cell electrodes. *Compos. Sci. Technol*. 2009. **69**(10): 1570.
27. Artyushkova K., Walker C., Patterson W., Atanassov P. Hierarchically Structured Non-PGM Oxygen Reduction Electrocatalyst Based on Microemulsion-Templated Silica and Pyrolyzed Iron and Cyanamide Precursors. *Electrocatalysis*. 2014. **5**(4): 241.
28. Robson M. H., Serov A., Artyushkova K., Atanassov P. A mechanistic study of 4-aminoantipyrine and iron derived non-platinum group metal catalyst on the oxygen reduction reaction. *Electrochim. Acta*. 2013. **90**: 656.
29. Kramm U. I., Herranz J., Larouche N., Arruda T. M., Lefèvre M., Jaouen F., Bogdanoff P., Fiechter S., Abs-Wurmbach I., Mukherjee S., Dodelet J. Structure of the catalytic sites in Fe/N/C-catalysts for O2-reduction in PEM fuel cells. *Phys. Chem. Chem. Phys*. 2012. **14**: 11673.
30. Chen Z., Higgins D., Chen Z. Electrocatalytic activity of nitrogen doped carbon nanotubes with different morphologies for oxygen reduction reaction. *Electrochim. Acta*. 2010. **55**: 4799.
31. Ostadi H., Rama P., Liu Y., Chen R., Zhang X. X., Jiang K. 3D reconstruction of a gas diffusion layer and a microporous layer. *J. Membr. Sci*. 2010. **351**: 69.
32. Kattel S., Atanassov P., Kiefer B. Stability, Electronic and Magnetic Properties of In-Plane Defects in Graphene: A First Principles Study. *J. Phys. Chem. C*. 2012. **116**: 816.
33. Vikkisk M., Kruusenberg I., Joost U., Shulga E., Tammeveski K. Electrocatalysis of oxygen reduction on nitrogen-containing multi-walled carbon nanotube modified glassy carbon electrodes. *Electrochim. Acta* 2013. **87**: 709.
34. Tylus U., Jia Q., Strickland K., Ramaswamy N., Serov A., Atanassov P., Mukerjee S. Elucidating oxygen reduction active sites in pyrolyzed metal nitrogen coordinated non-precious-metal electrocatalyst systems. *J. Phys. Chem. C*. 2014. **118**: 8999.
35. Wong W. Y., Daud W. R. W., Mohamad A. B., Kadhum A. A. H., Loh K. S., Majlan E. H. Recent progress in nitrogen-doped carbon and its composites as electrocatalysts for fuel cell applications. *Int. J. Hydrogen Energ*. 2013. **38**: 9370.
36. Stevie F. A., Donley C. L. Introduction to x-ray photoelectron spectroscopy. *J. Vac. Sci. Technol. A*. 2020. **38**: 063204-1.
37. Niwa H., Kobayashi M., Horiba K., Harada Y., Oshima M., Terakura K., Ikeda T., Koshigoe Y., Ozaki J., Miyata S., Ueda S., Yamashita Y., Yoshikawa H., Kobayashi K. X-ray photoemission spectroscopy analysis of N-containing carbon-based cathode catalysts for polymer electrolyte fuel cells. *J. Power Sources*. 2011. **196**: 1006.
38. Wood K. N., O'Hayre R., Pylypenko S. Recent progress on nitrogen/carbon structures designed for use in energy and sustainability applications. *Energ. Environ. Sci*. 2014. **7**: 1212.
39. Pels J. R., Kapteijn F., Moulijn J. A., Zhu Q., Thomas K. M. Evolution of nitrogen functionalities in carbonaceous materials during pyrolysis. *Carbon*. 1995. **33**: 1641.

40. Shao Y. Y., Zhang S., Engelhard M. H., Li G. S., Shao G. C., Wang Y., Liu J., Aksay I. A., Lin Y. H. Nitrogen-doped graphene and its electrochemical applications. *J. Mater. Chem*. 2010. **20**: 7491.
41. Kabir S., Artyushkova K., Serov A., Kiefer B., Atanassov P. Binding energy shifts for nitrogen-containing graphene-based electrocatalysts – experiments and DFT calculations. *Surf. Interface Anal*. 2016. **48**: 293.
42. Wang S. Y., Zhang L. P., Xia Z. H., Roy A., Chang D. W., Baek J. B., Dai L. M. BCN Graphene as Efficient Metal-Free Electrocatalyst for the Oxygen Reduction Reaction. *Angew Chem. Int. Edit*. 2012. **51**: 4209.
43. Yang S. B., Feng X. L., Mullen K. Sandwich-Like, Graphene-Based Titania Nanosheets with High Surface Area for Fast Lithium Storage. *Adv. Mater*. 2011. **23**: 3575.
44. Zheng B., Wang J., Wang F.-B., Xia X.-H. Synthesis of nitrogen doped graphene with high electrocatalytic activity toward oxygen reduction reaction. *Electrochem. Commun*. 2013. **28**: 24.
45. Xia W., Masa J., Bron M., Schuhmann W., Muhler M. Highly active metal-free nitrogen-containing carbon catalysts for oxygen reduction synthesized by thermal treatment of polypyridine-carbon black mixtures. *Electrochem. Commun*. 2011. **13**: 593.
46. Kohn W., Sham L.S. Self-consistent equation including exchange and correlation effect. *Phys. Rev. A*. 1965. **140**(4): 1133.
47. Parr R. G., Yang W. *Density-functional theory of atoms and molecules*. (Oxford: Oxford Univ. Press., 1989).
48. Perdew J. P., Chevary J., Vosko S., Jackson K. A., Pederson M. R., Singh D., Fiolhais C. Atoms, molecules, solids, and surfaces: Applications of the generalized gradient approximation for exchange and correlation. *Phys. Rev. B*. 1992. **46**: 6671.
49. Kabir S., Artyushkova K., Kiefer B., Atanassov P. *Phys. Chem. Chem. Phys*. 2015. **17**: 17785.
50. Artyushkova K., Kiefer B., Halevi B., Knop-Gericke A., Schlogl R., Atanassov P. Density functional theory calculations of XPS binding energy shift for nitrogen-containing graphene-like structures. *Chem. Commun*. 2013. **49**: 2539.
51. Beamson G., Briggs D. *High resolution XPS of organic polymers: the scienta ESCA300 database* (1992).
52. Naumkin A. V., Kraut-Vass A., Gaarenstroom S. W., Powell C. J. *NIST X-ray Photoelectron Spectroscopy Database* (2006) http://srdata.nist.gov/xps/.
53. Serov A., Artyushkova K., Atanassov P. Fe-N-C Oxygen Reduction Fuel Cell Catalyst Derived from Carbendazim: Synthesis, Structure, and Reactivity. *Adv. Energy Mater*. 2014. **4**: 1301735.
54. Kramm U. I., Abs Wurmbach I., Herrmann-Geppert I., Radnik J., Fiechter S., Bogdanoff P. Influence of the Electron-Density of FeN[sub$_4$]-Centers Towards the Catalytic Activity of Pyrolyzed FeTMPPCl-Based ORR-Electrocatalysts. *J. Electrochem. Soc*. 2011. **158**(1): B69.
55. S. Maldonado, Stevenson K. J. Influence of nitrogen doping on oxygen reduction electrocatalysis at carbon nanofiber electrodes. *J. Phys. Chem. B*. 2005. **109**: 4707.
56. Sidik R. A., Anderson A. B., Subramanian N. P., Kumaraguru S. P., Popov B. N. O_2 reduction on graphite and nitrogen-doped graphite: experiment and theory. *J. Phys. Chem. B*. 2006. **110**: 1787.
57. Wiggins-Camacho D., Stevenson K. J. Indirect electrocatalytic degradation of cyanide at nitrogen-doped carbon nanotube electrodes. *J. Phys. Chem. C*. 2011. **115**: 20002.
58. Unni S. M., Devulapally S., Karjule N., Kurungot S. Graphene enriched with pyrrolic coordination of the doped nitrogen as an efficient metal-free electrocatalyst for oxygen reduction. *J. Mater. Chem*. 2012. **22**: 23506.

59. Cong H.-P., Wang P., Gong M., Yu S.-H. Facile synthesis of mesoporous nitrogen-doped graphene: an efficient methanol – tolerant cathodic catalyst for oxygen reduction reaction. *Nano Energy*. 2014. **3**: 55.
60. Othman R., Dicks A. L., Zhu Z. H. Non precious metal catalysts for the PEM fuel cell cathode. *Int. J. Hydrogen Energ*. 2012. **37**: 357.
61. Wagner F. T., Lakshmanan B., Mathias M. F. Electrochemistry and the future of the automobile. *J. Phys. Chem. Lett*. 2010. **1**: 2204.
62. Jasinski R. A new fuel cell cathode catalyst. *Nature*. 1964. **201**: 1212.
63. Jahnke H., Schönborn M., Zimmermann G. *Physical and Chemical Applications of Dyestuffs Vol. 61* (Springer, 1976).
64. Gupta S., Tryk D., Bae I., Aldred W., Yeager E. Heat-treated polyacrylonitrile-based catalysts for oxygen electroreduction. *J. Appl. Electrochem*. 1989. **19**: 19.
65. Jaouen F. et al. Recent advances in non-precious metal catalysis for oxygen-reduction reaction in polymer electrolyte fuel cells. *Energy Environ. Sci*. 2011. **4**: 114.
66. Proietti E. et al. Iron-based cathode catalyst with enhanced power density in polymer electrolyte membrane fuel cells. *Nature Commun*. 2011. **2**: 416.
67. Wu G., More K. L., Johnston C. M., Zelenay P. HighPerformance Electrocatalysts For Oxygen Reduction Derived From Polyaniline, Iron, And Cobalt. *Science*. 2011. **332**: 443.
68. Koslowski U. I., Abs-Wurmbach I., Fiechter S., Bogdanoff P. Nature of the catalytic centers of porphyrin-based electrocatalysts for the ORR: A correlation of kinetic current density with the site density of Fe-N_4 centers. *J. Phys. Chem. C*. 2008. **112**: 15356.
69. Kramm U. I., Lefèvre M., Larouche N., Schmeisser D., Dodelet J.-P. Correlations between mass activity and physicochemical properties of Fe/N/C catalysts for the ORR in PEM fuel cell via ^{57}Fe Mössbauer spectroscopy and other techniques. *J. Am. Chem. Soc*. 2014. **136**: 978.
70. Lefèvre M., Dodelet J. P., Bertrand P. Molecular oxygen reduction in PEM fuel cells: Evidence for the simultaneous presence of two active sites in Fe-based catalysts. J. *Phys. Chem. B*. 2002. **106**: 8705
71. Lefèvre M., Proietti E., Jaouen F., Dodelet J.-P. Iron-based catalysts with improved oxygen reduction activity in polymer electrolyte fuel cells. *Science*. 2009. **324**: 71.
72. Charreteur F., Jaouen F., Ruggeri S., Dodelet J.-P. Fe/N/C non-precious catalysts for PEM fuel cells: Influence of the structural parameters of pristine commercial carbon blacks on their activity for oxygen reduction. *Electrochim. Acta*. 2008. **53**: 2925.
73. Matter P. H., Wang E., Millet J.-M. M., Ozkan U. S. Characterization of the iron phase in CN_x-based oxygen reduction reaction catalysts. *J. Phys. Chem. C*. 2007. **111**: 1444.
74. Subramanian N. P. et al. Nitrogen-modified carbon-based catalysts for oxygen reduction reaction in polymer electrolyte membrane fuel cells. *J. Power Sources*. 2009. **188**: 38.
75. Thorum M. S., Hankett J. M., Gewirth A. A. Poisoning the oxygen reduction reaction on carbon-supported Fe and Cu electrocatalysts: Evidence for metal-centered activity. *J. Phys. Chem. Lett*. 2011. **2**: 295.
76. Ganesan,S., Leonard N., Barton S. C. Impact of transition metal on nitrogen retention and activity of iron-nitrogen-carbon oxygen reduction catalysts. *Phys. Chem. Chem. Phys*. 2014. **16**: 4576.
77. Kattel S., Atanassov P., Kiefer B. Density functional theory study of the oxygen reduction reaction mechanism in a BN Co-doped grapheme electrocatalyst. *J. Mater. Chem. A*. 2014. **2**: 10273.
78. Szakacs C. E., Lefevre M., Kramm U. I., Dodelet, J.-P., Vidal, F. A density functional theory study of catalytic sites for oxygen reduction in Fe/N/C catalysts used in H_2/O_2 fuel cells. *Phys. Chem. Chem. Phys*. 2014. **16**: 13654.

79. Holby E. F., Wu G., Zelenay P., Taylor C. D. Structure of Fe-N_x-C defects in oxygen reduction reaction catalysts from first-principles modeling. *J. Phys. Chem. C*. 2014. **118**: 14388.
80. Hijazi I. et al. Carbon nanotube-templated synthesis of covalent porphyrin network for oxygen reduction reaction. *J. Am. Chem. Soc*. 2014. **136**: 6348.
81. Zitolo A., Goellner V., Armel V., Sougrati M.-T., Mineva T., Stievano L., Fonda E., Jaouen F. Identification of catalytic sites for oxygen reduction in iron- and nitrogen-doped graphene materials. *Nat. Matter*. 2015. **14**: 937.
82. Grimme S., Ehrlich S., Goerigk L. Effect of the damping function in dispersion corrected density functional theory. *J. Comput Chem*. 2011. **32**(7): 1456.
83. Grimme S. Density functional theory with London dispersion corrections. *WIREs Comput. Mol. Sci*. 2011. **1**(2): 211.
84. Herranz J. et al. Unveiling N-protonation and anion-binding effects on Fe/N/C catalysts for O_2 reduction in proton-exchange-membrane fuel cells. *J. Phys. Chem. C*. 2011. **115**: 16087.
85. Hu Y. et al. Hollow spheres of iron carbide nanoparticles encased in graphitic layers as oxygen reduction catalysts. *Angew. Chem. Int. Ed*. 2014. **53**: 3675.
86. Sun S., Jiang N., Xia, D. Density functional theory study of the oxygen reduction reaction on metalloporphyrins and metallophthalocyanines. *J. Phys. Chem. C*. 2011. **115**: 9511.
87. Rovira C., Kunc K., Hutter J., Ballone P., Parrinello, M. Equilibrium geometries and electronic structure of iron-porphyrin complexes: A density functional study. *J. Phys. Chem. A*. 1997. **101**: 8914.
88. D'Angelo P., Zitolo A., Migliorati V., Persson I. Analysis of the detailed configuration of hydrated lanthanoid(III) ions in aqueous solution and crystalline salts by using K- and L3-edge XANES spectroscopy. *Chem. Eur. J*. 2010. **16**: 684.
89. Zitolo A., Chillemi G., D'Angelo P. X-ray absorption study of the solvation structure of Cu_2^+ in methanol and dimethyl sulfoxide. *Inorg. Chem*. 2012. **51**: 8827.
90. Westre T. E. et al. A multiplet analysis of Fe K-edge 1s → 3d pre-edge features of iron complexes. *J. Am. Chem. Soc*. 1997. **119**: 6297.
91. D'Angelo P. et al. X-ray absorption spectroscopy of hemes and hemeproteins in solution: Multiple scattering analysis. *Inorg. Chem*. 2008. **47**: 9905.
92. D'Angelo, P. et al. Dynamic investigation of protein metal active sites: Interplay of XANES and molecular dynamics simulations. *J. Am. Chem. Soc*. 2010. **132**: 14901.
93. Kattel S., Atanassov P., Kiefer, B. Catalytic activity of Co-Nx/C electrocatalysts for oxygen reduction reaction: A density functional theory study. *Phys. Chem. Chem. Phys*. 2013. **15**: 148.
94. Holby E. F., Taylor C. D. Control of Graphene Nanoribbon Vacancies By Fe And N Dopants: Implications For Catalysis. *Appl. Phys. Lett*. 2012. **101**: 064102−1.
95. Kirner J. F., Dow W., Scheidt W. R. Molecular stereochemistry of two intermediate-spin complexes. Iron(II) phthalocyanine and manganese(II) phthalocyanine. *Inorg. Chem*. 1976. **15**: 1685.
96. Nallathambi V., Leonard N., Kothandaraman R., Barton S. C. Nitrogen precursor effects in iron–nitrogen–carbon oxygen reduction catalysts. *Electrochem. Solid State Lett*. 2011. **14**: B55.
97. Bezerra C. W. B., Zhang L., Lee K., Liu H., Marques A. L. B., Marques E. P., Wang H., Zhang J. A review of Fe–N/C and Co–N/C catalysts for the oxygen reduction reaction. *Electrochimica Acta*. 2008. **53**: 4937.
98. Ziegelbauer J. M., Olson T. S., Pylypenko S., Alamgir F., Jaye C., Atanassov P., Mukerjee S. Direct Spectroscopic Observation of the Structural Origin of Peroxide

Generation from Co-Based Pyrolyzed Porphyrins for ORR Applications. *J. Phys. Chem. C*. 2008. **112**: 8839.
99. Lefèvre M., Dodelet J.-P. Fe-based catalysts for the reduction of oxygen in polymer electrolyte membrane fuel cell conditions: determination of the amount of peroxide released during electroreduction and its influence on the stability of the catalysts. *Electrochimica Acta*. 2003. **48**: 2749.
100. Lefèvre M., Dodelet J. P., Bertrand P. O_2 Reduction in PEM Fuel Cells: Activity and Active Site Structural Information for Catalysts Obtained by the Pyrolysis at High Temperature of Fe Precursors. *J. Phys. Chem. B*. 2000. **104**: 11238.
101. Lefèvre M., Proietti E., Jaouen F., Dodelet J. P. Iron-based catalysts with improved oxygen reduction activity in polymer electrolyte fuel cells. *Science*. 2009. **324**: 71.
102. Titov A., Zapol P., Kral P., Liu D.-J., Iddir H., Baishya K., Curtiss L. A. Catalytic Fe-xN Sites in Carbon Nanotubes. *J. Phys. Chem. C*. 2009. **113**: 21629.
103. Maruyama J., Abe I. Structure control of a carbon-based noble-metal-free fuel cell cathode catalyst leading to high power output. *Chem. Commun*. 2007. **27**: 2879.
104. Maruyama J., Okamura J., Miyazaki K., Abe I. Two-Step Carbonization as a Method of Enhancing Catalytic Properties of Hemoglobin at the Fuel Cell Cathode. *J. Phys. Chem. C*. 2007. **111**(18): 6597.
105. Maruyama J., Fukui N., Kawaguchi M., Abe I. Application of nitrogen-rich amino acids to active site generation in oxygen reduction catalyst. *J. Power Sources*. 2008. **182**: 489.
106. Byon H. R., Suntivich J., Shao-Horn Y. Graphene-Based Non-Noble-Metal Catalysts for Oxygen Reduction Reaction in Acid. *Chem. Mater*. 2011. **23**: 3421.
107. Calle-Vallejo F., Martinez J. I., Rossmeisl J. Density Functional Studies Of Functionalized Graphitic Materials With Late Transition Metals For Oxygen Reduction Reactions. Phys. Chem. Chem. Phys. 2011. **13**: 15639.
108. Lee D. H., Lee W. J., Lee W. J., Kim S. O. Theory, Synthesis, and Oxygen Reduction Catalysis of Fe-Porphyrin-Like Carbon Nanotube. Phys. Rev. Lett. 2011. **106**: 175502-1.
109. Chen R., Li H., Chu D., Wang D. Unraveling Oxygen Reduction Reaction Mechanism on Carbon-Supported Fe-Phthalocyanine and Co-Phthalocyanine Catalysts in Alkaline Solutions. J. Phys. Chem. C. 2009. **113**: 20689.
110. Sun S., Jiang N., Xia D. Density Functional Theory Study of the Oxygen Reduction Reaction on Metalloporphyrins and Metallophthalocyanines. *J. Phys. Chem. C*. 2011. **115**: 9511.
111. Zhang J., Wang Z., Zhu Z. The inherent kinetic electrochemical reduction of oxygen into H_2O on FeN_4-carbon: a density functional theory study. *J. Power Sources*. 2014. **255**: 65.
112. Zhang J., Wang Z., Zhu Z., Wang Q. A density functional theory study on mechanism of electrochemical oxygen reduction on FeN_4-graphene. *J. Electrochem. Soc*. 2015. **162**: F796.
113. Perdew J. P., Burke K., Ernzerhof M. Generalized Gradient Approximation Made Simple. *Phys. Rev. Lett*. 1996. **77**: 3865.
114. Li Y., Zhou Z., Yu G., Chen W., Chen Z. CO Catalytic Oxidation on Iron-Embedded Graphene: Computational Quest for Low-Cost Nanocatalysts. *J. Phys. Chem. C*. 2010. **114**: 6250.
115. Nørskov J. K., Rossmeisl J., Logadottir A., Lindqvist L., Kitchin J. R., Bligaard T., Jonsson H. Origin of the Overpotential for Oxygen Reduction at a Fuel-Cell Cathode. *J. Phys. Chem. B*. 2004. **108**: 17886.
116. Maruyama J., Baier C., Wolfschmidt H., Bele P., Stimming U. Enhancement of oxygen reduction at Fe tetrapyridyl porphyrin by pyridyl-N coordination to transition metal ions. *Electrochim. Acta*. 2012. **63**: 16.

117. Medard C., Lefevre M., Dodelet J., Jaouen F., Lindbergh G. Oxygen reduction by Fe-based catalysts in PEM fuel cell conditions: Activity and selectivity of the catalysts obtained with two Fe precursors and various carbon supports. *Electrochim. Acta*. 2006. **51**: 3202.
118. Weiss J. J. Nature of the iron-oxygen bond in oxyhaemoglobin. Nature. 1964. **202**: 83.
119. Griffith J. S. On the magnetic properties of some haemoglobin complexes. *The Royal Society*. 1956. **235**: 23.
120. Wang G., Ramesh N., Hsu A., Chu D., Chen R. Density functional theory study of the adsorption of oxygen molecule on iron phthalocyanine and cobalt phthalocyanine. *Mol. Simul*. 2008. **34**: 1051.
121. Zhang P., Chen X. F., Lian J. S., Jiang Q. Structural Selectivity of CO Oxidation on Fe/N/C Catalysts. *J. Phys. Chem. C*. 2012. **116**(33): 17572.
122. Zhang L., Xia Z. Mechanisms of Oxygen Reduction Reaction on Nitrogen-Doped Graphene for Fuel Cells. *J. Phys. Chem. C*. 2011. **115**: 11170.
123. Hyman M. P., Medlin J. W. Mechanistic Study of the Electrochemical Oxygen Reduction Reaction on Pt(111) Using Density Functional Theory. *J. Phys. Chem. B*. 2006. **110**(31): 15338.
124. Nilekar A. U., Mavrikakis M. Improved oxygen reduction reactivity of platinum monolayers on transition metal surfaces. *Surf. Sci*. 2008. **602**: L89.
125. Zhang J., Vukmirovic M. B., Xu Y., Mavrikakis M., Adzic R. R. Controlling the Catalytic Activity of Platinum-Monolayer Electrocatalysts for Oxygen Reduction with Different Substrates. *Angew. Chem. Int. Ed*. 2005. **44**(14): 2132.
126. Chen Z., Higgins D., Yu A., Zhang L., Zhang. A Review On Non-Precious Metal Electrocatalysts For PEM Fuel Cells. *J. Energy Environ. Sci*. 2011. **4**: 3167.
127. Wu G., Chen Z., Artyushkov K., Garzon F. H., Zelenay P. Polyaniline-derived Non-Precious Catalyst for the Polymer Electrolyte Fuel Cell Cathode. *ECS Trans*. 2008. **16**: 159.
128. Longo R. C., Carrete J., Ferrer J., Gallego L. J. Structural, Magnetic, And Electronic Properites Of Nin And Fen Nanostructures (N = 1−4) Adsorbed On Zigzag Graphene Nanoribbons. *Phys. Rev. B*. 2010. **81**: 115418.
129. Ritter K. A., Lyding J. W. The Influence Of Edge Structure On The Electronic Properties Of Graphene Quantum Dots And Nanoribbons. *Nat. Mater*. 2009. **8**: 235−242.
130. Studt F. The Oxygen Reduction Reaction on Nitrogen-Doped Graphene. *Catal. Lett*. 2013. **143**: 58−60.
131. Holby E. F., Wu G., Zelenay P., Taylor C. D. Metropolis Monte Carlo Search for Non-Precious Metal Catalyst Active Site Candidates. *ECS Trans*. 2012. **50**: 1839.
132. Tributsch H., Koslowski U. I., Dorbrandt I. Experimental And Theoretical Modeling Of Fe-, Co-, Cu-, Mn-Based Electrocatalysts For Oxygen Reduction. *Electrochim. Acta*. 2008. **53**: 2198.
133. Yeager E. Dioxygen Electrocatalysis: Mechanisms In Relation To Catalyst Structure. *J. Mol. Catal*. 1986. **38**: 5.
134. Perdew J. P., Burke K., Ernzerhof M. Generalized Gradient Approximation Made Simple. *Phys. Rev. Lett*. 1996. **77**: 3865.
135. Jonsson H., Mills G., Jacobsen K. W. *Classical and quantum dynamics in condensed phase simulations* (World Scientific: Singapore, 1998).
136. Meunier B., de Visser S. P., Shaik S. Mechanism of oxidation reactions catalyzed by cytochrome P450 enzymes. *Chem. Rev*. 2004. **104**: 3947.
137. Kille S., Zilly F. E., Acevedo J. P., Reetz M. T. Regio- and stereoselectivity of P450-catalysed hydroxylation of steroids controlled by laboratory evolution. *Nat. Chem*. 2011. **3**: 738.
138. Burgess B. K., Lowe D. J. Mechanism of molybdenum nitrogenase. *Chem. Rev*. 1996. **96**: 2983.

139. Ambundo E. A., Friesner R. A., Lippard S. J. Reactions of methane monooxygenase intermediate Q with derivatized methanes. *J. Am. Chem. Soc*. 2002. **124**: 8770.
140. Ensing B., Buda F., Gribnau M. C. M., Baerends E. J. Methane-to-methanol oxidation by the hydrated iron(IV) oxo species in aqueous solution: A combined DFT and Car–Parrinello molecular dynamics study. *J. Am. Chem. Soc*. 2004. **126**: 4355.
141. Das T. K., Couture M., Ouellet Y., Guertin M., Rousseau D. L. Simultaneous observation of the O–O and Fe–O_2 stretching modes in oxyhemoglobins. *Proc. Natl. Acad. Sci. U.S.A*. 2001. **98**: 479.
142. Kudrik E. V., Afanasiev P., Alvarez L. X., Dubourdeaux P., Clemancey M., Latour J.-M., Blondin G., Bouchu D., Albrieux F., Nefedov S. E., Sorokin A. B. An N-bridged high-valent diiron–oxo species on a porphyrin platform that can oxidize methane. *Nat. Chem*. 2012. **4**: 1024.
143. Kwak J. H., Hu J., Mei D., Yi C.-W., Kim D. H., Peden C. H. F., Allard L. F., Szanyi J. Coordinatively unsaturated Al^{3+} centers as binding sites for active catalyst phases of platinum on g-Al_2O_3. *Science*. 2009. **325**: 1670.
144. Panov G. I., Uriarte A. K., Rodkin M. A., Sobolev V. I. Generation of active oxygen species on solid surfaces. Opportunity for novel oxidation technologies over zeolites. *Catal. Today*. 1998. **41**: 365.
145. Zecchina A., Rivallan M., Berlier G., Lamberti C., Ricchiardi G. Structure and nuclearity of active sites in Fe-zeolites: Comparison with iron sites in enzymes and homogeneous catalysts. *Phys. Chem. Chem. Phys*. 2007. **9**: 3483.
146. Thomas J. M. The concept, reality and utility of single-site heterogeneous catalysts (SSHCs). *Phys. Chem. Chem. Phys*. 2014. **16**: 7647.
147. Cretu O., Krasheninnikov A. V., Rodríguez-Manzo J. A., Sun L., Nieminen R. M., Banhart F. Migration and localization of metal atoms on strained graphene. *Phys. Rev. Lett*. 2010. **105**: 196102.
148. Wang H., Wang Q., Cheng Y., Li K., Yao Y., Zhang Q., Dong C., Wang P., Schwingenschlögl U., Yang W., Zhang X. X. Doping monolayer graphene with single atom substitutions. *Nano Lett*. 2012. **12**: 141.
149. Zhao J., Deng Q., Bachmatiuk A., Sandeep G., Popov A., Eckert J., Rümmeli M. H. Freestanding single-atom-thick iron membranes suspended in graphene pores. *Science*. 2014. **343**: 1228.
150. Claessens C. G., Hahn U., Torres T. Phthalocyanines: From outstanding electronic properties to emerging applications. *Chem. Rec*. 2008. **8**: 75.
151. Deng D., Yu L., Pan X., Wang S., Chen X., Hu P., Sun L., Bao X. Size effect of graphene on electrocatalytic activation of oxygen. *Chem. Commun*. 2011. **47**: 10016.
152. Sandoval S., Kumar N., Sundaresan A., Rao C. N. R., Fuertes A., Tobias G. Enhanced thermal oxidation stability of reduced graphene oxide by nitrogen doping. *Chem. Eur. J*. 2014. **20**: 11999.
153. Dehui Deng, Xiaoqi Chen, Liang Yu, Xing Wu, Qingfei Liu, Yun Liu, Huaixin Yang, Huanfang Tian, Yongfeng Hu, Peipei Du, Rui Si, Junhu Wang, Xiaoju Cui, Haobo Li, Jianping Xiao, Tao Xu, Jiao Deng, Fan Yang, Paul N. Duchesne, Peng Zhang, Jigang Zhou, Litao Sun, Jianqi Li, Xiulian Pan, Xinhe Bao. A single iron site confined in a graphene matrix for the catalytic oxidation of benzene at room temperature. *Sci. Adv*. 2015. **1**: e1500462
154. Hentsche M., Hermann H., Gemming T., Wendrock H., Wetzig K. Nanostructured graphite prepared by ball-milling at low temperatures. *Carbon*. 2006. **44**: 812.
155. Jeon I.-Y., Shin Y.-R., Sohn G.-J., Choi H.-J., Bae S.-Y., Mahmood J., Jung S.-M., Seo J.-M., Kim M.-J., Chang D. W., Dai L., Baek J.-B. Edge-carboxylated graphene nanosheets via ball milling. *Proc. Natl. Acad. Sci. U.S.A*. 2012. **109**: 5588.

156. Immohr S., Felderhoff M., Weidenthaler C., Schüth F. An orders-of-magnitude increase in the rate of the solid-catalyzed CO oxidation by in situ ball milling. *Angew. Chem. Int. Ed*. 2013. **52**: 12688.
157. Guo X., Fang G., Li G., Ma H., Fan H., Yu L., Ma C., Wu X., Deng D., Wei M., Tan D., Si R., Zhang S., Li J., Sun L., Tang Z., Pan X., Bao X. Direct, nonoxidative conversion of methane to ethylene,aromatics, and hydrogen. *Science*. 2014. **344**: 616.
158. Niwa S.-i., Eswaramoorthy M., Nair J., Raj A., Itoh N., Shoji H., Namba T., Mizukami F. A one-step conversion of benzene to phenol with a palladium membrane. *Science*. 2002. **295**: 105.
159. Tanev P. T., Chibwe M., Pinnavaia T. J. Titanium-containing mesoporous molecular sieves for catalytic oxidation of aromatic compounds. *Nature*. 1994. **368**: 321.
160. Ding G., Wang W., Jiang T., Han B., Fan H., Yang G. Highly selective synthesis of phenol from benzene over a vanadium-doped graphitic carbon nitride catalyst. *Chem. Cat. Chem*. 2013. 5: 192.
161. Yang J.-H., Sun G., Gao Y., Zhao H., Tang P., Tan J., Lu A.-H., Ma D. Direct catalytic oxidation of benzene to phenol over metal-free graphene-based catalyst. *Energy Environ. Sci*. 2013. **6**: 793.
162. Zhang H., Pan X., Han X., Liu X., Wang X., Shen W., Bao X. Enhancing chemical reactions in a confined hydrophobic environment: An NMR study of benzene hydroxylation in carbon nanotubes. *Chem. Sci*. 2013. **4**: 1075.
163. Zhou X., Kang L. A DFT study of graphene-FeN_x (x = 4, 3, 2, 1) catalysts for acetylene hydrochlorination. *Colloids Surf. A: Physicochem. Eng. Asp*. 2021. **618**: 126495.
164. Frisch M. J. T., Schlegel G. W, H. B., Scuseria G. E., Robb M. A., Cheeseman J. R., Scalmani G., Barone V., Mennucci B., Petersson G. A., Nakatsuji H., Caricato M., Li X., Hratchian H. P., Izmaylov A. F., Bloino J., Zheng G., Sonnenberg J. L., Hada M., Ehara M., Toyota K., Fukuda R., Hasegawa J., Ishida M., Nakajima T., Honda Y., Kitao O., *et al.* Gaussian 09, Revision A.02, Gaussian, Inc., Wallingford CT, 2009.
165. Lee C., Yang W., Parr R. G. Development of the Colle-Salvetti correlation-energy formula into a functional of the electron density. *Phys. Rev. B*. 1988. **37**: 785.
166. Grimme S., Antony J., Ehrlich S., Krieg H. A consistent and accurate ab initio parametrization of density functional dispersion correction (DFT-D) for the 94 elements H-Pu. *J. Chem. Phys*. 2010. **132**: 154104.
167. Gonzalez C., Schlegel H. B. An improved algorithm for reaction path following. *J. Chem. Phys*. 1989. **90**: 2154.
168. Gonzalez C., Schlegel H. B. Reaction path following in mass-weighted internal coordinates. *J. Phys. Chem*. 1990. **94**: 5523.
169. Liu F., Zhu G., Yang D., Jia D., Jin F., Wang W. Systematic exploration of N, C configurational effects on the ORR performance of Fe–N doped graphene catalysts based on DFT calculations. *RSC Adv*. 2019. **9**: 22656.
170. Yang Y., Li K., Meng Y., Wang Y., Wu Z. A density functional study on the oxygen reduction reaction mechanism on FeN_2-doped graphene. *New J. Chem*. 2018. **42**: 6873.
171. Lu T. Multiwfn: a multifunctional wavefunction analyzer. *J. Comput. Chem*. 2012. **33**: 580.
172. Ketrat S., Maihom T., Treesukul P., Boekfa B., Limtrakul J. Theoretical Study of Methane Adsorption and C-H Bond Activation over Fe-Embedded Graphene: Effect of External Electric Field. *J. Comput. Chem*. 2019.
173. Alvarez-Galvan M. C., Mota N., Ojeda M., Rojas S., Navarro R. M., Fierro J. L. G. Direct methane conversion routes to chemicals and fuels. *Catal. Today*. 2011. **171**: 15.
174. Holmen A. Direct conversion of methane to fuels and chemicals. *Catal. Today*. 2009. **142**: 2.

175. Arena F., Gatti G., Martra G., Coluccia S., Stievano L., Spadaro L., Famulari P., Parmaliana A. Structure and reactivity in the selective oxidation of methane to formaldehyde of low-loaded FeO_x/SiO_2 catalysts. *J. Catal*. 2005. **231**: 365.
176. Schwarz H. Chemistry with Methane: Concepts Rather than Recipe. *Angew. Chem. Int. Ed*. 2011. **50**: 10096.
177. Blanksby S. J., Ellison G. B. Bond dissociation energies of organic molecules. *Acc. Chem. Res*. 2003. **36**: 255.
178. Irikura K. K., Beauchamp J. L. Electronic structure considerations for methane activation by third-row transition-metal ions. *J. Phys. Chem*. 1991. **95**(21): 8344.
179. Li F.-X., Armentrout P. B. Activation of methane by gold cations: Guided ion beam and theoretical studies. *J. Chem. Phys*. 2006. **125**(13): 133114.
180. Killelea D. R., Campbell V. L., Shuman N. S., Smith R. R., Utz A. L. Surface Temperature Dependence of Methane Activation on Ni(111). *J. Phys. Chem. C*. 2009. **113**: 20618.
181. Trevor D. J., Cox D. M., Kaldor A. Methane activation on unsupported platinum clusters. *J. Am. Chem. Soc*. 1990. **112**(10): 3742.
182. Prats H., Gutierrez R. A., Pinero J. J., Vines F., Bromley S. T., Ramirez P. J., Rodriguez J. A., Illas F. Room Temperature Methane Capture and Activation by Ni Clusters Supported on TiC(001): Effects of Metal–Carbide Interactions on the Cleavage of the C–H Bond. *J. Am. Chem. Soc*. 2019. **141**(13): 5303.
183. Koszinowski K., Schröder D., Schwarz H. Reactivity of Small Cationic Platinum Clusters. *J. Phys. Chem. A*. 2003. **107**: 4999.
184. Roithová J., Schröder D Selective Activation of Alkanes by Gas-Phase Metal Ions. *Chem. Rev*. 2010. **110**: 1170.
185. Lang S. M., Bernhardt T. M., Barnett R. N., Landman U. Methane Activation and Catalytic Ethylene Formation on Free Au_2. *Angew. Chem. Int. Ed*. 2010. **49**: 980.
186. Schröder D., Roithová J. Low-Temperature Activation of Methane: It also Works Without a Transition Metal. *Angew. Chem. Int. Ed*. 2006. **45**: 5705.
187. Feyel S., Döbler J., Schröder D. J. Sauer, Schwarz H. Gas-Phase Oxidation of Propane and 1-Butene with $[V_3O_7]^+$: Experiment and Theory in Concert. *Angew. Chem. Int. Ed*. 2006. **45**: 4681.
188. Kurnaz E., Fellah M. F., Onal I. A density functional theory study of C–H bond activation of methane on a bridge site of M–O–M-ZSM-5 Clusters (M = Au, Ag, Fe and Cu). *Microporous Mesoporous Mater*. 2011. **138**: 68.
189. Ding B., Huang S., Wang W. Methane activation over Ag-exchanged ZSM-5 zeolites: A theoretical study. *Appl. Surf. Sci*. 2008. **254**: 4944.
190. Kim Y.-H., Borry R. W., Iglesia E. Genesis of methane activation sites in Mo-exchanged H–ZSM-5 catalysts. *Microporous Mesoporous Mater*. 2000. **35-36**: 495.
191. Yoshizawa K., Shiota Y., Yumura T., Yamabe T. Direct Methane−Methanol and Benzene−Phenol Conversions on Fe−ZSM-5 Zeolite: Theoretical Predictions on the Reaction Pathways and Energetics. *J. Phys. Chem. B*. 2000. **104**(4): 734.
192. Anton R., Schneidereit I. *In situ* TEM investigations of dendritic growth of Au particles on HOPG. *Phys. Rev. B*. 1998. **58**: 13874.
193. Lange U., Hirsch T., Mirsky V. M., Wolfbeis O. S. Hydrogen sensor based on a graphene–palladium nanocomposite. *Electrochim. Acta*. 2011. **56**: 3707.
194. Tjoa V., Jun W., Dravid V., Mhaisalkar S., Mathews N. Hybrid graphene–metal nanoparticle systems: electronic properties and gas interaction. *J. Mater. Chem*. 2011. **21**: 15593.
195. Zhou K., Zhu Y., Yang X., Luo J., Li C., Luan S. A novel hydrogen peroxide biosensor based on Au–graphene–HRP–chitosan biocomposites. *Electrochim. Acta*. 2010. **55**: 3055.

196. Baby T. T., Aravind S. S. J., Arockiadoss T., Rakhi R. B., Ramaprabhu S. Metal decorated graphene nanosheets as immobilization matrix for amperometric glucose biosensor. *Actuators Sens. B Chem*. 2010. **145**: 71.
197. Zhou M., Zhang A., Dai Z., Feng Y. P., Zhang C. Strain-Enhanced Stabilization and Catalytic Activity of Metal Nanoclusters on Graphene. *J. Phys. Chem. C*. 2010. **114**: 16541.
198. Song E. H., Wen Z., Jiang Q. CO Catalytic Oxidation on Copper-Embedded Graphene. *J. Phys. Chem. C*. 2011. **115**: 3678.
199. Yang J., Tian C., Wang L., Fu H. An effective strategy for small-sized and highly-dispersed palladium nanoparticles supported on graphene with excellent performance for formic acid oxidation. *J. Mater. Chem*. 2011. **21**: 3384.
200. Zhou M., Zhang A., Dai Z., Zhang C., Feng Y. P. Greatly enhanced adsorption and catalytic activity of Au and Pt clusters on defective graphene. *J. Chem. Phys*. 2010. **132**: 194704.
201. Yoo E., Okata T., Akita T., Kohyama M., Nakamura J., Honma I. Enhanced Electrocatalytic Activity of Pt Subnanoclusters on Graphene Nanosheet Surface. *Nano. Lett*. 2009. **9**: 2255.
202. Lu Y.-H., Zhou M., Zhang C., Feng Y.-P. Metal-Embedded Graphene: A Possible Catalyst with High Activity. *J. Phys. Chem. C*. 2009. **113**: 20156.
203. Chisholm M. F., Duscher G., Windl W. Oxidation Resistance of Reactive Atoms in Graphene. *Nano. Lett*. 2012. **12**: 4651.
204. Cortés-Arriagada D., Villegas-Escobar N., Miranda-Rojas S., Toro-Labbé A. Adsorption/desorption process of formaldehyde onto iron doped graphene: a theoretical exploration from density functional theory calculations. *PCCP*. 2017. **19**: 4179.
205. Zhang H.-p., Luo X.-g., Song H.-t., Lin X.-y., Lu X., Tang Y. DFT study of adsorption and dissociation behavior of H_2S on Fe-doped graphene. *Appl. Surf. Sci*. 2014. **317**: 511.
206. Wanno B., Tabtimsai C. *Superlattices Microstruct*. 2014. **67**: 110.
207. Cortés-Arriagada D., Villegas-Escobar N., Ortega D. E. Fe-doped graphene nanosheet as an adsorption platform of harmful gas molecules (CO, CO_2, SO_2 and H_2S), and the co-adsorption in O_2 environments. *Appl. Surf. Sci*. 2018. **427**: 227.
208. Wannakao S., Nongnual T., Khongpracha P., Maihom T., Limtrakul J. Reaction Mechanisms for CO Catalytic Oxidation by N_2O on Fe-Embedded Graphene. *J. Phys. Chem. C*. 2012. **116**: 16992.
209. He Z., He K., Robertson A. W., Kirkland A. I., Kim D., Ihm J., Yoon E., Lee G.-D., Warner J. H. Atomic Structure and Dynamics of Metal Dopant Pairs in Graphene. *Nano. Lett*. 2014. **14**: 3766.
210. He C., Zhang W., Deng J. Electric Field and Size Effects on Atomic Structures and Conduction Properties of Ultrathin Cu Nanowires. *J. Phys. Chem. C*. 2011. **115**: 3327.
211. Zhang R. Q., Hou C., Gao N., Wen Z., Jiang Q. Multi-Field Effect on the Electronic Properties of Silicon Nanowires. *Chem. Phys. Chem*. 2011. **12**: 1302.
212. Hirao H., Chen H., Carvajal M. A., Wang Y., Shaik S. Effect of External Electric Fields on the C−H Bond Activation Reactivity of Nonheme Iron−Oxo Reagents. *J. Am. Chem. Soc*. 2008. **130**: 3319.
213. Shaik S., de Visser S. P., Kumar D. External Electric Field Will Control the Selectivity of Enzymatic-Like Bond Activations. *J. Am. Chem. Soc*. 2004. **126**: 11746.
214. Aragonès A. C., Haworth N. L., Darwish N., Ciampi S., Bloomfield N. J., Wallace G. G., Diez-Perez I., Coote M. L. Electrostatic catalysis of a Diels-Alder reaction. *Nature*. 2016. **531**: 88.
215. Li Y., Rotkin S. V., Ravaioli U. Electronic Response and Bandstructure Modulation of Carbon Nanotubes in a Transverse Electrical Field. *Nano Lett*. 2003. **3**: 183.

216. Liu W., Zhao Y. H., Nguyen J., Li Y., Jiang Q., Lavernia E. J. Electric field induced reversible switch in hydrogen storage based on single-layer and bilayer graphenes. *Carbon*. 2009. **47**: 3452.
217. Ao Z. M., Peeters F. M. Electric Field Activated Hydrogen Dissociative Adsorption to Nitrogen-Doped Graphene. *J. Phys. Chem. C*. 2010. **114**: 14503.
218. Lv Y.-a., Zhuang G.-l., Wang J.-g., Jia Y.-b., Xie Q. Enhanced role of Al or Ga-doped graphene on the adsorption and dissociation of N_2O under electric field. *PCCP*. 2011. **13**: 12472.
219. Zhou X. H., Huang Y., Chen X. S., Lu W. External Electric Field Modulation of Structural Configurations and Electronic Properties of Gold Dimers on Graphene. *J. Phys. Chem. C*. 2012. **116**: 7393.
220. Peles-Lemli B., Kánnár D., Nie J. C., Li H., Kunsági-Máté S. Some Unexpected Behavior of the Adsorption of Alkali Metal Ions onto the Graphene Surface under the Effect of External Electric Field. *J. Phys. Chem. C*. 2013, **117**: 21509.
221. Liu W., Zhao Y. H., Li Y., Lavernia E. J., Jiang Q. A reversible switch for hydrogen adsorption and desorption: electric fields. *PCCP*. 2009. **11**: 9233.
222. Song E. H., Yan J. M., Lian J. S., Jiang Q. External Electric Field Catalyzed N_2O Decomposition on Mn-Embedded Graphene. *J. Phys. Chem. C*. 2012. **116**: 20342.
223. Zhao Y., Truhlar D. G. Benchmark Data for Interactions in Zeolite Model Complexes and Their Use for Assessment and Validation of Electronic Structure Methods. *J. Phys. Chem. C*. 2008. **112**: 6860.
224. Zhao Y., Truhlar D. G. Density Functionals with Broad Applicability in Chemistry. *Acc. Chem. Res*. 2008. **41**: 157.
225. Dolg M., Wedig U., Stoll H., Preuss H. Energy-adjusted ab initio pseudopotentials for the first row transition elements. *J. Chem. Phys*. 1987. **86**: 866.
226. Reed A. E., Curtiss L. A., Weinhold F. Intermolecular interactions from a natural bond orbital, donor-acceptor viewpoint. *Chem. Rev*. 1988. **88**: 899.
227. Sowlati-Hashjin S., Matta C. F. The chemical bond in external electric fields: Energies, geometries, and vibrational Stark shifts of diatomic molecules. *J. Chem. Phys*. 2013. **139**: 142102.
228. Cortés-Arriagada D., Villegas-Escobar N. A DFT analysis of the adsorption of nitrogen oxides on Fe-doped graphene, and the electric field induced desorption. *Appl. Surf. Sci*. 2017. **420**: 446.
229. Impeng S., Khongpracha P., Sirijaraensre J., Jansang B., Ehara M., Limtrakul J. Methane activation on Fe- and FeO-embedded graphene and boron nitride sheet: role of atomic defects in catalytic activities. *RSC Adv*. 2015. **5**: 97918.
230. Impeng S., Khongpracha P., Warakulwit C., Jansang B., Sirijaraensre J., Ehara M., Limtrakul J. Direct oxidation of methane to methanol on Fe–O modified graphene. *RSC Adv*. 2014. **4**: 12572.
231. Warner J. H., et al. Structural transformations in graphene studied with high spatial and temporal resolution. *Nat. Nanotechnol*. 2009. **4**(8): 500.
232. Warner J. H., et al. Dislocation-driven deformations in graphene. *Science*. 2012. **337**(6091): 209.
233. Huang P.Y., et al. Grains and grain boundaries in single-layer graphene atomic patchwork quilts. Nature. 2011. **469**(7330): 389.
234. Girit Ç.Ö., et al. Graphene at the edge: Stability and dynamics. *Science*. 2009. **323**(5922): 1705.
235. Krasheninnikov A. V., Lehtinen P. O., Foster A. S., Pyykkö P., Nieminen R. M. Embedding transition-metal atoms in graphene: Structure, bonding, and magnetism. *Phys. Rev. Lett*. 2009. **102**(12): 126807.

236. Meyer J. C., et al. Experimental analysis of charge redistribution due to chemical bonding by high-resolution transmission electron microscopy. *Nat. Mater*. 2011. **10**(3): 209.
237. Robertson A. W., et al. (2013) Dynamics of single Fe atoms in graphene vacancies. *Nano Lett.* **13**(4): 1468.
238. Wang H., et al. Unraveling the atomic structure of ultrafine iron clusters. *Sci. Rep*. 2012. **2**: 995.
239. Zhou W., et al. Atomically localized plasmon enhancement in monolayer graphene. *Nat Nanotechnol*. 2012. **7**(3): 161.
240. Wang H., et al. Interaction between single gold atom and the graphene edge: A study via aberration-corrected transmission electron microscopy. *Nanoscale*. 2012. **4**(9): 2920.
241. Hardcastle T.P., et al. Mobile metal adatoms on single layer, bilayer, and trilayer graphene: An ab initio DFT study with van der Waals corrections correlated with electron microscopy data. *Phys. Rev. B Condens. Matter. Mater. Phys*. 2013. **87**: 195430.
242. Gao J., Zhao J., Ding F. Transition metal surface passivation induced grapheme edge reconstruction. *J. Am. Chem. Soc*. 2012. **134**(14): 6204.
243. Shu H., Chen X., Tao X., Ding F. Edge structural stability and kinetics of grapheme chemical vapor deposition growth. *ACS Nano*. 2012. **6**(4): 3243.
244. Zhao J., Deng Q., Avdoshenko S. M., Fu L., Eckert J., Rümmeli M. H. Direct in situ observations of single Fe atom catalytic processes and anomalous diffusion at graphene edges. *PNAS*. 2014. **44**: 15641.
245. Qiao B., et al. Single-atom catalysis of CO oxidation using $Pt1/FeO_x$. *Nat. Chem*. 2011. **3**(8): 634.
246. Sun S., et al. Single-atom catalysis using Pt/Graphene achieved through atomic layer deposition. *Sci. Rep*. 2013. **3**: 1775.
247. Börrnert F., et al. Retro-fitting an older (S)TEM with two Cs aberration correctors for 80 kV and 60 kV operation. *J. Microsc*. 2013. **249**(2): 87.
248. Lee Y.H., Kim S.G., Tománek D. Catalytic growth of single-wall carbon nanotubes: An ab initio study. *Phys. Rev. Lett*. 1997. **78**: 2393.
249. Gan Y., Sun L., Banhart F. One- and two-dimensional diffusion of metal atoms in graphene. *Small.* 2008. **4**(5): 587.
250. Bouchaud J. P., Georges A. Anomalous diffusion in disordered media: Statistical mechanisms, models and physical applications. *Phys Rep*. 1990. **195**(4-5): 127.
251. Metzler R., Klafter J. The random walk's guide to anomalous diffusion: A fractional dynamics approach. *J. Phys. Rep*. 2000. **339**: 1.
252. Warner J. H., Liu Z., He K., Robertson A. W., Suenaga K. Sensitivity of graphene edge states to surface adatom interactions. *Nano. Lett*. 2013. **13**(10): 4820.
253. He K., Lee G. D., Robertson A. W., Yoon E., Warner J. H. Hydrogen-free grapheme edges. *Nat. Commun*. 2014. **5**: 3040.
254. Malola S., Häkkinen H., Koskinen P. Gold in graphene: In-plane adsorption and diffusion. *Appl. Phys. Lett*. 2009. **94**: 043106.
255. Krasheninnikov A. V., Nordlund K. Ion and electron irradiation-induced effects in nanostructured materials. *J. Appl. Phys*. 2010. **107**: 071301.
256. Aryanpour M., van Duin A. C. T., Kubicki J. D. Development of a reactive force field for iron-oxyhydroxide systems. *J. Phys. Chem. A.* 2010. **114**(21): 6298.

УДК 544.18:546.72 *DOI: 10.15407/Surface.2025.17.003*

ЗАЛІЗОВМІСНІ ПОХІДНІ ГРАФЕНУ

О. С. Кремень В. В. Лобанов, М. Т. Картель

Інститут хімії поверхні ім. О. О. Чуйка НАН України,
вул. Олега Мудрака, 17, Київ, 03164, Україна, е-пошта: kremenoksana@ukr.net

Огляд присвячений розгляду результатів квантовохімічних розрахунків властивостей електрокаталізаторів на основі залізовмісних вуглеців, переважно графену. Описаний спосіб віднесення піків N1s в рентгенофотоелектронних спектрах (РФЕС) залежно від типу стану атомів азоту в електрокаталізаторах, які отримано піролізом суміші вуглець-, азот- та залізовмісних прекурсорів. Спільне використання даних з експериментально отриманих спектрів РФЕС та результатів квантовохічних розрахунків щодо енергії хімічно викликаних зсувів остівних рівнів N1s дозволило напівкількісно визначити вміст різних типів атомів азоту в електрокаталізаторах реакцій відновлення кисню (РВК).

Кількісний аналіз областей спектрів поглинання рентгенівських променів (як спектрів поглинання розширеної тонкої області, так і спектрів поблизу краю) каталізаторів FeN-C, які не містять або майже не містять кристалічних структур Fe, показав існування у них порфіриноподібних фрагментів FeN_4C_{12}. Електрохімічні дослідження показали, що фрагменти FeN_4C_{12} каталізують чотириелектронне відновлення молекули кисню до молекули води. Порфіриноподібні фрагменти можуть формуватися або у невпорядкованих графенових шарах, або між зигзагоподібними їх краями, що утворюють мікропори. Каталізатори FeN-C, які попередньо піддавалися Ar- та NH_3-піролізу, демонструють зовсім різну активність у РВК. Збільшення активності у РВК, яка викликана фрагментами типу FeN_4C_{12} обумовлена високоосновними N-групами, що утворюються при піролізі з NH_3.

Детальний кінетичний та термодинамічний аналіз протікання РВК на каталізаторі типу FeN_4-G з усіма пірольними атомами азоту показали, що енергія активації реакції дисоціації адсорбованої молекули O_2 дуже висока незалежно від типу її адсорбції на каталізаторі FeN_4-G у конфігурації моделей Полінга або Гріффіта.

Отримані в розрахунках діаграми зміни вільної енергії у РВК показують, що для всіх її елементарних стадій за чотириелектронним механізмом зміни вільної енергії (ΔG) негативні при низькому потенціалі електрода (до 0.41 еВ). Стадія, що лімітує швидкість РВК, це відновлення $OH_{(ads)}$ до $H_2O_{(ads)}$, з E_{act} = 1.02 еВ.

Вперше проведено самоузгоджене порівняння активності ряду потенційних структур крайових дефектів активного центру залізовмісних каталізаторів на основі графенового нановуглецю та показано, що в залежності від умов синтезу, найбільш стабільними є структури з залізовмісними дефектами та чотирма або трьома атомами азоту. Передбачається, що ці структури можуть співіснувати. Кластерні структури типу $FeN_3(Fe_2N_5)$, ймовірно, здатні розщеплювати зв'язок у молекулі O_2 з нульовим активаційним бар'єром і, отже, можуть направити РВК по дисоціативного маршруту. Очікується, що цей маршрут буде більш селективним, без утворення H_2O_2 через надмірне зв'язування проміжних продуктів у РВК. Дані неепіричної молекулярної динаміки показують, що на цю мимовільну реакцію, швидше за все, не впливає сольватація, оскільки розчинник, ймовірно, не змінює стійкості розглянутих крайових дефектів.

Отримані методом теорії функціоналу густини результати показали, що в міру збільшення ступеня допування атомами азоту в графенах-FeN_x (x = 4, 3, 2, 1) активність реакції їх гідрохлорування послідовно зростає. Отримано наступний порядок енергії

активації (E_{act}) для каталітичної реакції серії каталізаторів графен-FeN_x: графен-FeN_1 > графен-FeN_2 > графен-FeN_3 > графен-FeN_4.

Без накладання зовнішнього електричного поля впроваджений у графенову ґратку атом заліза активує молекулу метану з E_{act} 25.7 ккал/моль. Стабільність адсорбційних комплексів, перехідних станів та продуктів реакції істотно змінюється під дією напряму та напруженості прикладеного електричного поля. Позитивне електричне поле дестабілізує адсорбційні комплекси, тоді як перехідний стан і продукти реакції виявилися стабільнішими порівняно з випадком коли поле відсутнє. Енергія активації значно зменшилася з 25.7 до 17.5 ккал/моль при накладенні електричного поля напруженістю +0.015 ат.од. Отримані результати свідчать, що каталітична активність графену з додаванням заліза може регулюватися прикладеним зовнішнім електричним полем.

Методом трансмісійної електронної спектроскопії з корекцією аберацій показано, що дифузія одиночних атомів заліза на графенових краях залежить від типу краю (зигзаґ чи крісло): субдифузія проявляється при формуванні краю типу крісло, а супердифузія – краю типу зигзаґ. Теоретичні розрахунки показують, що ця відмінність пов'язана з різними бар'єрами дифузії між стійкими станами. Очікується, що аномальна дифузійна поведінка вплине на кінетику росту/каталізу синтетичних sp^2 наноматеріалів, вирощених з використанням металевих каталізаторів. Проведені спостереження in situ та теоретичні дослідження (метод молекулярної динаміки, метод ТФГ) дають ключове уявлення про фундаментальні процеси росту sp^2 нанорозмірних структур, зокрема графену та вуглецевих нанотрубок, на металевих каталізаторах.

Ключові слова: *теорія функціоналу густини**,** залізовмісні електрокаталізатори**,** рентгенофотоелектронні спектри, остівні рівні N1s, порфіриноподібні фрагменти, реакція відновлення кисню (РВК), чотириелектронний механізм РВК, ступінь допування графену азотом, аномальна дифузія.*